OPEN ACCESS



The Effects of Stellar Population and Gas Covering Fraction on the Emergent Ly α Emission of High-redshift Galaxies*

Naveen A. Reddy¹ , Michael W. Topping², Alice E. Shapley³ , Charles C. Steidel⁴ , Ryan L. Sanders⁵.8 , Xinnan Du¹ , Alison L. Coil⁵ , Bahram Mobasher¹, Sedona H. Price⁵ , and Irene Shivaei².8
¹ Department of Physics and Astronomy, University of California, Riverside, 900 University Avenue, Riverside, CA 92521, USA; naveenr@ucr.edu

2 Steward Observatory, University of Arizona, 933 North Cherry Avenue, Tucson, AZ 85721, USA

3 Department of Physics & Astronomy, University of California, Los Angeles, 430 Portola Plaza, Los Angeles, CA 90095, USA

4 Cahill Center for Astronomy and Astrophysics, California Institute of Technology, MC 249-17, Pasadena, CA 91125, USA

5 Department of Physics, University of California, Davis, One Shields Ave., Davis, CA 95616, USA

6 Center for Astrophysics and Space Sciences, University of California, San Diego, 9500 Gilman Drive, La Jolla, CA 92093-0424, USA

7 Max-Planck-Institut für Extraterrestrische Physik, Postfach 1312, Garching, D-85741, Germany

Received 2021 August 11; revised 2021 November 17; accepted 2021 November 17; published 2022 February 9

Abstract

We perform joint modeling of the composite rest-frame far-UV and optical spectra of redshift $1.85 \leqslant z \leqslant 3.49$ star-forming galaxies to deduce key properties of the massive stars, ionized interstellar medium (ISM), and neutral ISM, with the aim of investigating the principal factors affecting the production and escape of Ly α photons. Our sample consists of 136 galaxies with deep Keck/LRIS and MOSFIRE spectra covering, respectively, Ly β through C III] $\lambda\lambda$ 1907, 1909 and [O II], [Ne III], H β , [O III], H α , [N II], and [S II]. Spectral and photoionization modeling indicates that the galaxies are uniformly consistent with stellar population synthesis models that include the effects of stellar binarity. Over the dynamic range of our sample, there is little variation in stellar and nebular abundance with Ly α equivalent width, W_{λ} (Ly α), and only a marginal anticorrelation between age and W_{λ} (Ly α). The inferred range of ionizing spectral shapes is insufficient to solely account for the variation in W_{λ} (Ly α); rather, the covering fraction of optically thick H I appears to be the principal factor modulating the escape of Ly α , with most of the Ly α photons in down-the-barrel observations of galaxies escaping through low column density or ionized channels in the ISM. Our analysis shows that a high star-formation-rate surface density, $\Sigma_{\rm SFR}$, particularly when coupled with a low galaxy potential (i.e., low stellar mass), can aid in reducing the covering fraction and ease the escape of Ly α photons. We conclude with a discussion of the implications of our results for the escape of ionizing radiation at high redshift.

Unified Astronomy Thesaurus concepts: Stellar abundances (1577); Interstellar abundances (832); H II regions (694); High-redshift galaxies (734); Interstellar medium (847); Star formation (1569)

1. Introduction

Ly α emission is often used as a signpost of ionizing radiation from star-forming galaxies (Partridge & Peebles 1967) owing to the strength of the line and the cosmic abundance of hydrogen. Despite its widespread use, its large absorption cross section means that a Ly α photon may traverse a complicated path through the interstellar medium (ISM) of a galaxy before being absorbed by dust or escaping (Spitzer 1978; Meier & Terlevich 1981). The intensity of the line will be severely affected as a result. Ly α photons will scatter out of the line of sight by relatively small columns of H I, rendering a significant fraction of the flux undetectable in typical slit-spectroscopic observations of galaxies. The observed Ly α flux will be further diminished in the presence of dust, and its velocity profile will be shaped by bulk motions that cause the photons to shift out of resonance (e.g., Kunth et al. 1998).

⁸ NASA Hubble Fellow.

Original content from this work may be used under the terms of the Creative Commons Attribution 4.0 licence. Any further distribution of this work must maintain attribution to the author(s) and the title of the work, journal citation and DOI.

While the resonant scattering of Ly α poses challenges for interpreting the nature of the ionizing sources and the subsequent transmission of those photons, it can be exploited to probe the spatial structure and kinematics of the ISM and circumgalactic medium (CGM; e.g., Steidel et al. 2011; Momose et al. 2014; Bacon et al. 2017; Xue et al. 2017; Wisotzki et al. 2018; Leclercq et al. 2020). Further, because Ly α photons are easily scattered, the residual flux that emerges along the observer's sight line holds important clues on the porosity of the ISM, a key factor in the escape of ionizing ("Lyman continuum," or LyC) photons (Zackrisson et al. 2013; Trainor et al. 2015; Dijkstra et al. 2016; Reddy et al. 2016b; Steidel et al. 2018). It is thus not surprising that many efforts to investigate the sources of cosmic reionization have focused on galaxies with strong Ly α emission, or Ly α emitters (LAEs) see Ouchi et al. (2020) and references therein.

Radiative transfer simulations can be used to trace $Ly\alpha$ photons from the time they are produced to their escape or absorption by dust, a useful exercise for understanding how the strength and the velocity profile of the emerging photons is shaped by a clumpy, dusty, or nonstatic ISM (Dijkstra et al. 2006; Verhamme et al. 2006, 2008; Duval et al. 2014; Gronke et al. 2015, 2016; Dayal et al. 2011; Hutter et al. 2014). Nevertheless, one can gain significant insight into the key factors governing the production and escape of $Ly\alpha$ (and LyC) photons—namely, the ionizing spectrum and the gas covering

^{*} Based on data obtained at the W. M. Keck Observatory, which is operated as a scientific partnership among the California Institute of Technology, the University of California, and NASA and was made possible by the generous financial support of the W. M. Keck Foundation.

fraction—without resorting to computationally expensive radiative transfer simulations. As discussed below, these two factors appear to successfully describe the variation in Ly α equivalent widths and escape fractions measured for the high-redshift galaxies analyzed here. The rest-frame far-UV (FUV) and rest-frame optical spectra of galaxies can be used to constrain the ionizing spectrum and the gas covering fraction.

The FUV ($\lambda \simeq 1000-2000 \,\text{Å}$) galaxy spectrum contains a high density of emission and absorption lines well suited for investigating the production and transmission of Ly α photons. Aside from allowing a direct measurement of the emergent Ly α flux, this region of the spectrum contains numerous stellar photospheric absorption lines (e.g., Leitherer et al. 2001) and stellar wind lines (e.g., N V λ 1240, Si IV λ 1402, C IV λ 1550, He II λ 1640; Leitherer et al. 2001; Crowther et al. 2006; Brinchmann et al. 2008) sensitive to the stellar metallicity, age, and initial mass function (IMF)-factors that are among those responsible for modulating the ionizing radiation field. Several studies have used specific features in the FUV, or full-spectrum fitting, to deduce stellar metallicities and ages of the massive stellar populations in high-redshift galaxies (e.g., Halliday et al. 2008; Sommariva et al. 2012; Steidel et al. 2016; Cullen et al. 2019, 2020; Topping et al. 2020a, 2020b).

The FUV and optical nebular emission lines provide additional powerful constraints on the shape of the extreme-UV (EUV; λ < 912 Å) radiation field, which ultimately sets the intrinsic number of ionizing photons. Specifically, these lines allow one to distinguish between single-star population synthesis models and those that include the effects of stellar multiplicity (binarity). While both flavors of models successfully match many of the stellar photospheric absorption and wind lines in the FUV for various assumptions of the stellar metallicity and age, only the binary models are able to reproduce the hard EUV spectrum required to generate the nebular line luminosities and line ratios measured from composite FUV and optical spectra of $z \sim 2$ galaxies (Steidel et al. 2016).

In addition to providing valuable constraints on the ionizing radiation field, the FUV spectrum includes a number of low- and high-ionization metal and H I absorption lines that may be used to infer gas covering fraction. Several studies have used the strong saturated metal transitions occurring in a predominantly neutral medium (e.g., Si II λ 1260, Si II λ 1527, C II λ 1334, Al II λ 1670) to infer the covering fraction of H_I (e.g., Shapley et al. 2003; Heckman et al. 2011; Berry et al. 2012; Jones et al. 2013; Alexandroff et al. 2015; Trainor et al. 2015; Henry et al. 2015; Du et al. 2018; Harikane et al. 2020). Many of the same works and others have suggested a strong connection between the escape of Ly α (and LyC photons) and gas covering fraction as inferred from these same lines (e.g., Kornei et al. 2010; Hayes et al. 2011; Wofford et al. 2013; Borthakur et al. 2014; Rivera-Thorsen et al. 2015; Trainor et al. 2015; Reddy et al. 2016b; Steidel et al. 2018; Jaskot et al. 2019).

As noted elsewhere, however, the depths of saturated low-ionization metal absorption lines may underestimate the covering fraction of H I (Henry et al. 2015; Vasei et al. 2016; Reddy et al. 2016b; Gazagnes et al. 2018): these lines are not sensitive to metal-poor and possibly less dense gas. The H I absorption lines provide the most direct probe of the covering fraction if the lines are saturated. Large variations in $\mathrm{Ly}\alpha$ forest blanketing along different sight lines render it difficult to

robustly model the interstellar H I lines for all but the highest column density individual (damped Ly α) systems at high redshift. Thus, one must average the FUV spectra across typically $N \gtrsim 25$ independent sight lines to reduce uncertainty in the mean foreground opacity to $\lesssim 10\%$ (Reddy et al. 2016b; Steidel et al. 2018).

For the most part, analyses of composite spectra of highredshift galaxies, as well as the spectra of individual Ly α emitting (and LyC-leaking) local galaxies, imply a picture where Ly α and LyC photons that emerge along the line of sight (or down the barrel of the galaxy) do so after escaping the ISM through low column density channels in an otherwise optically thick (ionization-bounded) medium (Trainor et al. 2015; Dijkstra et al. 2016; Reddy et al. 2016b; Gazagnes et al. 2018; Chisholm et al. 2018; Steidel et al. 2018; Trainor et al. 2019; Gazagnes et al. 2020). Other studies of local galaxies with high equivalent width optical emission lines (such as "Green Pea" galaxies) find a high covering fraction of H I with \sim unity optical depth, where the column density modulates Ly α escape (Henry et al. 2015; Jaskot et al. 2019). There are yet other studies that have suggested that density-bounded conditions indicated by very high [O III]/[O II] may favor the escape of LyC and Ly α photons (e.g., Nakajima et al. 2013; Nakajima & Ouchi 2014; Jaskot & Oey 2013; Tang et al. 2019).

In general, galaxies are likely better visualized not as a single HII region but as many overlapping regions, with a complicated ISM structure as a consequence. Thus, all of the aforementioned conditions could be present even in an individual galaxy: e.g., some sight lines through the galaxy may be ionization bounded, others may be density bounded, while still others may be something in between (HI gas with ~unity optical depth; see also Kakiichi & Gronke 2021). If this is the case, averaging over many galaxies (and hence many sight lines) will result in an average (composite) spectrum that appears consistent with an ionization-bounded and porous ISM, i.e., a nonunity covering fraction of optically thick gas (Reddy et al. 2016b). One also expects the visibility of Ly α (and LyC) emission to be highly dependent on the orientation of the galaxy relative to the line of sight (e.g., Ma et al. 2016). At any rate, modeling of FUV spectra can elucidate the predominant pathways by which Ly α and LyC photons escape the ISM of galaxies (e.g., Henry et al. 2015; Reddy et al. 2016b; Steidel et al. 2018; Gazagnes et al. 2018, 2020).

Galaxies at redshifts $2.0 \lesssim z \lesssim 2.6$ are uniquely suited for studying the production and transmission of Ly α photons: the FUV is shifted to observed wavelengths where the sky background is extremely low and the throughput of blue-optimized ground-based spectrographs is high, typical star-forming galaxies are sufficiently bright to enable detailed studies of individual objects (Reddy & Steidel 2009), the relative transparency of the foreground intergalactic medium (IGM) allows for constraints on the gas covering fraction for ensembles of objects (Reddy et al. 2016b), and the full suite of strong optical emission lines used to diagnose the state of the ISM are shifted to the near-IR windows of atmospheric transmission.

In this paper, we investigate the role of stellar population and gas covering fraction in the production and escape of Ly α (and LyC) photons using a sample of 136 typical star-forming galaxies at redshifts 1.85 \leq z \leq 3.49 with deep FUV and optical spectra from the MOSFIRE Deep Evolution Field (MOSDEF)

survey (Kriek et al. 2015). Our analysis expands on previous efforts (e.g., Steidel et al. 2016; Topping et al. 2020a; Cullen et al. 2020) by jointly modeling FUV and optical composite spectra—including the interstellar HI absorption lines—constructed in bins of Ly α equivalent width and star-formationrate (SFR) surface density. The galaxies were targeted for optical and subsequent FUV spectroscopy independent of FUV or optical emission-line strength and, as such, constitute a sample that is particularly advantageous in the current context. While targeted searches of LAEs and other high equivalent width optical line emitters provide a means of efficiently selecting galaxies that contribute significantly to cosmic reionization, they lack the dynamic range in galaxy properties to properly evaluate the physical factors modulating the emission lines and escape of Ly α and ionizing photons. To address the question of why certain galaxies have strong Ly α emission and others do not, one would clearly want to obtain spectroscopy in a controlled way for many galaxies spanning a range of Ly α strength. Moreover, the availability of deep Hubble Space Telescope (HST) imaging in the fields targeted by MOSDEF allows for an exploration of how the compactness of star formation impacts the porosity of the ISM and the escape of Ly α and ionizing photons (e.g., Heckman et al. 2011; Verhamme et al. 2017; Marchi et al. 2019; Naidu et al. 2020).

The outline of this paper is as follows. The MOSDEF survey, follow-up Keck/LRIS FUV spectroscopy and data reduction, individual galaxy measurements, and construction of composite spectra are described in Section 2. Section 3 presents the procedures for fitting the composite FUV spectra and optical emission-line ratios with stellar population synthesis (SPS) and photoionization models, respectively, and the correlations between Ly α equivalent width and parameters relating to the ionizing spectrum (e.g., stellar metallicity, age), state of the ionized ISM (e.g., ionization parameter, gas-phase oxygen abundance), and the configuration of the neutral ISM (e.g., H I column density and covering fraction). The role of the shape of the ionizing spectrum and gas covering fraction on Ly α escape and the impact of the SFR surface density and galaxy potential well on the escape of Ly α and the ionization parameter are discussed in Section 4. We summarize the analysis and our conclusions in Section 5. Unless indicated otherwise, quoted wavelength ranges (e.g., EUV, FUV, and optical) refer to the rest frame. All equivalent widths are expressed in the rest frame. A Chabrier (2003) IMF is considered throughout the paper. Magnitudes are on the AB system (Oke & Gunn 1983). We adopt a cosmology with $H_0 = 70 \text{ km s}^{-1} \text{ Mpc}^{-1}, \ \Omega_{\Lambda} = 0.7, \text{ and } \Omega_{\text{m}} = 0.3.$

2. Sample Selection and Observations

2.1. The MOSDEF Survey

Galaxies analyzed here were drawn from the MOSDEF survey. This survey obtained moderate-resolution ($R \sim 3000-3600$) rest-frame optical spectroscopy of $\approx 1500~H$ -band-selected galaxies and active galactic nuclei (AGNs) at redshifts $1.4 \lesssim z \lesssim 3.8$ in the CANDELS fields (Grogin et al. 2011; Koekemoer et al. 2011) using the MOSFIRE spectrometer (McLean et al. 2012) on the Keck telescope. MOSDEF galaxies were selected for spectroscopy based on preexisting photometric, grism, or spectroscopic redshifts ($z_{\rm spec}$)—z = 1.37-1.70, z = 2.09-2.70, and z = 2.95-3.80—that place the strong rest-frame optical emission lines (e.g., [O III], H β , [O III],

 ${\rm H}\alpha$, [N II]) in the *YJHK* atmospheric transmission windows. Details of the spectroscopic data reduction are provided in Kriek et al. (2015). The final spectroscopic sample spans ranges of SFR (1 M_{\odot} yr⁻¹ \lesssim SFR \lesssim 200 M_{\odot} yr⁻¹) and stellar mass (10⁹ $M_{\odot} \lesssim M_{*} \lesssim 10^{11}$ M_{\odot}) typical for galaxies at $z \sim 1.4-3.8$, with the majority of galaxies in the sample having detections of multiple rest-frame optical emission lines. Optical line luminosities were calculated using the methodology presented in Kriek et al. (2015).

2.2. MOSDEF-LRIS FUV Spectroscopy

Optical spectra from MOSDEF were complemented with FUV spectra obtained using the Low Resolution Imaging Spectrometer (LRIS; Oke et al. 1995; Steidel et al. 2004) on the Keck telescope. Objects from the parent MOSDEF spectroscopic sample in the AEGIS, COSMOS, GOODS-N, and GOODS-S fields were prioritized for LRIS spectroscopy in the following manner. Objects with detections of H β , [O III], H α , and [N II] were given the highest priority, and those with detections of the first three of these lines and an upper limit on [NII] were given the next-highest priority. We then included the following in order of priority: objects with MOSDEF redshifts $2.0 \leqslant z_{\text{spec}} \leqslant 2.7$, $1.4 \leqslant z_{\text{spec}} \lesssim 1.7$, or $3.0 \leqslant z_{\rm spec} \leqslant 3.8$; those for which we were unable to obtain a redshift with MOSFIRE; and finally objects not observed with MOSFIRE, but which have photometric or grism redshifts from the 3D-HST survey that place them in the redshift ranges—and which meet the limit in *H*-band magnitude—targeted by MOSDEF.

Slit masks were milled with 1"2 width slits and, to ensure proper background subtraction, a minimum slit length of 9". A total of 259 objects (217 of which have z_{spec} from MOSFIRE) were observed using nine slit masks in the AEGIS, COSMOS, GOODS-N, and GOODS-S fields. The observations were obtained over 10 nights in five separate observing runs during the period 2017 January-2018 June. Spectra were obtained with the blue and red channels of LRIS (LRIS-B and LRIS-R, respectively), with the incoming beam split at $\simeq 5000 \,\text{Å}$ using the d500 dichroic. LRIS-B and LRIS-R were configured with the 400 line mm⁻¹ grism and the 600 line mm⁻¹ grating blazed at 5000 Å, respectively. The red-side grating was tilted so that the combined LRIS-B and LRIS-R spectrum for each galaxy has continuous wavelength coverage from the atmospheric cutoff at $\lambda \simeq 3100 \,\text{Å}$ to $\gtrsim 7000 \,\text{Å}$, with the reddest covered wavelength depending on the position of the slit within the LRIS spectroscopic field of view. This setup yielded blue and red spectral resolutions of $R \sim 800$ and $R \sim 1400$, respectively, for a typical seeing of around 0.18. Total exposure times varied from 6 to 11 hr, with a median of 7.5 hr. In addition to internal flats on the red side, we obtained sky flats taken in twilight on the blue side, as they provide better illumination than the internal flats at $\lambda \lesssim 4000$ Å. Arc spectra from Cd, Ar, Zn, He, and Hg internal lamps were acquired for wavelength calibration, and spectroscopic flux standards were observed at different air masses on all observing runs to aid in flux calibration. LRIS data were reduced using the procedures described in Steidel et al. (2018) and Topping et al. (2020a).

2.3. Individual Galaxy Measurements

2.3.1. Redshifts

The procedure used to derive redshifts for Ly α emission and each of the strongest interstellar low-ionization metal absorption lines in the LRIS spectra—Si II λ 1260, O I λ 1302+Si II λ 1304,

C II λ 1334, S II λ 1526, Fe II λ 1608, and Al II λ 1670—is described in Topping et al. (2020a). Briefly, the redshift of each line was calculated by fitting the local continuum and the line with a quadratic and Gaussian function, respectively, and taking the centroid of the Gaussian function as the observed wavelength of the line. These fits were manually inspected, and only those lines with satisfactory fits were used to derive the final Ly α emission line and interstellar absorption-line redshifts, $z_{\rm Ly}\alpha$ and $z_{\rm IS}$, respectively.

The spectra were shifted to the rest frame using systemic redshifts, z_{sys} , which were measured from the highest signal-tonoise ratio (S/N) optical nebular emission lines (i.e., typically $[O III] \lambda 5008$ or $H\alpha$) in the MOSFIRE spectra, as described in Kriek et al. (2015). For the 21 (of 259) objects in the sample that did not have a spectroscopic redshift from MOSFIRE—either because a robust redshift identification was not possible or because the object had not been previously targeted in the MOSDEF survey— z_{sys} was estimated from $z_{Ly\alpha}$ and/or z_{IS} using the relationships between $z_{\rm sys}$, $z_{\rm Ly\alpha}$, and $z_{\rm IS}$ for those objects where both $z_{\rm sys}$ and at least one of $z_{\rm Ly\alpha}$ or $z_{\rm IS}$ were available (see Topping et al. 2020a). There were an additional three objects in the sample that did not have redshifts from MOSFIRE and for which we were unable to derive redshifts from the LRIS spectra, usually because the LRIS spectrum either was too noisy or contained irreparable artifacts that prevented a robust redshift identification. The redshift and near-IR magnitude distributions of the MOSDEF-LRIS sample, relative to those of the parent MOSDEF sample, are presented in the top panel of Figure 1. The few objects fainter than the H = 24.0, 24.5, and 25.0 mag limits imposed for MOSDEF target selection in the z = 1.37 - 1.70, z = 2.09 - 2.70, and z = 2.95 - 3.80 redshift windows, respectively, are serendipitous objects that happened to fall on MOSFIRE slits and for which we were able to derive robust redshifts.

2.3.2. Ly α Equivalent Widths, $W_{\lambda}(Ly\alpha)$

One of the basic parameters in this study is the equivalent width of Ly α , W_{λ} (Ly α). This quantity scales with the escape fraction of Ly α photons and thus depends on the intrinsic ionizing photon production rate and gas covering fraction. $W_{\lambda}(Ly\alpha)$ was measured for each galaxy following the procedures given in Kornei et al. (2010) and Du et al. (2018). Errors in $W_{\lambda}(Ly\alpha)$ were calculated by remeasuring $W_{\lambda}(Ly\alpha)$ for many realizations of each spectrum based on the corresponding error spectrum. Note that $W_{\lambda}(Ly\alpha)$ only includes the emission measured within the spectroscopic aperture, adjusted for slit loss by assuming that the emission is spatially coincident with the nonionizing FUV continuum (Section 2.2). $W_{\lambda}(Ly\alpha)$ does not include the fraction of Ly α scattered out of the spectroscopic aperture (e.g., Steidel et al. 2011). As discussed in Section 3.3.2, the spectroscopically determined $W_{\lambda}(Ly\alpha)$ is the one most relevant for identifying ISM configurations that are amenable for the escape of Ly α (and ionizing) photons. Throughout this work, $W_{\lambda}(Ly\alpha)$ refers to the rest-frame value and is positive for Ly α in emission. In Section 4.1, we consider an alternative method for computing Ly α equivalent widths that accounts for underlying interstellar and stellar absorption.

2.3.3. Broadband SED Modeling

To aid in accounting for stellar Balmer absorption when measuring line luminosities, as well as determining SFRs (SFR

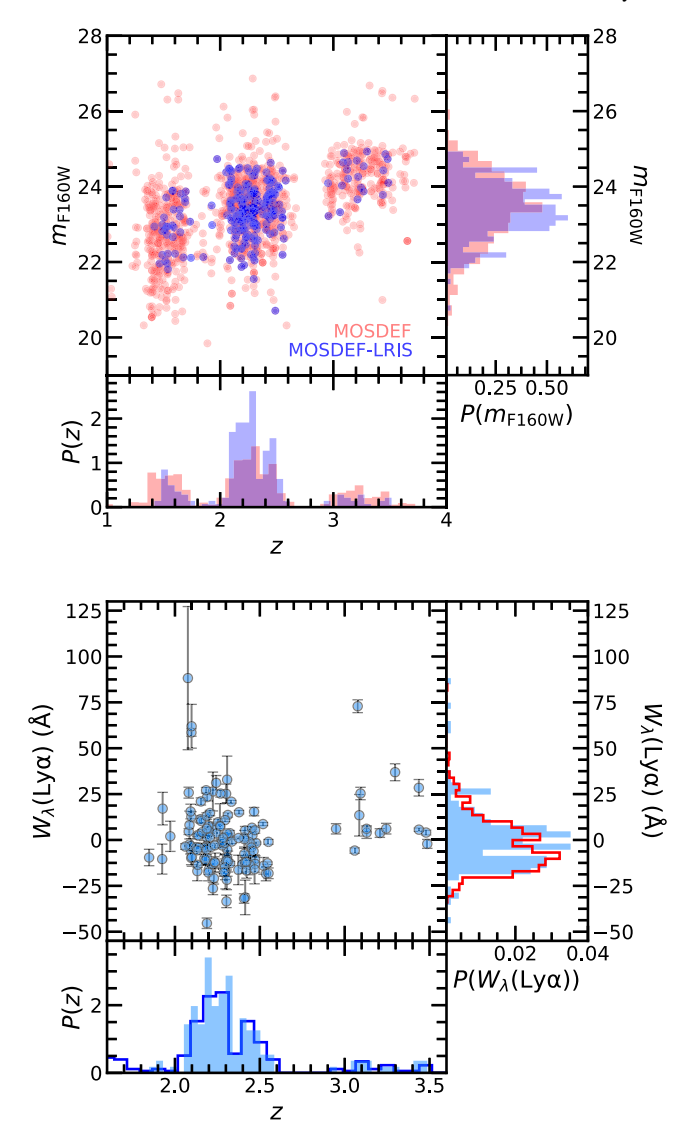


Figure 1. Top: joint magnitude and redshift distributions of the MOSDEF-LRIS sample (blue circles) and the parent MOSDEF sample (red circles). The histograms show the probability density, normalized so that the total area below the histograms is equal to unity, as a function of redshift (bottom subpanel) and magnitude (right subpanel). Bottom: joint $W_{\lambda}(\text{Ly}\alpha)$ and redshift distributions for the final sample of 136 objects used in this work (blue circles). The bottom subpanel shows the redshift probability density histogram for the final sample (shaded blue) and that of the entire MOSDEF-LRIS sample (blue outline). The right subpanel shows the $W_{\lambda}(\text{Ly}\alpha)$ probability density distribution for the final sample (shaded blue) and that of 978 objects from the UV-selected KBSS survey of star-forming galaxies at similar redshifts (red outline).

(SED)), stellar masses (M_*) , ages, and continuum reddening $(E(B-V)_{\rm cont})$, we fit the broadband photometry of galaxies in the sample with the Binary Population and Spectral Synthesis (BPASS) version 2.2.1 models (Eldridge et al. 2017; Stanway & Eldridge 2018). Our choice of these models is motivated by recent studies (e.g., Steidel et al. 2016) that jointly model FUV and optical spectra and find that the FUV and optical line luminosity ratios of typical star-forming galaxies at $z \sim 2$ are best reproduced when incorporating the physics of stellar binarity. The BPASS distribution conveniently includes model predictions both with and without the effects of stellar binarity, as well as for two different cutoffs of the high-mass end of the IMF, 100 and $300\,M_\odot$. The resulting four variations of the BPASS models are considered in the present analysis: binarity with an upper mass cutoff of $100\,M_\odot$ ("100bin"), binarity with

an upper mass cutoff of $300\,M_\odot$ ("300bin"), single-star evolution with an upper mass cutoff of $100\,M_\odot$ ("100sin"), and single-star evolution with an upper mass cutoff of $300\,M_\odot$ ("300sin"). We refer to these four flavors of models as the BPASS model "types."

The instantaneous burst models provided in the BPASS distribution were summed to produce constant star formation models for $\log[{\rm Age/yr}] = 7.0{\text -}10.0$ in 0.1 dex increments. The $Z_* = 0.001$ metallicity models were considered in fitting the broadband photometry, based on the results obtained when directly fitting the BPASS models to the FUV spectra (Section 3.1). Nebular continuum emission was added to the SPS models as described in Section 3.1.1. Based on the analysis presented in Appendix A (see also Section 3.1), the SMC (Gordon et al. 2003) dust extinction curve was assumed for the reddening of the stellar continuum.

The broadband photometry for each galaxy (as compiled in Skelton et al. 2014) was first corrected for contributions from the optical emission lines and Ly α . The corrected photometry was then fit with the aforementioned models, limiting the age to be less than the age of the universe at the redshift of each galaxy and greater than the minimum dynamical timescale of $\simeq 10$ Myr inferred for the most compact galaxies in the sample (e.g., Reddy et al. 2012b; Price et al. 2016, 2020). The model parameters that yielded the lowest χ^2 relative to the photometry were taken to be the best-fit values. Errors in the parameters were determined from the standard deviation of parameter values obtained when fitting many perturbed realizations of the photometry based on the photometric errors. Unless indicated otherwise, the SED-fitting results obtained with the 100bin models and the SMC extinction curve are adopted by default (see Section 3.1.1 and Appendix A for further discussion on the choice of the stellar reddening curve).

2.4. Final Sample

Several criteria were applied to the targeted set of 259 objects in the MOSDEF-LRIS survey to arrive at the final sample for analysis. Any objects for which the LRIS spectra contained irreparable artifacts that prevented a robust redshift identification, or that were too noisy to yield a redshift ($z_{Lv\alpha}$ or $z_{\rm IS}$), were removed. AGNs identified using the IR, X-ray, and optical line flux criteria described in Coil et al. (2015), Azadi et al. (2017, 2018), and Leung et al. (2019) were removed. Examination of the LRIS spectra of the remaining objects did not reveal the presence of any additional luminous AGN (e.g., such as those identified by broad Ly α emission or significant N V or C IV emission). Any objects for which the MOSFIRE or LRIS spectra indicate that the target may be blended with a foreground object were removed. The combined telescope and instrumental sensitivity of LRIS-B with the 400 line mm⁻¹ grism falls below $\simeq 20\%$ at $\lambda \lesssim 3300$ Å. As such, any objects for which Ly α falls at bluer wavelengths (i.e., $z_{\text{sys}} < 1.7$) were removed. These criteria result in a final sample of 136 galaxies, whose redshift and $W_{\lambda}(Ly\alpha)$ distributions are indicated in the bottom panel of Figure 1—of these, 79 galaxies have complete coverage of the strong optical nebular emission lines. The redshift distribution is statistically similar to that of the full MOSDEF-LRIS sample, while the $W_{\lambda}(Ly\alpha)$ distribution is statistically similar to that of the Keck Baryonic Structure Survey (KBSS) sample distribution for UV-selected galaxies at similar redshifts (Reddy et al. 2008; Steidel et al. 2018). The percentage of galaxies with $W_{\lambda}(Ly\alpha) > 20$ Å, the criterion that defines a Ly α emitter (LAE), is 12.5% (17 of 136 galaxies). This percentage agrees well with the 12% found for star-forming galaxies selected by their FUV colors to lie at similar redshifts, i.e., "BX"-selected galaxies, with $\mathcal{R}_s \leqslant$ 25.5 (Reddy et al. 2008).

2.5. FUV and Optical Composite Spectra

Higher-S/N measurements and inferences of mean spectral properties were obtained by averaging individual galaxy spectra to produce composite spectra. The procedures used for constructing composite FUV and optical spectra are specified in Reddy et al. (2016a) and Reddy et al. (2020), respectively, and are summarized here. Galaxies were first grouped together based on a certain property of interest (e.g., $W_{\lambda}(\mathrm{Ly}\alpha)$, SFR surface density). The FUV and optical spectra for all galaxies in a given grouping were shifted to the rest frame based on z_{sys} , converted to units of luminosity density, and spline-interpolated to a linear wavelength grid with a spacing $\delta\lambda_0 = 0.5$ Å. At each grid wavelength point, the luminosity densities were averaged after rejecting values that differ from the median luminosity density by more than 3σ .

No weighting was applied in the averaging to ensure that every galaxy contributes equally to the composite spectrum and that the predicted mean IGM+CGM opacity—which is computed assuming that all sight lines contribute equally to the mean decrement shortward of Ly α —can be confidently used to correct the composite spectrum (Steidel et al. 2018). The foreground IGM+CGM transmission curve appropriate for the mean redshift of the galaxies forming the composite spectrum was derived from the $N({\rm H~I})$ distribution of intervening absorbers as a function of redshift given in Rudie et al. (2013) (e.g., Shapley et al. 2006; Reddy et al. 2016b; Steidel et al. 2018). The composite FUV spectrum was divided by this transmission curve to correct for the mean foreground IGM +CGM opacity.

The error in the mean luminosity density at each dispersion point (i.e., the composite error spectrum) reflects both measurement uncertainties (from the error spectra for individual objects) and the variance in luminosity densities of objects contributing to each dispersion point. The composite FUV and optical spectra for the entire sample are presented in Figure 2.

Table 1 lists the subsets of the sample for which composite spectra were constructed, along with the number of objects in each subset and their mean redshifts and $W_{\lambda}(\text{Ly}\alpha)$. For reference, the latter were calculated by simply averaging the individual $W_{\lambda}(\text{Ly}\alpha)$ measurements of the galaxies composing the subsets (Section 2.3.2). The $\langle W_{\lambda}(\text{Ly}\alpha)\rangle$ measured directly from the composite spectra using the procedure described in Kornei et al. 2010) are systematically lower by \simeq 7 Å than those computed from the individual measurements owing to the presence of significantly detected interstellar H I absorption

The method of normalizing each individual galaxy spectrum by the luminosity of the most frequently detected (or highest-S/N) line of a line ratio can be used to ensure that a line ratio measured from a composite spectrum is mathematically identical to the average of individual galaxy line ratios. However, normalizing individual galaxy spectra in this manner prevents the inclusion of galaxies where the normalizing line may be undetected and complicates the IGM+CGM opacity correction to the composite FUV spectrum. As a result, we do not normalize the spectra in this manner, opting instead to check that the line ratios measured from the composite spectra are consistent with the average of individual galaxy line ratios within the measurement uncertainties of those ratios. This is the case for all of the line ratios measured from composite spectra of galaxies where all of the relevant lines are detected individually.

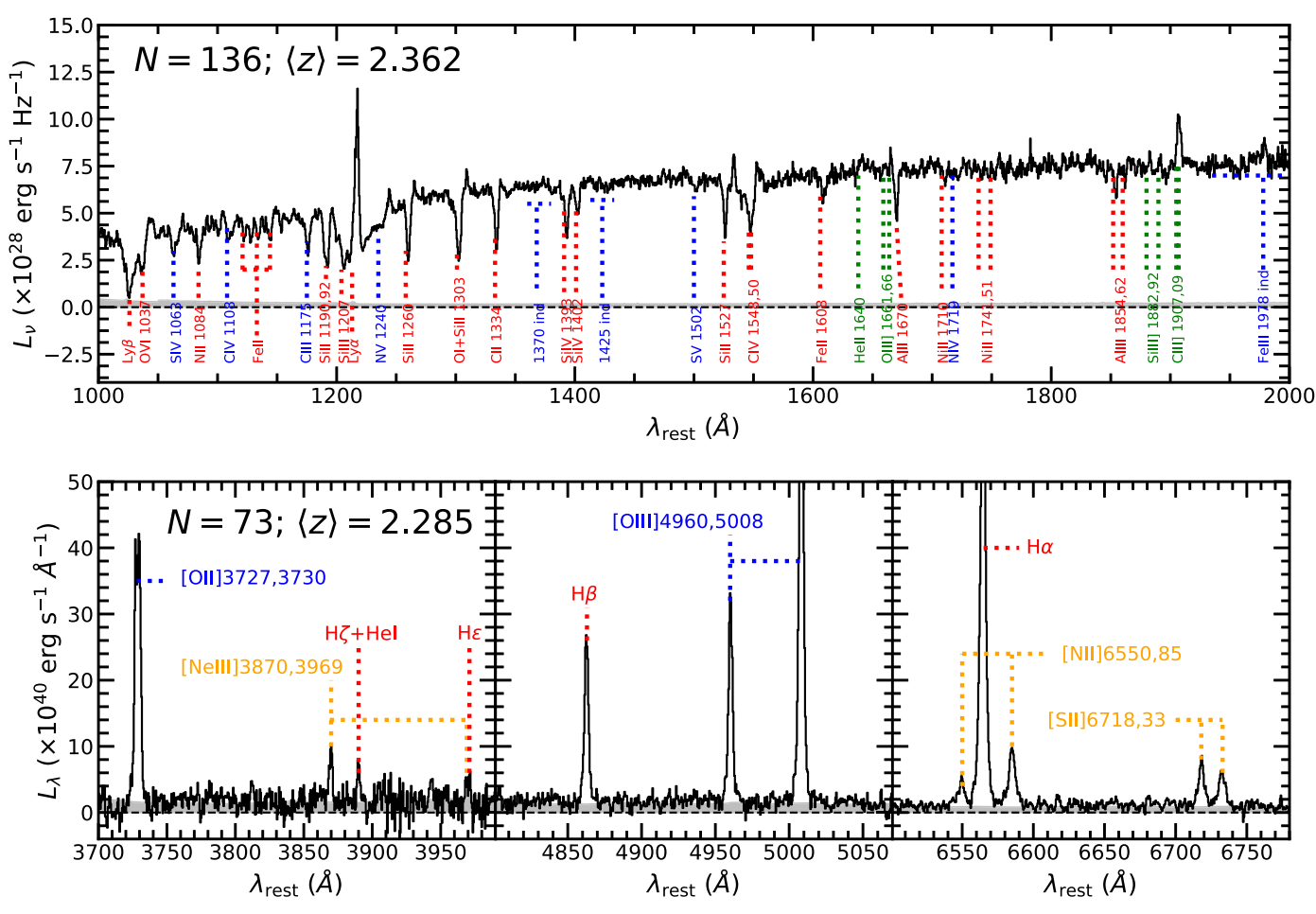


Figure 2. Top: composite FUV spectrum (based on the LRIS spectroscopic observations) for the N=136 galaxies in the sample with a mean redshift of $\langle z \rangle = 2.362$. The spectrum has been corrected for the combined IGM and CGM opacity appropriate for the mean redshift of galaxies contributing to the composite spectrum. Labeled are some of the prominent features in the spectrum, including stellar absorption (blue), nebular emission (green), and interstellar absorption (red). C IV, Si IV, and O VI also include stellar wind absorption. Bottom: composite optical spectrum (based on the MOSFIRE spectroscopic observations) for the N=73 galaxies ($\langle z \rangle = 2.285$) in the subsample with complete wavelength coverage of the strong optical emission lines, including [O II] $\lambda\lambda 3727$, 3730, [Ne III] $\lambda\lambda 3870$, 3969, H β , [O III] $\lambda\lambda 4960$, 5008, H α , [N II] $\lambda\lambda 6550$, 6585, and [S II] $\lambda\lambda 6718$, 6733. The prominent oxygen emission lines (blue), H I Balmer recombination emission lines (red), and other nebular emission lines (orange) are shown. In both panels, the light-gray region indicates the composite error spectrum.

underlying the Ly α emission line in the composite spectra (e.g., as seen in Figure 2). Consequently, while $\langle W_{\lambda}(\mathrm{Ly}\alpha) \rangle$ is relatively straightforward to compute, differences in exactly how it is calculated can lead to some ambiguity in its relation to the production and escape of Ly α photons. Thus, the $W_{\lambda}(\mathrm{Ly}\alpha)$ of the emission line itself, $W_{\lambda}^{\mathrm{em}}(\mathrm{Ly}\alpha)$, and the escape fraction of Ly α photons, $f_{\mathrm{esc}}^{\mathrm{spec}}$ (Ly α), are also considered below (Section 4.1).

3. Modeling of the Composite FUV and Optical Spectra

A central focus of this analysis is to identify the primary factors in the production and transmission of $Ly\alpha$ (and LyC) photons. For the most part, these factors are constrained by fitting SPS and simplified ISM models to composite FUV spectra and through photoionization modeling of nebular emission lines in the composite optical spectra. The fitting proceeded in three steps. In the first step, the BPASS models were fit to the composite FUV spectra to constrain stellar metallicities, ages, and continuum reddening of the stellar population dominating the FUV light. In the second step, photoionization modeling of the emission-line ratios measured from the composite optical spectra was used to deduce

ionization parameters, gas-phase oxygen abundances, and nebular reddening. Additionally, the residual He II λ 1640 nebular emission in the composite FUV spectra was used to constrain the BPASS model type (i.e., the high-mass cutoff of the IMF and stellar binarity). The parameters obtained in the first two fitting steps determine the shape of the ionizing spectrum. In the third step, models of the neutral ISM were fit to the composite FUV spectra to infer the line-of-sight reddening, H I column densities, and H I covering fractions. These three steps—and the correlations between $W_{\lambda}(\text{Ly}\alpha)$ and the aforementioned parameters—are described, respectively, in Sections 3.1, 3.2, and 3.3. The fitting results are summarized in Section 3.4. Readers who wish to skip the details of the fitting procedures can proceed to Section 3.4.

3.1. SPS Modeling and Results

3.1.1. SPS Modeling Procedure

Composite FUV spectra were fit with the BPASS 100bin, 300bin, 100sin, and 300sin SPS models (see Section 2.3.3) using a methodology similar to that presented in Steidel et al. (2016) and Topping et al. (2020a), with a few modifications described below. Similar to the aforementioned studies, we

Table 1
Subsample Construction and Statistics

| Subsample | Criteria ^a | N^{b} | $\langle z_{\rm sys} \rangle^{\rm c}$ | $\langle W_{\lambda}(\mathrm{Ly}\alpha)\rangle \ (\mathring{\mathrm{A}})^{\mathrm{d}}$ |
|-----------|--|------------------|---------------------------------------|--|
| A | All | 136 | 2.362 | 1.09 ± 0.46 |
| AL | All, Ly β | 118 | 2.410 | -0.79 ± 0.37 |
| ALN | All, Ly β , neb | 73 | 2.285 | -3.42 ± 0.47 |
| WT1 | $W_{\lambda}(Ly\alpha)$, T1 | 45 | 2.298 | -15.88 ± 0.71 |
| WT1L | $W_{\lambda}(Ly\alpha)$, T1, Ly β | 39 | 2.326 | -16.89 ± 0.76 |
| WT1LN | $W_{\lambda}(Ly\alpha)$, T1, Ly β , neb | 24 | 2.311 | -19.13 ± 0.97 |
| WT2 | $W_{\lambda}(Ly\alpha)$, T2 | 45 | 2.371 | -0.98 ± 0.38 |
| WT2L | $W_{\lambda}(Ly\alpha)$, T2, Ly β | 39 | 2.368 | -1.56 ± 0.38 |
| WT2LN | $W_{\lambda}(Ly\alpha)$, T2, Ly β , neb | 24 | 2.284 | -4.72 ± 0.63 |
| WT3 | $W_{\lambda}(Ly\alpha)$, T3 | 46 | 2.417 | 19.72 ± 1.12 |
| WT3L | $W_{\lambda}(Ly\alpha)$, T3, Ly β | 40 | 2.533 | 15.67 ± 0.72 |
| WT3LN | $W_{\lambda}(Ly\alpha)$, T3, Ly β , neb | 25 | 2.260 | 12.92 ± 0.82 |
| ST1 | $\Sigma_{\rm SFR(H\alpha)}$, T1 | 26 | 2.305 | -2.20 ± 0.99 |
| ST1L | $\Sigma_{SFR(H\alpha)}$, T1, Ly β | 24 | 2.325 | -5.32 ± 0.90 |
| ST2 | $\Sigma_{\rm SFR(H\alpha)}$, T2 | 26 | 2.266 | -2.24 ± 0.68 |
| ST2L | $\Sigma_{SFR(H\alpha)}$, T2, Ly β | 24 | 2.292 | -2.84 ± 0.76 |
| ST3 | $\Sigma_{\rm SFR(H\alpha)}$, T3 | 28 | 2.274 | 0.76 ± 0.59 |
| ST3L | $\Sigma_{\rm SFR(H\alpha)}$, T3, Ly β | 25 | 2.283 | -1.58 ± 0.60 |
| sST1 | $\Sigma_{\rm sSFR(H\alpha)}$, T1 | 26 | 2.281 | -0.88 ± 1.04 |
| sST1L | $\Sigma_{\rm sSFR(H\alpha)}$, T1, Ly β | 24 | 2.297 | -3.88 ± 0.96 |
| sST2 | $\Sigma_{\rm sSFR(H\alpha)}$, T2 | 26 | 2.296 | -6.93 ± 0.69 |
| sST2L | $\Sigma_{\rm sSFR(H\alpha)}$, T2, Ly β | 24 | 2.314 | -7.19 ± 0.74 |
| sST3 | $\Sigma_{\rm sSFR(H\alpha)}$, T3 | 28 | 2.268 | 3.89 ± 0.51 |
| sST3L | $\Sigma_{\rm sSFR(H\alpha)}$, T3, Ly β | 25 | 2.289 | 1.22 ± 0.53 |

Notes.

adopted a constant star formation history (SFH). While there exist several different physically relevant models for the SFHs of star-forming galaxies (e.g., Chisholm et al. 2019), we chose a constant SFH based on findings that such an SFH (or slowly rising SFHs) provides a reasonable approximation of the mean SFH of ensembles of typical star-forming galaxies at $z \gtrsim 1.5$ (Papovich et al. 2011; Reddy et al. 2012b). We also considered ages of log[Age/yr] = 7.0, 7.3, 7.5, 7.6, 7.8, 8.0, 8.5, and 9.0.The publicly available BPASS version 2.2.1 distribution includes model spectra computed at stellar metallicities $Z_* = 10^{-5}$ to 0.04, expressed in terms of the mass fraction of metals where, for reference, the solar value is $Z_{\odot} = 0.0142$ (Asplund et al. 2009). The provided spectra were interpolated to construct a new grid of models with Z* that more finely sample (and bracket) the values expected for $z \sim 2$ galaxies (Steidel et al. 2016). Specifically, we considered stellar metallicities of $Z_* = 10^{-4},\ 3\times 10^{-4},\ 5\times 10^{-4},\ 7\times 10^{-4},\ 9\times 10^{-4},\ 0.0010,\ 0.0012,\ 0.0014,\ 0.0016,\ 0.0018,\ 0.0020,$ 0.0022, 0.0024, 0.0026, 0.0028, and 0.0030. Thus, we obtain a grid of SPS models with different stellar metallicities and ages. Nebular continuum emission was added to each SPS model in the grid (as described in Topping et al. 2020a) to produce an "SPSneb" model.

Finally, because of the lower resolution of the blue-side LRIS spectra relative to the red-side spectra (Section 2.2), the SPSneb models were smoothed to match the resolution of the former at $\lambda_0 < 1500\,\text{Å}$, corresponding to the rest-frame wavelength of the dichroic cutoff for the mean redshift of the sample, $\langle z \rangle \sim 2.3$. No smoothing was applied at wavelengths redder than 1500 Å.

Appendix A presents a comparison of the SFRs obtained with the different continuum attenuation curves, SFR(SED), and those derived from ${\rm H}\alpha$, SFR(H α). This comparison indicates that only the SMC extinction curve results in UV-based SFRs fully consistent with the H α -based ones for the galaxy ensembles considered in this study, irrespective of the BPASS model type (100bin, 300bin, 100sin, and 300sin models; see also Theios et al. 2019). Thus, the SMC extinction curve—updated in the wavelength range $\lambda=950-1250\,{\rm \AA}$ based on the analysis of Reddy et al. (2016a)—was assumed in fitting the SPSneb models to the composite FUV spectra. Each SPSneb model was reddened assuming a range of stellar continuum reddening $E(B-V)_{\rm cont}=0.00-0.40$. The χ^2 of each model of a given Z_* , age, and reddening is

$$\chi^2 = \sum_i \left[\frac{l(i) - m(i)}{\sigma(i)} \right]^2,\tag{1}$$

where l(i) is the luminosity density of the composite FUV spectrum, m(i) is the luminosity density of the model spectrum, and $\sigma(i)$ is the error in luminosity density, at wavelength point i. Wavelength points in the "Mask 1" windows given in Steidel et al. (2016) were used in computing the χ^2 statistic, and only for those windows for which all galaxies in the composite spectrum have coverage. Furthermore, the model spectrum was normalized to have the same median luminosity density as the composite FUV spectrum in the Mask 1 windows—the normalization of the model yields an estimate of the SFR. The best-fit values of Z_* , age, reddening, and SFR were set equal to the mean values obtained when fitting many realizations of the composite spectrum generated through random sampling of the galaxy spectra with replacement. Uncertainties in parameters were conservatively set equal to the standard deviation of the values obtained by fitting these realizations—which are larger than the standard errors in the mean values—and are thus effectively marginalized over the uncertainties of other fitted parameters. This method of deriving the uncertainties applies to all of the line measurements and model parameters obtained in this work.

3.1.2. Modeling Constraints on Z* and Age

Figures 3 and 4 show the 100bin SPSneb model fits to the composite FUV spectrum of all the galaxies in our sample. ¹⁰

^a Criteria used to construct the subsamples: those with "Ly β " include only galaxies with coverage of Ly β absorption (i.e., $z_{\rm sys} > 2.12$), while those with "Ly β , neb" include only galaxies with coverage of Ly β absorption and complete coverage of the optical nebular emission lines. Subsamples resulting from dividing a sample into thirds are denoted by T1, T2, and T3, ordered by increasing value of the parameter used to divide galaxies into each subsample. ^b Number of galaxies in the subsample.

^c Average systematic redshift of galaxies in the subsample.

^d Average of individually measured $W_{\lambda}(\mathrm{Ly}\alpha)$ for galaxies contributing to the subsample.

 $^{^{10}}$ The fitting to the composite FUV spectrum of all galaxies was performed by considering the Steidel et al. (2016) Mask 1 windows in the range $\lambda \simeq 1100-1600$ Å, for which all galaxies have wavelength coverage. For illustrative purposes, however, we show the comparison of these fits to the composite spectrum in longer-wavelength windows (right panel of Figure 3) to which galaxies at $z\lesssim 2.6$ primarily contribute. In practice, the fitting performed using all windows is identical to that performed using the subset of windows for which all galaxies have wavelength coverage since the sample is dominated by galaxies at $2.0\lesssim z\lesssim 2.6$.

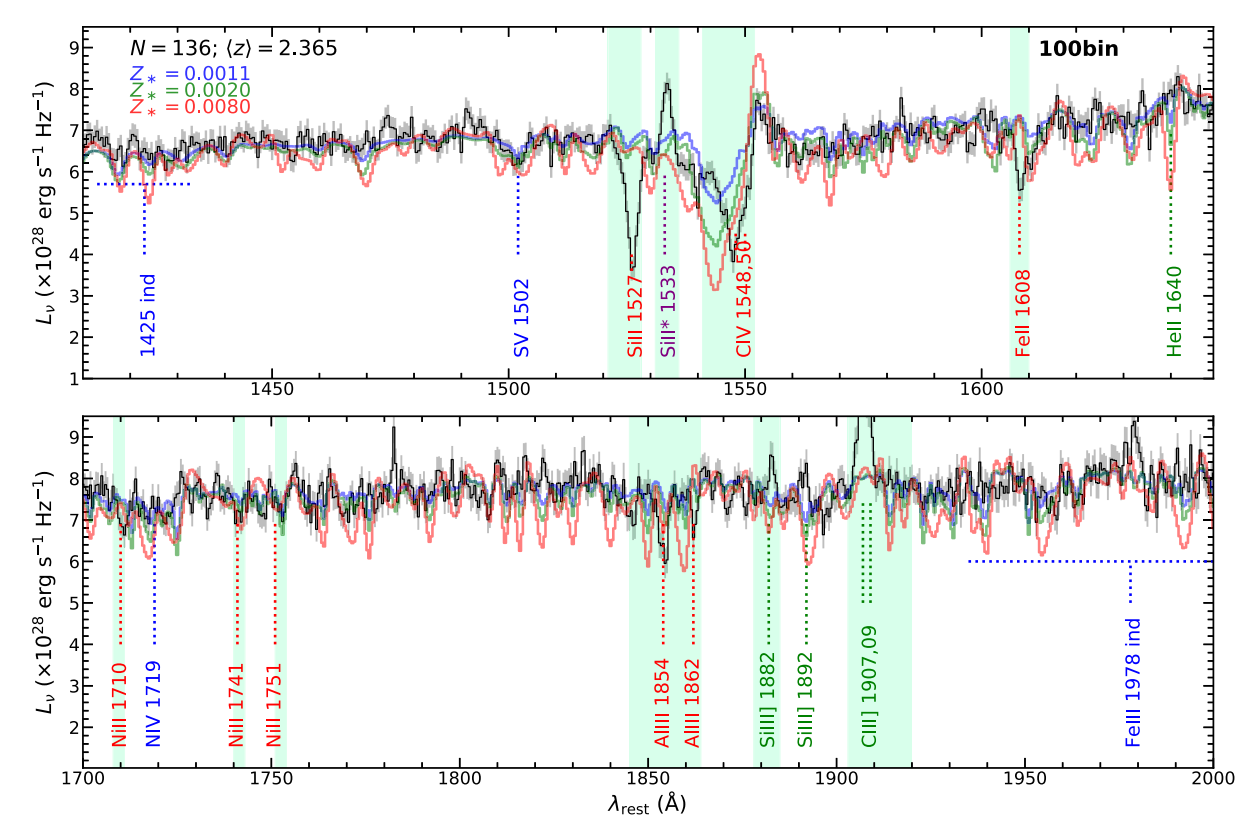


Figure 3. Comparison of the composite FUV spectrum of the entire sample (black, with the 1σ error in gray) and the 100bin SPSneb models for $\log[{\rm Age/yr}] = 8.0$ and different metallicities, focused on the wavelength regions around C IV $\lambda\lambda1548$, 1550 (top) and $\lambda_{\rm rest} = 1700-2000$ Å (bottom). Line labeling is similar to Figure 2, where we include the fine-structure emission line Si II* $\lambda1533$. Regions not included in the fitting are indicated by the light-green shaded regions.

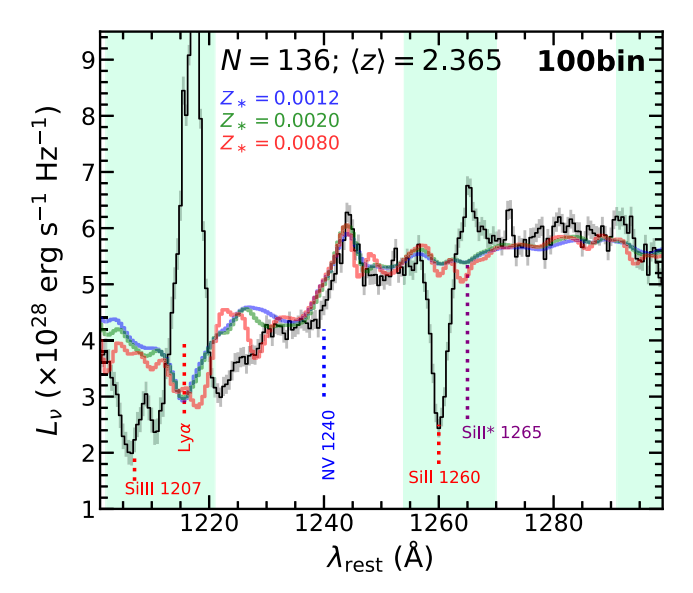


Figure 4. Comparison of the composite FUV spectrum of the entire sample (black, with the 1σ error in gray) and the 100bin SPSneb models for log[Age/yr] = 8.0 and different metallicities, focused on the wavelength region around N v $\lambda1240$. The models shown here do not include interstellar H I absorption. Line labeling is similar to Figure 2, where we include the fine-structure emission line Si II* $\lambda1265$. Regions not included in the fitting are indicated by the light-green shaded regions.

The best-fit continuum reddening, stellar metallicity, and age obtained with the 100bin model are $\langle E(B-V)_{\rm cont}\rangle=0.099\pm0.005,\ \langle Z_*\rangle=0.0011\pm0.0003\ (0.076\pm0.018\,Z_\odot),$ and $\langle \log[{\rm Age/yr}]\rangle=8.0\pm0.2$. This best-fit model is shown

by the blue spectrum. The best-fit models of the same age but with $Z_* = 0.0020$ and $Z_* = 0.0080$ are also shown.

While all the models provide an adequate fit to the NIV λ 1240 P Cygni emission feature (Figure 4), comparison of these models clearly demonstrates the strong preference for lower stellar metallicities when fitting the entire composite FUV spectrum (see also Topping et al. 2020a). For instance, the blend of Si, C, and Fe photospheric lines centered at \simeq 1425 Å (i.e., the 1425 index; Rix et al. 2004); the depths of S V λ 1502 and N V λ 1719; and the Fe III blend centered at \simeq 1978 Å (i.e., the 1978 index; Rix et al. 2004) are all significantly weaker than the predictions of models with $Z_* \gtrsim 0.002$. Moreover, the weak photospheric absorption seen across the full FUV wavelength range (excluding regions affected by interstellar absorption or nebular emission) is most consistent with the $Z_* \lesssim 0.002$ models. Formally, the $Z_* = 0.008$ (≈ 0.56 Z_{\odot}) model is excluded with $\simeq 8\sigma$ significance.

Similar fitting of the composite FUV spectrum of 30 star-forming galaxies at $z \sim 2.3$ from KBSS also indicates a low stellar metallicity, $Z_* \simeq 0.001 - 0.002$ (Steidel et al. 2016; see also Cullen et al. 2019; Topping et al. 2020a, 2020b). Interestingly, the KBSS composite FUV spectrum exhibits very weak C IV P Cygni *emission*, possibly because of blending with interstellar C IV absorption (Steidel et al. 2016). The strong C IV P Cygni emission observed in the composite FUV spectrum of our sample—similar in strength to the predictions of the $Z_* \lesssim 0.002$ models, which best reproduce the overall level of photospheric absorption—may suggest a narrower velocity distribution and/or lower covering fraction of the C IV-bearing gas in the ISM.

The preference for subsolar stellar metallicities persists irrespective of the age of the stellar population (e.g., Topping et al. 2020a). Additionally, the variations in Z_* and age that are obtained with different BPASS model type are negligible compared to the random uncertainties in these parameters (Steidel et al. 2016). Furthermore, Z_* and age are primarily determined by the overall level of photospheric line blanketing in the FUV and, as such, are relatively insensitive to the assumed continuum dust attenuation curve. Because the FUV spectrum is dominated by the light from the youngest stellar populations, the ages derived from the spectral fitting are a factor of $\simeq 2-3$ lower than—but still correlate with—those derived from the broadband SED fitting (Section 2.3.3; see also Section 3.1.3). The former are most relevant for our analysis since the youngest stellar populations dictate the shape of the ionizing spectrum.

3.1.3. Correlations between $W_{\lambda}(Ly\alpha)$ and SPS Model Parameters

The procedure described in Section 3.1.1 was used to fit the composite FUV spectra for subsamples A, AL, and ALN and the nine subsamples constructed in bins of $W_{\lambda}(\mathrm{Ly}\alpha)$ (Table 1). The best-fit values of $\langle E(B-V)_{\mathrm{cont}} \rangle$, $\langle Z_*/Z_{\odot} \rangle$, and $\langle \log[\mathrm{Age/yr}] \rangle$ obtained from fitting the 100bin SPSneb models are listed in Table 2. The variations in $\langle W_{\lambda}(\mathrm{Ly}\alpha) \rangle$ with the aforementioned parameters are presented in Figure 5.

The reddening of the stellar continuum, parameterized by $\langle E(B-V)_{\rm cont} \rangle$, clearly anticorrelates with $\langle W_{\lambda}({\rm Ly}\alpha) \rangle$, such that objects with higher $\langle W_{\lambda}({\rm Ly}\alpha) \rangle$ exhibit significantly bluer $\langle E(B-V)_{\rm cont} \rangle$. The composite FUV spectrum with $\langle W_{\lambda}({\rm Ly}\alpha) \rangle \approx 20~{\rm Å}$ (subsample WT3) has $\langle E(B-V)_{\rm cont} \rangle = 0.073 \pm 0.007$, roughly 0.043 mag bluer than the composite with $\langle W_{\lambda}({\rm Ly}\alpha) \rangle \approx -20~{\rm Å}$ (subsample WT1). Throughout the analysis, we focus on the significance of the difference in the measurements made on composite spectra that contain independent sets of galaxies, such as subsamples formed from the lower and upper third of the $W_{\lambda}({\rm Ly}\alpha)$ distribution of individual galaxies (e.g., subsamples WT1 and WT3, subsamples WT1LN and WT3, and so on).

The top panel of Figure 5 also shows the $E(B-V)_{\rm cont}$ and $W_{\lambda}({\rm Ly}\alpha)$ measured for individual galaxies in the sample, where the former were inferred from broadband SED fitting (Section 2.3.3). The averages of these individual $E(B-V)_{\rm cont}$ measurements in bins of $W_{\lambda}({\rm Ly}\alpha)$ are similar within the uncertainties to the $\langle E(B-V)_{\rm cont} \rangle$ of the composite spectra. The Spearman rank correlation coefficient between $E(B-V)_{\rm cont}$ and $W_{\lambda}({\rm Ly}\alpha)$ for individual galaxies is $\rho_{\rm ind}=-0.31$, with a probability of $p_{\rm ind}=2.6\times 10^{-4}$ that the two variables are uncorrelated.

As noted in Section 3.1.2, the modeling of the composite FUV spectra strongly prefers subsolar stellar metallicities: these metallicities vary from $\langle Z_*/Z_\odot \rangle \simeq 0.07$ to 0.12 for the composites formed in bins of $W_\lambda({\rm Ly}\alpha)$. However, there is no significant correlation between $\langle Z_* \rangle$ and $\langle W_\lambda({\rm Ly}\alpha) \rangle$ for the ensembles analyzed here. For example, the two composites with the most extreme values of $\langle W_\lambda({\rm Ly}\alpha) \rangle$, namely, subsamples WT1LN and WT3, have $\langle Z_*/Z_\odot \rangle = 0.080 \pm 0.021$ and 0.079 ± 0.015 , respectively.

On the other hand, the composite FUV spectra indicate a marginally significant anticorrelation between $\langle \log[{\rm Age/yr}] \rangle$ and $\langle W_{\lambda}({\rm Ly}\alpha) \rangle$. Composites with $\langle W_{\lambda}({\rm Ly}\alpha) \rangle > 0$ have $\langle \log[{\rm Age/yr}] \rangle \lesssim 8.0$, while those with net ${\rm Ly}\alpha$ in absorption have $\langle \log[{\rm Age/yr}] \rangle \gtrsim 8.3$. Formally, the number of degrees of

freedom in the fit (determined by the number of wavelength points considered in the fitting, $\nu = 1060$) implies a difference in reduced χ^2 , $\delta\chi_r^2 \approx 0.0198$ for $\Delta\sigma = 1$. Thus, based on the variation in χ_r^2 with $\langle \log[{\rm Age/yr}] \rangle$, the difference in ages of the two composites with the largest difference in $\langle W_\lambda({\rm Ly}\alpha) \rangle$ (corresponding to subsamples WT1LN and WT3) is significant at the $\simeq 2\sigma$ level.

For comparison, the distributions of SED-inferred $\log[{\rm Age/yr}]$ (Section 2.3.3) and $W_{\lambda}({\rm Ly}\alpha)$ measured for individual galaxies are shown in the bottom right panel of Figure 5. A Spearman rank correlation test indicates a marginal anticorrelation between $\log[{\rm Age/yr}]$ and $W_{\lambda}({\rm Ly}\alpha)$ for individual galaxies, with a probability of 18% that the two are uncorrelated. As noted in Section 3.1.2, the strengths of the correlations summarized in Figure 5 are similar to those obtained with the 300bin, 100sin, and 300sin models. The ionizing spectrum assumed for the next step of the fitting process (photoionization modeling; Section 3.2) was determined by the SPSneb model that best fits the composite FUV spectrum.

3.2. Photoionization Modeling and Results

3.2.1. Photoionization Modeling Procedure

The Cloudy version 17.02 radiative transfer code (Ferland et al. 2017) was used to predict the nebular continuum spectra and line intensities for the SPSneb models that best fit the composite FUV spectra, following the same procedure described in Topping et al. (2020a). The photoionization modeling also assumed a plane-parallel geometry with an electron density $n_e = 250 \text{ cm}^{-3}$, the average value inferred for MOSDEF galaxies (Sanders et al. 2016). 11 All elemental abundances were updated to the values given in Asplund et al. (2009). Additionally, we assumed log(N/O) = -1.20 based on the N2O2 and N2S2 indices computed for the composites and using the calibrations of Steidel et al. (2016) and Strom et al. (2017). For the range of O abundances inferred for the composites using lines other than [N II], log(N/O) is expected to vary by ≈ 0.14 dex according to the best-fit relation between log(N/O) and 12 + log(O/H) provided in Pilyugin et al. (2012). Regardless, the best-fit $\langle Z_{neb} \rangle$ does not change significantly if log(N/O) is allowed to vary with O abundance in the photoionization modeling, or if [NII] is excluded altogether from the fitting.

The nebular oxygen abundance was varied from $Z_{\rm neb}/Z_{\odot}=0.1$ to 1.0 in steps of $0.1\,Z_{\odot}$. Additionally, the intensity of the ionizing radiation field at the illuminated face of the gas slab, expressed by the ionization parameter, U, where

$$U \equiv \frac{n_{\gamma}}{n_{\rm H}},\tag{2}$$

 $[\]overline{^{11}}$ For the subsample containing all galaxies with coverage of the optical nebular emission lines (subsample ALN), $\langle n_e \rangle = 288 \pm 58 \text{ cm}^{-3}$ based on the ratio of the two lines of the [O II] doublet, consistent with the $n_e = 250 \text{ cm}^{-3}$ assumed for the photoionization modeling.

¹² The Pilyugin et al. (2012) relation between $\log(N/O)$ and electron-temperature-based (T_e -based) 12 + $\log(O/H)$ was shifted by \simeq 0.24 dex toward higher 12 + $\log(O/H)$ to account for the tendency of the latter to underestimate O abundances obtained from photoionization modeling (e.g., Esteban et al. 2014; Blanc et al. 2015; Steidel et al. 2016) and to ensure that the relation simultaneously passes through the solar values of $\log(N/O)$ and $\log(O/H)$.

10

Table 2 SPSneb and ISM Model Fit Results

| Subsample | $\langle E(B-V)_{\rm cont}\rangle^{\rm a}$ | $\left\langle Z_{*}/Z_{\odot}\right angle ^{b}$ | $\left\langle log \left[\frac{Age}{yr} \right] \right\rangle^c$ | $\langle E(B-V)_{\rm neb}\rangle^{\rm d}$ | $\langle Z_{\rm neb}/Z_{\odot} angle^{ m e}$ | $\langle \log U angle^{ m f}$ | $\langle E(B-V)_{\rm los}\rangle^{\rm g}$ | $\langle f_{\rm cov}({\rm H~I}) \rangle^{ m h}$ | $\left\langle \log \left[\frac{N(H I)}{cm^{-2}} \right] \right\rangle^{i}$ | $\langle W_{\lambda}^{\rm em}({\rm Ly}\alpha)\rangle \ (\mathring{\rm A})^{\rm j}$ | $\langle f_{\rm esc}^{\rm spec} ({\rm Ly}\alpha) \rangle^{\bf k}$ |
|---------------|--|---|--|---|---|--------------------------------|---|---|---|--|---|
| A | 0.099 ± 0.005 | 0.076 ± 0.018 | 8.0 ± 0.2 | | | | | | | | _ |
| AL | 0.099 ± 0.005 | 0.075 ± 0.017 | 8.1 ± 0.2 | | | | 0.096 ± 0.013 | 0.97 ± 0.02 | 20.7 ± 0.2 | 9.11 ± 1.67 | |
| ALN | 0.101 ± 0.006 | 0.082 ± 0.017 | 8.2 ± 0.3 | 0.33 ± 0.04 | 0.38 ± 0.09 | -2.93 ± 0.05 | 0.089 ± 0.012 | 0.99 ± 0.01 | 20.7 ± 0.2 | 8.65 ± 1.36 | 0.014 ± 0.003 |
| WT1 | 0.116 ± 0.009 | 0.082 ± 0.019 | 8.5 ± 0.2 | | | | | | | | |
| WT1L | 0.113 ± 0.011 | 0.097 ± 0.019 | 8.4 ± 0.3 | | | | 0.104 ± 0.010 | 0.98 ± 0.02 | 21.0 ± 0.2 | 0.00 ± 0.89 | |
| WT1LN | 0.115 ± 0.011 | 0.080 ± 0.021 | 8.4 ± 0.3 | 0.29 ± 0.07 | 0.37 ± 0.11 | -3.01 ± 0.07 | 0.102 ± 0.015 | 0.99 ± 0.02 | 21.1 ± 0.2 | 0.00 ± 0.97 | 0.001 ± 0.002 |
| WT2 | 0.095 ± 0.007 | 0.126 ± 0.022 | 8.2 ± 0.2 | | | | | | | | |
| WT2L | 0.093 ± 0.007 | 0.119 ± 0.023 | 8.3 ± 0.2 | | | | 0.100 ± 0.012 | 0.96 ± 0.02 | 20.0 ± 0.7 | 5.78 ± 1.69 | |
| WT2LN | 0.099 ± 0.011 | 0.123 ± 0.032 | 8.3 ± 0.2 | 0.48 ± 0.11 | 0.41 ± 0.04 | -3.15 ± 0.08 | 0.096 ± 0.014 | 0.97 ± 0.03 | 20.7 ± 0.2 | 4.89 ± 1.37 | 0.006 ± 0.003 |
| WT3 | 0.073 ± 0.007 | 0.079 ± 0.015 | 7.7 ± 0.2 | | | | | | | | |
| WT3L | 0.078 ± 0.009 | 0.078 ± 0.017 | 7.7 ± 0.2 | | | | 0.093 ± 0.017 | 0.90 ± 0.03 | 20.2 ± 0.4 | 22.50 ± 2.64 | 0.035 ± 0.009 |
| WT3LN | 0.091 ± 0.010 | 0.087 ± 0.033 | 7.8 ± 0.2 | 0.33 ± 0.07 | 0.44 ± 0.08 | -2.74 ± 0.07 | 0.093 ± 0.017 | 0.90 ± 0.03 | 19.7 ± 0.5 | 17.99 ± 3.06 | 0.031 ± 0.006 |
| ST1 | 0.100 ± 0.010 | 0.115 ± 0.042 | 8.2 ± 0.2 | | | | | | | | |
| ST1L | 0.095 ± 0.009 | 0.091 ± 0.032 | 8.2 ± 0.2 | 0.24 ± 0.13 | 0.28 ± 0.13 | -3.06 ± 0.07 | 0.100 ± 0.022 | 0.95 ± 0.03 | 20.8 ± 0.3 | 5.49 ± 1.98 | 0.015 ± 0.005 |
| ST2 | 0.113 ± 0.011 | 0.117 ± 0.034 | 8.1 ± 0.3 | | | | | | | | |
| ST2L | 0.122 ± 0.012 | 0.146 ± 0.059 | 8.2 ± 0.3 | 0.45 ± 0.07 | 0.40 ± 0.03 | -3.10 ± 0.06 | 0.117 ± 0.006 | 0.98 ± 0.01 | 20.3 ± 0.7 | 6.36 ± 2.45 | 0.007 ± 0.003 |
| ST3 | 0.083 ± 0.007 | 0.111 ± 0.020 | 7.8 ± 0.2 | | | | | | | | |
| ST3L | 0.085 ± 0.007 0.086 ± 0.009 | 0.111 ± 0.020 0.118 ± 0.028 | 8.0 ± 0.2 | 0.38 ± 0.07 | 0.43 ± 0.08 | -2.70 ± 0.07 | 0.082 ± 0.017 | 0.92 ± 0.02 | 20.8 ± 0.2 | 10.55 ± 3.62 | 0.013 ± 0.003 |
| sST1 | 0.127 ± 0.012 | 0.079 ± 0.022 | 7.9 ± 0.2 | | | | | | | | - |
| sST1L | 0.123 ± 0.011 | 0.063 ± 0.014 | 7.8 ± 0.3 | 0.39 ± 0.08 | 0.34 ± 0.14 | -3.16 ± 0.07 | 0.122 ± 0.005 | 0.99 ± 0.02 | 20.4 ± 0.2 | 6.28 ± 2.43 | 0.009 ± 0.003 |
| sST2 | 0.095 ± 0.010 | 0.163 ± 0.052 | 8.4 ± 0.3 | | | | | | | | |
| sST2L | 0.099 ± 0.010 0.099 ± 0.012 | 0.163 ± 0.052 0.167 ± 0.055 | 8.4 ± 0.3 8.4 ± 0.3 | 0.38 ± 0.08 | 0.40 ± 0.02 | -2.95 ± 0.07 | 0.101 ± 0.008 | 0.95 ± 0.02 | 20.9 ± 0.2 | 5.17 ± 2.34 | 0.007 ± 0.003 |
| -CT2 | 0.076 0.006 | 0.100 0.010 | 9.1 + 0.2 | | | | | | | | |
| sST3 sST3L | 0.076 ± 0.006 0.080 ± 0.007 | 0.108 ± 0.018 0.115 ± 0.014 | 8.1 ± 0.2 8.1 ± 0.2 | 0.30 ± 0.06 | 0.41 ± 0.08 | -2.70 ± 0.04 | 0.067 ± 0.005 | 0.91 ± 0.02 | 20.4 ± 0.3 | 11.30 ± 3.90 | 0.020 ± 0.003 |
| 55151 | 3.000 ± 0.007 | 5.11 <i>5</i> ± 5.514 | 0.1 ± 0.2 | 3.30 ± 0.00 | 3.11 ± 0.00 | 2.70 ± 0.04 | 5.007 ± 6.005 | 0.71 ± 0.02 | 20.1 ± 0.5 | 11.50 ± 5.50 | 5.020 ± 5.005 |

Notes.

^a Continuum reddening assuming the SMC extinction curve (Gordon et al. 2003).

^b Stellar metallicity in solar units, assuming $Z_{\odot} = 0.0142$ (Asplund et al. 2009).

c Age.

^d Nebular reddening assuming the Cardelli et al. (1989) extinction curve.

^e Nebular oxygen abundance in solar units.

f Ionization parameter.

Eline-of-sight reddening of the gas covering the continuum in the clumpy ISM model, assuming the SMC extinction curve.

He I covering fraction in the clumpy ISM model.

He I column density in the clumpy ISM model.

^j Ly α emission-line equivalent width.

k Line-of-sight escape fraction of Ly α photons.

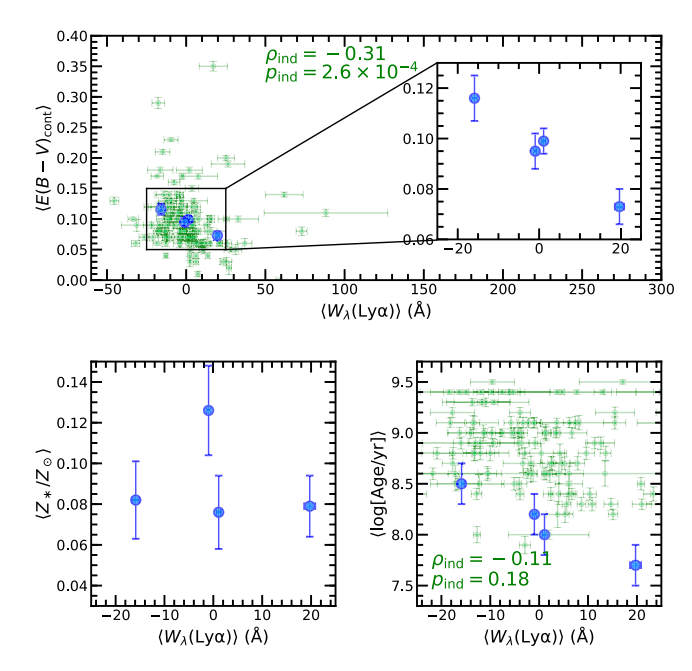


Figure 5. Variation of $\langle E(B-V)_{\rm cont} \rangle$ (top), $\langle Z_*/Z_{\odot} \rangle$ (bottom left), and $\langle \log[{\rm Age/yr}] \rangle$ (bottom right) assuming the 100bin models, with $\langle W_{\lambda}({\rm Ly}\alpha) \rangle$ for the A, WT1, WT2, and WT3 subsamples. The $E(B-V)_{\rm cont}$ and $\log[{\rm Age/yr}]$ (obtained from SED fitting; Section 2.3.3) for individual galaxies are denoted by the light-green points in the top and bottom right panels, respectively. Also indicated are the Spearman ρ correlation coefficient ($\rho_{\rm ind}$) and p-value ($p_{\rm ind}$) between $E(B-V)_{\rm cont}$ and $W_{\lambda}({\rm Ly}\alpha)$ and between $\log[{\rm Age/yr}]$ and $W_{\lambda}({\rm Ly}\alpha)$, for individual galaxies. The inset panel on the top zooms in on the $\langle E(B-V)_{\rm cont} \rangle$ and $\langle W_{\lambda}({\rm Ly}\alpha) \rangle$ measurements obtained from the composite FUV spectra.

was varied from $\log U = -3.5$ to $\log U = -1.6$ in steps of 0.1 dex. Here U is the ratio of the number densities of hydrogen-ionizing photons and hydrogen atoms, where $n_{\rm H} \approx n_e$.

Each photoionization model predicts the intrinsic ratio of H α to H β , which, in concert with the Cardelli et al. (1989) extinction curve, was used to calculate the nebular reddening, $E(B-V)_{\text{neb}}$ (e.g., Reddy et al. 2015), and dust-correct all the nebular emission lines. 13 The dust-corrected nebular emissionline intensities relative to dust-corrected H β for all the subsamples with complete coverage of the optical nebular emission lines are listed in Table 3. The optical nebular emission-line ratios predicted by each photoionization model were then compared to the dust-corrected emission-line ratios measured from the composite optical spectra to deduce the best-fit combinations of $Z_{\rm neb}$ and $\log U$. ¹⁴ Table 4 lists a few of the line diagnostics discussed below and their definitions. In identifying the best-fit photoionization model, we considered all of the following lines: [O II] $\lambda\lambda3727$, 3730, [Ne III] $\lambda3870$, $H\beta$, [O III] $\lambda\lambda4960$, 5008, $H\alpha$, [N II] $\lambda6585$, and [S II] $\lambda\lambda6718$, 6733. The photoionization modeling constraints on Z_{neb} , log U, and the BPASS model type are discussed below in Sections 3.2.2, 3.2.3, and 3.2.4, respectively.

3.2.2. Modeling Constraints on Oxygen Abundance

A few of the key line ratios used to constrain Z_{neb} are depicted in Figure 6, including the O32 versus R23 diagnostic plane—which provides a clean separation between models of different Z_{neb} (e.g., McGaugh 1991; Kobulnicky et al. 1999; Kewley & Dopita 2002)—and the N2 and S2 BPT planes (Baldwin et al. 1981). In these diagrams, each colored curve represents the sequence of $\log U$ at a fixed Z_{neb} for a given BPASS model type. The widths of the curves indicate the range of line ratios expected given the range of $\langle Z_* \rangle$ and $\langle \log[\text{Age/yr}] \rangle$ inferred from modeling the composite FUV spectra (Section 3.1). Specifically, the upper and lower edges of each curve indicate the model expectations for the ionizing spectrum of a stellar population with $Z_* = 0.0010$ and log[Age/yr] = 7.8 and with $Z_* = 0.0018$ and log[Age/yr] = 8.5, respectively, covering roughly the range of Z_* and ages found in Section 3.1. The differences in the ionizing spectra of the best-fit SPSneb models are discussed further in Section 4.2, but for the moment we note that these variations in the ionizing spectrum do little to alter the nebular line ratios predicted from the photoionization modeling (see also Runco et al. 2021).

Figure 6 clearly demonstrates the preference for oxygen abundances of $\langle Z_{\text{neb}} \rangle \simeq 0.4$ Z_{\odot} ($\langle 12 + \log(\text{O/H}) \rangle \simeq 8.29$) averaged across the ALN and WT subsamples with complete coverage of the optical nebular emission lines. The $\langle Z_{\text{neb}} \rangle$ obtained from the photoionization modeling vary in the range $\langle Z_{neb} \rangle \simeq \! 0.3 - 0.5~\bar{Z}_{\odot}$ (see also Topping et al. 2020a; Runco et al. 2021). As noted earlier, we adopted log(N/O) = -1.20based on the N2O2 and N2S2 indices. This choice yields N2 that are consistent with the predictions of the photoionization model (with $Z_{\rm neb} \approx 0.4 \ Z_{\odot}$) that reproduces all of the other line ratios under consideration. The inferred $\langle Z_{\text{neb}} \rangle$ are similar between the different BPASS model types given the typical uncertainties in the nebular line ratios. Photoionization models with Z_{neb} comparable to the *stellar* metallicities obtained from fitting the composite FUV spectra ($\langle Z_* \rangle \simeq 0.001$; Section 3.1) are ruled out at the $3\sigma-4\sigma$ level, depending on the subsample (see also Steidel et al. 2016). Appendix B discusses the O abundances derived from the "direct" metallicity method: these direct-method abundances agree with those obtained from the photoionization modeling.

3.2.3. Modeling Constraints on Ionization Parameter

The line diagnostic diagrams in Figure 6, in addition to Ne3O2 versus O32 (e.g., Nagao et al. 2006; Pérez-Montero et al.2007; Levesque & Richardson 2014; Steidel et al. 2016; Strom et al. 2017; Jeong et al. 2020), may be used to constrain the ionization parameter, U. These diagrams are presented in Figure 7, zoomed in on the regions of line diagnostic space that encompass the measurements for the ALN and WT subsamples with complete coverage of the optical nebular emission lines. For simplicity, we only show the expected line ratios for a 100bin stellar population with $Z_* = 0.0012$, $\log[Age/yr] = 8.0$, and $Z_{neb} = 0.4$ Z_{\odot} (thick black curve), where the points indicate the labeled values of $\log U$. The photoionization modeling points to best-fit values of $\langle \log U \rangle \simeq -3.1$ to -2.8. As per the discussion in Section 3.2.2 and Figure 6, the best-fit values of $\langle \log U \rangle$ are insensitive to the BPASS model type and the range of ionizing spectra corresponding to the best-fit SPSneb models.

 $[\]overline{^{13}}$ Reddy et al. (2020) find that the Galactic extinction curve (Cardelli et al. 1989) provides an adequate description of the nebular reddening curve at optical wavelengths for $z\sim2$ galaxies in the MOSDEF survey.

 $^{^{1\}dot{4}}$ The best-fit photoionization models predict an intrinsic H α -to-H β ratio of $({\rm H}\alpha/{\rm H}\beta)_{\rm int}=2.79$ (independent of the BPASS model type used for fitting), slightly lower than the canonical value of $({\rm H}\alpha/{\rm H}\beta)_{\rm int}=2.86$ for Case B recombination and $T_e=10,000$ K (Osterbrock & Ferland 2006).

Table 3
Optical Nebular Emission-line Measurements

| Subsample | $\langle L(H\beta) \rangle^{a}$ | $\langle I(O II) \rangle^{b}$ | $\langle I(\text{Ne III})\rangle^{c}$ | $\langle I(O \text{ III } \lambda 4960) \rangle^{\mathbf{d}}$ | $\langle I(O \text{ III } \lambda 5008) \rangle^{e}$ | $\langle I(H\alpha)\rangle^{f}$ | $\langle I(N II)\rangle^{g}$ | $\langle I(S II)\rangle^{h}$ |
|---|--|---|---|---|---|---|---|---|
| ALN | 277 ± 41 | 3.18 ± 0.37 | 0.29 ± 0.08 | 1.17 ± 0.10 | 3.56 ± 0.25 | 2.79 ± 0.01 | 0.35 ± 0.04 | 0.55 ± 0.06 |
| WT1LN WT2LN WT3LN | 287 ± 119 368 ± 128 314 ± 65 | 3.77 ± 1.03 4.59 ± 1.01 3.03 ± 0.54 | $\begin{array}{c} 0.29 \pm 0.21 \\ 0.03 \pm 0.21 \\ 0.41 \pm 0.16 \end{array}$ | $\begin{aligned} 1.02 &\pm 0.25 \\ 1.07 &\pm 0.21 \\ 1.37 &\pm 0.19 \end{aligned}$ | $\begin{array}{c} 3.57 \pm 0.65 \\ 2.66 \pm 0.42 \\ 4.50 \pm 0.51 \end{array}$ | $\begin{array}{c} 2.79 \pm 0.01 \\ 2.79 \pm 0.01 \\ 2.79 \pm 0.01 \end{array}$ | 0.33 ± 0.05 0.48 ± 0.07 0.29 ± 0.05 | 0.49 ± 0.11 0.67 ± 0.13 0.44 ± 0.07 |
| ST1 ST1L ST2 ST2L ST3L ST3L | 158 ± 47 160 ± 56 400 ± 97 426 ± 98 491 ± 137 511 ± 173 | $\begin{array}{c} 3.43 \pm 0.83 \\ 3.41 \pm 0.91 \\ 4.44 \pm 0.93 \\ 4.74 \pm 0.88 \\ 2.91 \pm 0.45 \\ 2.94 \pm 0.45 \end{array}$ | $\begin{array}{c} 0.31 \pm 0.28 \\ 0.25 \pm 0.29 \\ 0.28 \pm 0.24 \\ 0.30 \pm 0.25 \\ 0.41 \pm 0.10 \\ 0.41 \pm 0.11 \end{array}$ | 0.94 ± 0.21 1.00 ± 0.27 0.87 ± 0.19 0.80 ± 0.18 1.53 ± 0.17 1.48 ± 0.17 | 2.64 ± 0.49 2.64 ± 0.59 3.04 ± 0.47 3.00 ± 0.51 4.76 ± 0.41 4.65 ± 0.43 | 2.80 ± 0.01 2.80 ± 0.01 2.79 ± 0.01 2.79 ± 0.01 2.79 ± 0.01 2.79 ± 0.01 | $\begin{array}{c} 0.46 \pm 0.08 \\ 0.42 \pm 0.07 \\ 0.42 \pm 0.06 \\ 0.44 \pm 0.06 \\ 0.28 \pm 0.05 \\ 0.28 \pm 0.05 \end{array}$ | $\begin{array}{c} 0.56 \pm 0.14 \\ 0.54 \pm 0.13 \\ 0.58 \pm 0.08 \\ 0.60 \pm 0.09 \\ 0.39 \pm 0.05 \\ 0.39 \pm 0.05 \end{array}$ |
| sST1 sST1L sST2 sST2L sST3 sST3L | 269 ± 96 303 ± 104 415 ± 136 400 ± 117 298 ± 74 323 ± 90 | $\begin{array}{c} 3.83 \pm 0.92 \\ 4.28 \pm 1.16 \\ 4.12 \pm 0.78 \\ 3.95 \pm 0.64 \\ 2.41 \pm 0.42 \\ 2.57 \pm 0.51 \end{array}$ | $\begin{array}{c} 0.23 \pm 0.19 \\ 0.19 \pm 0.31 \\ 0.49 \pm 0.21 \\ 0.49 \pm 0.20 \\ 0.33 \pm 0.11 \\ 0.38 \pm 0.11 \end{array}$ | 0.69 ± 0.17 0.72 ± 0.20 1.15 ± 0.21 1.10 ± 0.20 1.58 ± 0.17 1.52 ± 0.16 | 2.30 ± 0.31 2.52 ± 0.50 3.60 ± 0.60 3.63 ± 0.63 4.88 ± 0.39 4.68 ± 0.45 | 2.80 ± 0.01 2.79 ± 0.01 | $\begin{array}{c} 0.53 \pm 0.05 \\ 0.51 \pm 0.05 \\ 0.36 \pm 0.06 \\ 0.37 \pm 0.06 \\ 0.23 \pm 0.04 \\ 0.25 \pm 0.05 \end{array}$ | $\begin{array}{c} 0.61 \pm 0.09 \\ 0.62 \pm 0.10 \\ 0.50 \pm 0.10 \\ 0.49 \pm 0.10 \\ 0.37 \pm 0.07 \\ 0.39 \pm 0.08 \end{array}$ |

Notes

Table 4
Line Diagnostics

| Line | |
|------------|--|
| Diagnostic | Definition |
| O3 | $\log(\text{[O III]} \lambda 5008/\text{H}\beta)$ |
| O32 | $\log(\text{[O III]} \lambda\lambda 4960 + 5008/\text{[O II]} \lambda\lambda 3727 + 3730)$ |
| N2 | $\log(\text{[N II]}\lambda6585/\text{H}\alpha)$ |
| S2 | $\log([S II] \lambda \lambda 6718 + 6733/H\alpha)$ |
| N2O2 | $\log([\text{N II}] \lambda 6585/[\text{O II}] \lambda \lambda 3727 + 3730)$ |
| N2S2 | $\log([\text{N II}] \lambda 6585/[\text{S II}] \lambda \lambda 6718 + 6733)$ |
| Ne3O2 | $\log(\text{[Ne III]} \lambda 3870/\text{[O II]} \lambda \lambda 3727 + 3730)$ |
| R23 | $\log((\text{[O III]}\lambda\lambda4960 + 5008 + \text{[O II]}\lambda\lambda3727 + 3730)/\text{H}\beta)$ |
| C3O3 | $\log(\text{C III}] \lambda \lambda 1907 + \lambda 1909/\text{O III}] \lambda \lambda 1661 + 1666)$ |

3.2.4. Constraints on the BPASS Model Type (or Binarity)

The ratio of nebular He II $\lambda 1640$ to H β is one of the most sensitive discriminators of the BPASS model type (Steidel et al. 2016). In single-star models, He II emission arises from the stellar winds of very high mass and short-lived Wolf-Rayet stars (e.g., Shirazi & Brinchmann 2012; Crowther et al. 2016). On the other hand, the higher effective temperatures of massive binaries, their harder ionizing spectra, and the increased main-sequence lifetimes of such stars result in significant production of He II-ionizing photons for a longer duration compared to single-star models (Eldridge et al. 2017). In the context of a continuous SFH, binary stellar evolution results in significant stellar He II emission, while this emission is absent in the single-star models for ages comparable to those that best fit the composite FUV spectra, as shown in Figure 8. As alluded to in

Section 1, the (nonionizing) FUV spectrum is insufficient to discriminate between single- and binary-star population synthesis models. On the other hand, binarity results in both a harder and more intense ionizing (EUV) spectrum whose signature can be probed with FUV and optical nebular emission-line ratios (e.g., Steidel et al. 2014, 2016; Schaerer et al. 2019; Nanayakkara et al. 2019; Chisholm et al. 2019). Along these lines, the BPASS model type (i.e., single- vs. binary-star evolution) can be evaluated by comparing the inferred nebular He II luminosity with that predicted by the best-fit photoionization model.

Following Steidel et al. (2016), we measured the residual He II luminosity from the composite FUV spectrum after subtracting the best-fit SPSneb model. Because the SPSneb model includes stellar He II emission, the residual He II luminosity is assumed to be nebular in nature. The inferred nebular He II luminosity was corrected for dust obscuration assuming $\langle E(B-V)_{\text{neb}} \rangle$ and the Cardelli et al. (1989) extinction curve. These residual values are listed in Table 5 for the 100bin model type. Figure 9 shows the relative intensity of nebular He II to H β , compared to $\langle \text{He II}/\text{H}\beta \rangle$ predicted by the best-fit photoionization models for the ALN and WT subsamples with complete coverage of the optical nebular emission lines. The errors, reflected by the length of the bars in this figure, include measurement uncertainties (and thus uncertainties in the best-fit SPSneb model and uncertainties in the best-fit photoionization model). A majority of the subsamples have residual nebular He II emission that is formally "undetected" for the binary models, for the reasons explained below.

^a Dust-corrected H β luminosity in units of 10⁴⁰ erg s⁻¹, assuming the intrinsic H α /H β ratio of the best-fit photoionization model and the Cardelli et al. (1989) extinction curve, for the subsamples with complete coverage of the optical nebular emission lines.

^b Dust-corrected [O II] $\lambda\lambda 3727$, 3730 luminosity relative to $L(H\beta)$.

^c Dust-corrected [Ne III] $\lambda 3870$ luminosity relative to $L(H\beta)$.

^d Dust-corrected [O III] $\lambda 4960$ luminosity relative to $L({\rm H}\beta)$.

^e Dust-corrected [O III] λ 5008 luminosity relative to $L(H\beta)$.

f Dust-corrected H α luminosity relative to $L(H\beta)$.

^g Dust-corrected [N II] $\lambda 6585$ luminosity relative to $L(H\beta)$.

^h Dust-corrected [S II] $\lambda\lambda$ 6718, 6733 luminosity relative to $L(H\beta)$.

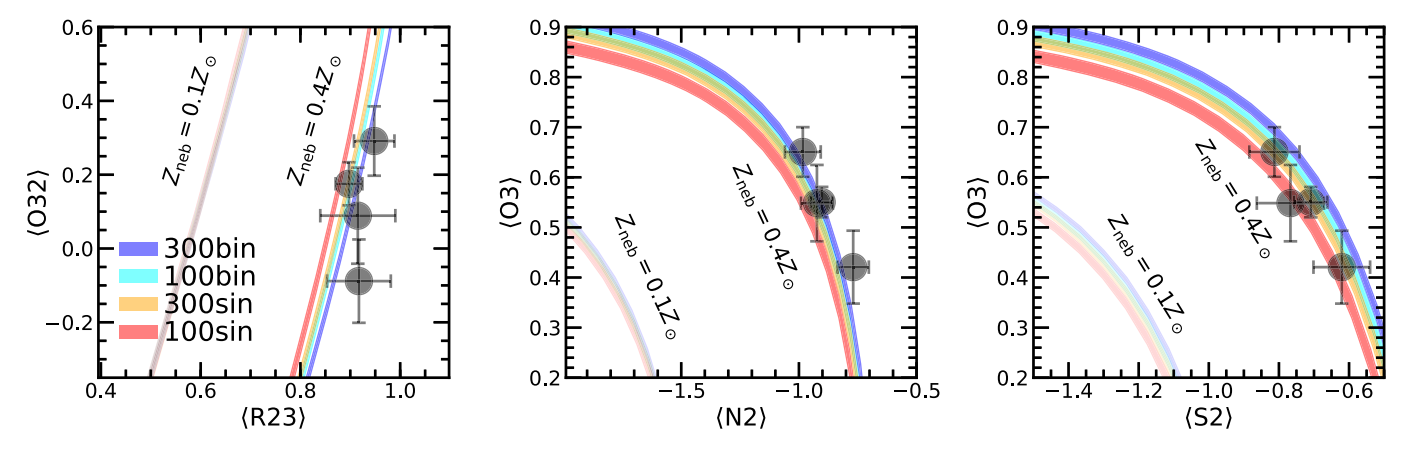


Figure 6. O32 vs. R23 (left), O3 vs. N2 (middle), and O3 vs. S2 (right) diagnostic diagrams. The dark-blue, cyan, orange, and red curves show the predicted line ratios for the 300bin, 100bin, 300sin, and 100sin BPASS model types, respectively, for $Z_{neb} = 0.4 Z_{\odot}$, while the thickness of the curves indicates the range of expected line ratios for a (1) $Z_* = 0.0010$ and $\log[{\rm Age/yr}] = 7.8$ and (2) $Z_* = 0.0018$ and $\log[{\rm Age/yr}] = 8.5$ stellar population. The set of four lighter curves are for the four BPASS model types assuming $Z_{neb} = 0.1 Z_{\odot}$. The modeling assumes $\log({\rm N/O}) = -1.20$ (Section 3.2.1). The points denote the line ratios for the ALN, WT1LN, WT2LN, and WT3LN subsamples that have complete coverage of the optical nebular emission lines.

Recall that the photoionization modeling assumes the best-fit SPSneb model as the ionizing source (Section 3.2.1). Hence, the inferred stellar He II emission and the nebular He II emission predicted by the best-fit photoionization model both assume the same SPSneb model, providing internal consistency in the way that He II is modeled. The inferred nebular He II emission is much larger in the single-star models because of the weaker inferred stellar emission, and in fact that nebular emission is significantly larger than that predicted by the best-fit photoionization models when considering the same single-star (100sin and 300sin) models. In other words, the ionizing spectra associated with single-star models are unable to account for the level of nebular He II emission inferred based on the weak stellar He II predicted by the same models.

On the other hand, the binary models yield a residual He II intensity that is comparable within the uncertainties to that predicted by the photoionization models. Based on comparing the offsets between the predicted and residual nebular He II emission from subsample to subsample, it may be tempting to conclude that the binary models also tend to underestimate the nebular He II emission. However, it is important to keep in mind that many of the subsamples have galaxies in common, and therefore the offsets observed for a given subsample are not necessarily independent of the offsets for a different subsample. When considering all galaxies in our subsample with complete coverage of the optical nebular emission lines (i.e., subsample ALN), the inferred offset between the predicted and residual nebular He II emission for the binary models is consistent with zero, while it is at least 1 dex for the single-star models.

In conclusion, we find that the binary models produce internally consistent inferences of the nebular He II emission for the composites, while the single-star models do not. Similar conclusions were reached by Steidel et al. (2016) in their analysis of the KBSS composite spectrum. Here we have shown that the binary models appear consistent with the composite spectra irrespective of $\langle W_{\lambda}(\mathrm{Ly}\alpha)\rangle$ (see Section 3.2.5 for further discussion). In the present context, the most pertinent impact of the BPASS model type is on the intrinsic production of H-ionizing photons, which is addressed in Section 4.2). As per the discussion in Sections 3.1.2, 3.2.2, and 3.2.3, the BPASS model type has little effect on the derived Z_* , $\log[\mathrm{Age/yr}]$, Z_{neb} , and $\log U$.

3.2.5. Correlations between $W_{\chi}(Ly\alpha)$ and Photoionization Model Parameters

Figure 10 summarizes the correlations between the best-fit photoionization model parameters (Table 2) and $\langle W_{\lambda}(Ly\alpha)\rangle$. For comparison, the $E(B-V)_{\rm neb}$ calculated for individual galaxies with significant (S/N \geqslant 3) detections of H α and H β are also shown in the left panel of the figure. These individual $E(B-V)_{\rm neb}$ were calculated using the same method to calculate $\langle E(B-V)_{neb} \rangle$ for the ensembles. In calculating $E(B-V)_{\text{neb}}$ for individual galaxies, we assumed $(H\alpha/H\beta)_{int} = 2.79$ based on the results of the photoionization modeling (Section 3.2.1). Over the dynamic range probed by our sample, we do not find a significant trend between $\langle E(B-V)_{\text{neb}} \rangle$ and $\langle W_{\lambda}(\text{Ly}\alpha) \rangle$. Furthermore, while the averages of individual $E(B-V)_{\text{neb}}$ measurements in bins of $W_{\lambda}(\text{Ly}\alpha)$ are consistent with the $\langle E(B-V)_{\rm neb} \rangle$ measured from the composite spectra, a Spearman correlation test indicates a high probability $(p_{\text{ind}} = 0.56)$ of a null correlation between $E(B - V)_{\text{neb}}$ and $W_{\lambda}(\text{Ly}\alpha)$ for individual galaxies (but see Scarlata et al. 2009), perhaps as a result of the larger uncertainties on the individual $E(B-V)_{\text{neb}}$ measurements.

The best-fit $\langle Z_{\rm neb} \rangle$ also do not appear to correlate strongly with $\langle W_{\lambda}({\rm Ly}\alpha) \rangle$, in the sense that galaxies with high $\langle W_{\lambda}({\rm Ly}\alpha) \rangle \gtrsim 10$ Å have $\langle Z_{\rm neb} \rangle$ consistent within the uncertainties with that of galaxies with lower $\langle W_{\lambda}({\rm Ly}\alpha) \rangle$. The ostensible lack of correlation between $\langle Z_{\rm neb} \rangle$ and $\langle W_{\lambda}({\rm Ly}\alpha) \rangle$ can be appreciated from Figures 6 and 7, where all composites irrespective of $\langle W_{\lambda}({\rm Ly}\alpha) \rangle$ have optical nebular line ratios that are generally consistent with photoionization models where $Z_{\rm neb} \approx 0.4~Z_{\odot}$.

The only significant difference found among the photoionization modeling parameters for galaxies with low and high $W_{\lambda}(\text{Ly}\alpha)$ is $\log U$. Composites formed from the lower and upper third of the $W_{\lambda}(\text{Ly}\alpha)$ distribution (i.e., WT1LN and WT3LN) indicate $\langle \log U \rangle \simeq -3.01 \pm 0.07$ and -2.74 ± 0.07 , respectively, a difference that is significant at the $\simeq 3\sigma$ level (see also Figure 7).

3.3. Neutral ISM Modeling and Results

3.3.1. Neutral ISM Modeling Procedure

The third and last step of the spectral modeling involved modifying the SPSneb models to include interstellar HI

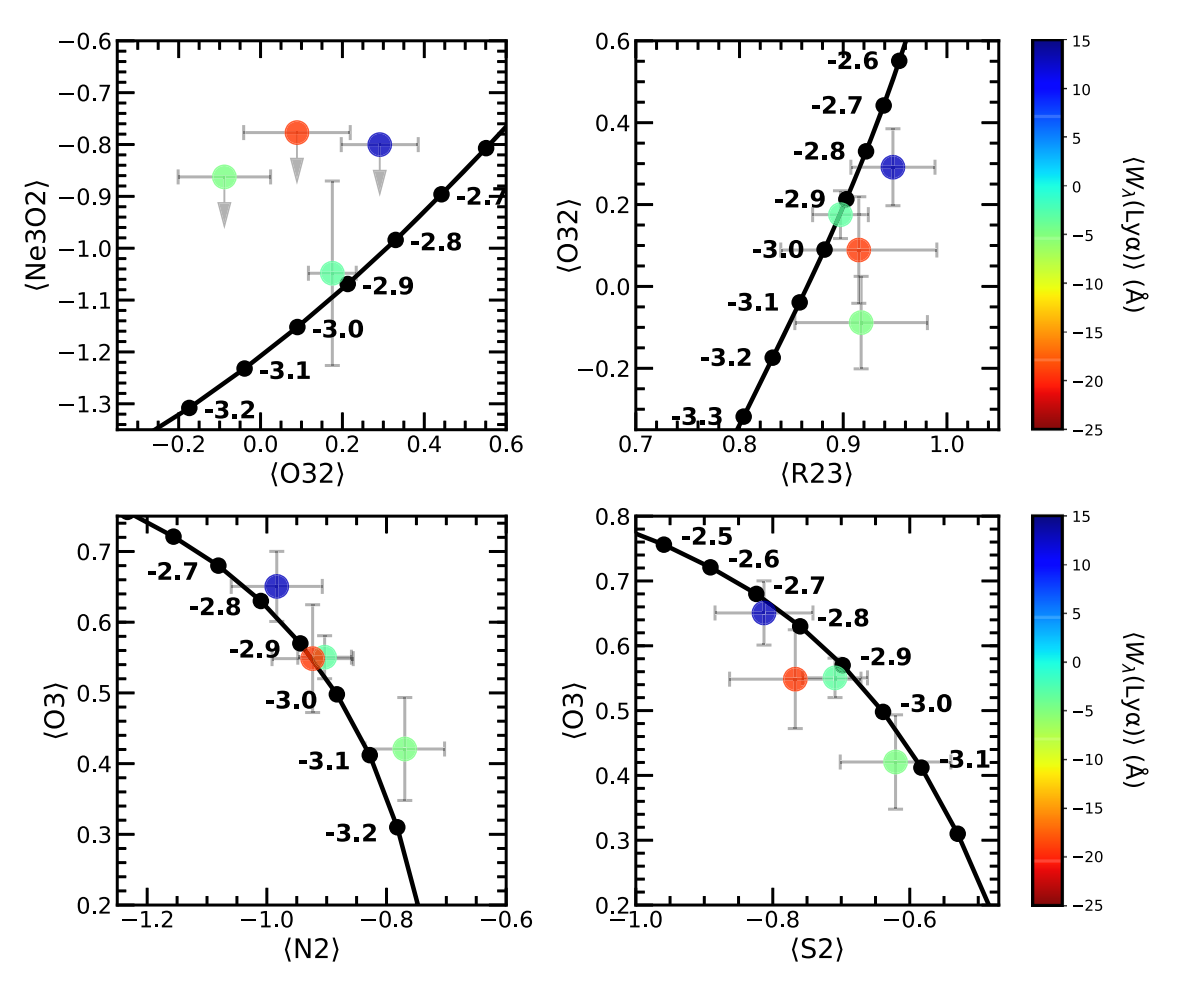


Figure 7. Ne3O2 vs. O32 (top left), O32 vs. R23 (top right), O3 vs. N2 (bottom left), and O3 vs. S2 (bottom right) diagnostic diagrams for the ALN, WT1LN, WT2LN, and WT3LN subsamples which have complete coverage of the optical nebular emission lines, where the points are color-coded according to $\langle W_{\lambda}(Ly\alpha) \rangle$. The 3 σ upper limits in Ne3O2 are shown for composites where [Ne III] was not detected with S/N > 3. The thick black curves show the expected line ratios for a 100bin stellar population with $Z_* = 0.0012$, $\log[{\rm Age/yr}] = 8.0$, and $Z_{\rm neb} = 0.4~Z_{\odot}$. The points along the curves indicate the labeled values of $\log U$.

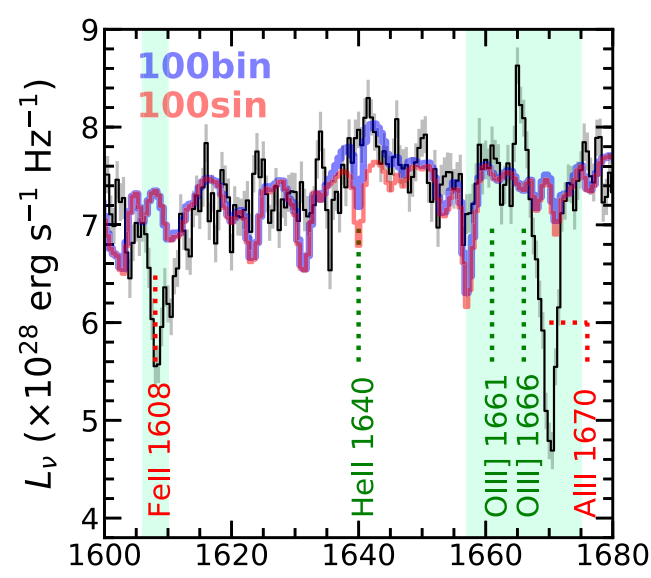


Figure 8. Comparison of the best-fit 100bin (i.e., with binaries) and 100sin (i.e., without binaries) models (blue and red, respectively) to the composite FUV spectrum of all galaxies in the sample (black), zoomed in on the region around He II λ 1640. Binary models predict significant stellar He II emission, while this emission is absent for comparably aged models that do not include binaries. Regions not included in the fitting are indicated by the light-green shaded regions.

absorption with varying column density and line-of-sight reddening. The method employed here is identical to that of Reddy et al. (2016a, 2016b) and Steidel et al. (2018), where the observed spectrum consists of two components: (a) the intrinsic spectrum and (b) the spectrum that emerges after passing through foreground H I and dust. These two components are then weighted according to the H I gas covering fraction, $f_{\rm cov}({\rm H\,I})$, to model a nonunity covering fraction of optically thick H I. This model of the neutral ISM, referred to as the "clumpy" model (also called the "holes" model in Steidel et al. 2018), can be expressed as

$$m_{\text{final}} = f_{\text{cov}}(\text{H I}) \times m_{\text{H I}} \times 10^{-0.4E(B-V)_{\text{los}}k(\lambda)} + [1 - f_{\text{cov}}(\text{H I})] \times m_0.$$
 (3)

Here m_0 is the intrinsic (unreddened) stellar spectrum determined from fitting the composite FUV spectrum with the SPSneb models (Section 3.1.1). $E(B-V)_{\rm los}$ is the line-of-sight reddening (i.e., the reddening of the covered portion of the continuum), where a range $E(B-V)_{\rm los}=0.000-0.300$ and the SMC extinction curve, $k(\lambda)$, was assumed. Lyman series absorption lines were added to the intrinsic (unreddened) stellar spectrum with a Doppler parameter of $b=125~{\rm km~s^{-1}}$ and column densities in the range $\log[N({\rm H~I})/{\rm cm^{-2}}]=18.0-23.0$. $N({\rm H~I})$ is primarily constrained by the H I

Table 5FUV Nebular Emission-line Measurements

| Subsample | $\langle I({\rm O~III})\rangle^{\rm a}$ | $\langle I(C III)\rangle^{b}$ | $\langle W_{\lambda}(\text{C III})\rangle^{c}$ | $\langle I(\text{He II})\rangle^{\mathbf{d}}$ |
|----------------|---|---|--|---|
| ALN | 0.112 ± 0.034 | 0.393 ± 0.120 | 1.330 ± 0.244 | 0.012 ± 0.029 |
| WT1LN | 0.089 ± 0.052 | 0.280 ± 0.245 | 1.032 ± 0.561 | 0.064 ± 0.195 |
| WT2LN WT3LN | $\begin{array}{c} 0.147 \pm 0.072 \\ 0.149 \pm 0.096 \end{array}$ | $\begin{array}{c} 0.847 \pm 0.531 \\ 0.478 \pm 0.201 \end{array}$ | 1.278 ± 0.554 1.790 ± 0.637 | $\begin{array}{c} 0.023 \pm 0.107 \\ 0.015 \pm 0.042 \end{array}$ |
| ST1 | 0.132 ± 0.062 | 0.286 ± 0.183 | 1.138 ± 0.509 | 0.009 ± 0.061 |
| ST1L | 0.103 ± 0.072 | 0.305 ± 0.289 | 1.053 ± 0.474 | 0.010 ± 0.058 |
| ST2 | 0.122 ± 0.085 | 0.774 ± 0.403 | 1.660 ± 0.605 | 0.022 ± 0.090 |
| ST2L | 0.102 ± 0.042 | 0.861 ± 0.372 | 1.759 ± 0.639 | 0.029 ± 0.082 |
| ST3 | 0.133 ± 0.079 | 0.459 ± 0.196 | 1.546 ± 0.503 | 0.038 ± 0.076 |
| ST3L | 0.133 ± 0.099 | 0.423 ± 0.230 | 1.349 ± 0.520 | 0.026 ± 0.061 |
| sST1 | 0.268 ± 0.101 | 0.646 ± 0.397 | 1.537 ± 0.503 | 0.035 ± 0.115 |
| sST1L | 0.121 ± 0.087 | 0.831 ± 0.587 | 1.518 ± 0.514 | 0.039 ± 0.164 |
| sST2 | 0.081 ± 0.042 | 0.357 ± 0.251 | 0.999 ± 0.548 | 0.029 ± 0.083 |
| sST2L | 0.054 ± 0.049 | 0.320 ± 0.207 | 0.966 ± 0.539 | 0.030 ± 0.075 |
| sST3 | 0.082 ± 0.070 | 0.410 ± 0.144 | 1.935 ± 0.414 | 0.020 ± 0.040 |
| sST3L | 0.112 ± 0.118 | 0.391 ± 0.183 | 1.691 ± 0.451 | 0.019 ± 0.046 |

Notes

damping wings and is therefore insensitive to the particular choice of b. Furthermore, the assumed range of $\log[N({\rm H\,I})/{\rm cm}^{-2}]$ is motivated by the results of Reddy et al. (2016b; e.g., see their Figure 2) that show that it is not possible to fit the red damping wings of the H I lines, particularly that of ${\rm Ly}\alpha$, unless $\log[N({\rm H\,I})/{\rm cm}^{-2}]\gtrsim 19$. The resulting H I-absorbed spectrum is denoted by $m_{\rm H\,I}$ in Equation (3). Accordingly, we obtained a grid of neutral ISM models with varying $E(B-V)_{\rm los}$, $\log[N({\rm H\,I})/{\rm cm}^{-2}]$, and $f_{\rm cov}({\rm H\,I})$.

The clumpy model makes the physically motivated assumption that the mechanisms that establish low column density channels in the ISM also result in negligible dust attenuation along those channels, such that only the light passing through the high column density HI is reddened by dust (but see Borthakur et al. 2014). However, because we cannot rule out the possibility of nonnegligible columns of dust in these channels, we also consider the more extreme possibility of a "screen" model where all light is attenuated by a foreground screen of dust (e.g., Steidel et al. 2018; Gazagnes et al. 2018). In this case, the ISM model can be expressed as

$$m_{\text{final}} = [f_{\text{cov}}(\text{H I}) \times m_{\text{H I}} + (1 - f_{\text{cov}}(\text{H I})) \times m_0] \times 10^{-0.4E(B-V)_{\text{cont}}k(\lambda)}.$$
 (4)

Covering fractions derived from the screen model are systematically lower than those derived from the clumpy model (see Section 3.3.2 for further discussion). Throughout the subsequent discussion, we assume by default the $f_{\rm cov}({\rm H~I})$ derived from the clumpy model, and we discuss the results from the screen model where relevant.

The best-fit values of $E(B-V)_{\rm los}$, $\log[N({\rm H~I})/{\rm cm^{-2}}]$, and $f_{\rm cov}({\rm H~I})$ are determined by the neutral ISM (clumpy) model with the minimum χ^2 relative to the composite FUV spectrum in the wavelength windows specified in Steidel et al. (2018)—slightly modified from the windows used in Reddy et al. (2016b)—where

only those windows with $\lambda_0 \gtrsim 1000\,\text{Å}$ were considered, for the following reason. While the best constraints on $f_{\rm cov}({\rm H~I})$ come from fitting multiple Lyman series absorption lines, doing so would require us to only consider galaxies for which those lines are redshifted above the atmospheric cutoff at $\lambda \simeq 3100 \,\text{A}$. All of these lines, as well as the LyC continuum region at $\lambda \simeq 900 \,\text{Å}$, can be observed from the ground at z > 2.7, a limit that excludes the bulk of our sample, which lies at lower redshifts (Figure 1). Alternatively, adopting a redshift cutoff of z > 2.12 ensures coverage of at least Ly β while still retaining sufficient numbers of galaxies in the smallest subsamples to reduce uncertainties in the foreground IGM+CGM opacity to ≤10% (Steidel et al. 2018). For this reason, the neutral ISM models are compared to the composite spectra in wavelength windows lying above $\lambda_0 \gtrsim 1000 \, \text{Å}$. Consequently, $f_{\text{cov}}(\text{H I})$ is primarily determined by the depth of $\text{Ly}\beta$, while $\log[N(\text{H I})/\text{cm}^{-2}]$ is constrained by the damping wings of Ly α and Ly β . Note that the depths of the Lyman series lines are sensitive to the HI gas covering fraction only if the lines are saturated. Below we present evidence that this is the case for galaxies in our sample.

3.3.2. Correlations between $W_{\lambda}(Ly\alpha)$ and Neutral ISM Model Parameters

The procedure described in Section 3.3.1 was used to determine the best-fit $\langle E(B-V)_{\rm los}\rangle$, $\langle \log[N({\rm H\,I})/{\rm cm^{-2}}]\rangle$, and $\langle f_{\rm cov}({\rm H\,I})\rangle$ for the AL, ALN, and WT subsamples with coverage of Ly β (Table 1). These best-fit values are listed in Table 2, and their correlations with $\langle W_{\lambda}({\rm Ly}\alpha)\rangle$ are shown in Figure 11. Figure 12 demonstrates the neutral ISM model fits to the composite FUV spectra for subsamples WT1L and WT3L. Although the gas covering fraction is primarily constrained by

^a Dust-corrected O III] $\lambda\lambda$ 1661, 1666 luminosity relative to $L(H\beta)$.

^b Dust-corrected C III] $\lambda\lambda$ 1907, 1909 luminosity relative to $L(H\beta)$.

^c Equivalent width of C III] $\lambda\lambda$ 1907, 1909.

^d Dust-corrected He II λ 1640 luminosity relative to $L(H\beta)$.

 $^{^{15}}$ Ly $\!\alpha$ absorption provides little constraint on $f_{\rm cov}({\rm H~I})$ owing to emission filling.

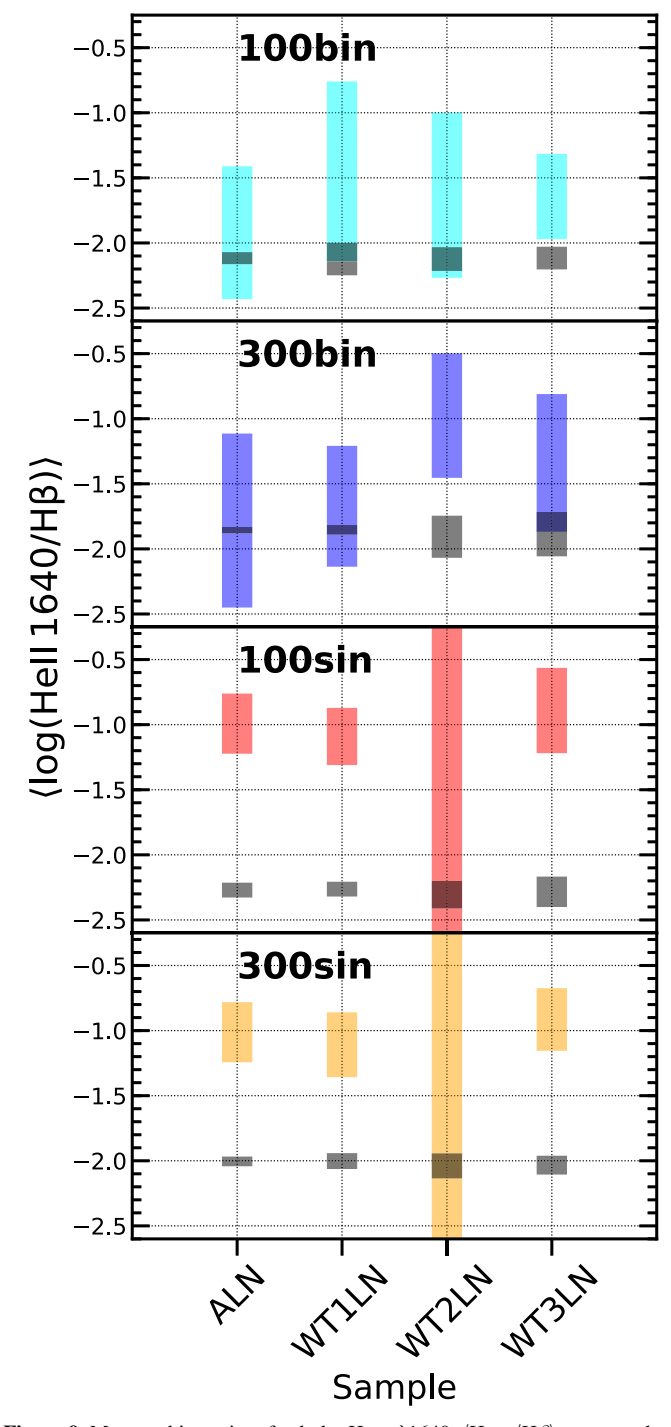


Figure 9. Measured intensity of nebular He II λ 1640, \langle He II/H β \rangle , compared to the photoionization model predictions for the ALN, WT1LN, WT2LN, and WT3LN subsamples that have complete coverage of the optical nebular emission lines. Each panel shows the comparison for a particular BPASS model type (100bin, 300bin, 100sin, 300sin). The colored bars indicate the $\pm 1\sigma$ range of the (dust-corrected) residual He II intensities obtained by subtracting the best-fit SPSneb models from the composite FUV spectra, where the errors include measurement uncertainties in the composite FUV spectra, uncertainties in the best-fit SPSneb models, and uncertainties in the best-fit $\langle E(B-V)_{\rm neb} \rangle$ (which is used for the dust correction; see text). The gray bars indicate the $\pm 1\sigma$ range of nebular He II intensities predicted by the best-fit photoionization models that assume the best-fit SPSneb models as the source of the He-ionizing photons where, for visibility, the errors have been multiplied by a factor of 5. The errors include the uncertainties in the best-fit photoionization models.

the depth of Ly β , the inferred gas covering fractions provide a good match to the depth of Ly γ , for which only the subset of galaxies with $z \gtrsim 2.3$ has coverage.

The neutral ISM model fitting indicates no significant correlation between $\langle E(B-V)_{los} \rangle$ and $\langle W_{\lambda}(Ly\alpha) \rangle$. There are marginal differences in the HI column densities for galaxies with low and high $W_{\lambda}(Ly\alpha)$ (middle panel of Figure 11), such that galaxies with high $\langle W_{\lambda}(L v \alpha) \rangle$ appear to have somewhat lower $\langle \log[N(H I)/cm^{-2}] \rangle$. However, the uncertainties in the latter are sufficiently large to prevent us from coming to any strong conclusions regarding any correlation between $\langle W_{\lambda}(Ly\alpha)\rangle$ and $\langle \log[N(\text{H I})/\text{cm}^{-2}] \rangle$. Regardless, the column densities even for composites with the highest $\langle W_{\lambda}(Ly\alpha)\rangle$ (i.e., those containing the strongest Ly α emitters) indicate gas that is optically thick in all the Lyman series lines and the Lyman continuum. Thus, the presence of significant Ly α emission spatially coincident with the stellar continuum (i.e., Ly α emission that is detected within the spectroscopic aperture) suggests that the Ly α photons must be escaping the galaxies through optically thin (i.e., ionized or low column density) channels in the ISM, or are scattered off of gas with sufficient velocity to be redshifted out of resonance and pass unimpeded through foreground HI.

Evidence for a nonunity covering fraction of optically thick gas is illustrated in the comparison of the neutral ISM model fits to subsamples WT1L and WT3L (Figure 12), consisting of galaxies in the lower and upper third of the $W_{\lambda}(Ly\alpha)$ distribution, respectively (Table 1). In the former case, there is little residual flux under the core of the Ly β line—and Ly γ for the subset of higher-redshift galaxies where this line is covered in the spectra while the damping wings of Ly α imply high column density gas. Thus, the model fit to subsample WT1L suggests a very high covering fraction of high column density HI. The neutral ISM model fit for subsample WT3L suggests somewhat lower (but still high) column densities of $log[N(H I)/cm^{-2}] = 20.2 \pm 0.4$, with significant residual flux detected under the Ly β core, and Ly γ for the subset of galaxies where this line is covered. This residual flux is a principal signature of the nonunity covering fraction of optically thick HI gas (e.g., Reddy et al. 2016b).

More generally, galaxies with $\langle W_{\lambda}(Ly\alpha)\rangle < 0 \text{ Å}$ have $\langle f_{\text{cov}}(\text{H I}) \rangle \gtrsim 0.96$, while those with $\langle W_{\lambda}(\text{Ly}\alpha) \rangle > 0 \text{ Å}$ have $\langle f_{\rm cov}({\rm H\,I})\rangle\lesssim 0.93$. This difference in $\langle f_{\rm cov}({\rm H\,I})\rangle$ is significant at the $\simeq 2.5\sigma$ level. However, the constraints on $\langle f_{cov}(H I) \rangle$ are sufficient to rule out (to $\gtrsim 3\sigma$) unity covering fraction for galaxies with high $\langle W_{\lambda}(Ly\alpha)\rangle$. A more significant anticorrelation between $\langle f_{cov}(H I) \rangle$ and $\langle W_{\lambda}(Ly\alpha) \rangle$ was found for UV-selected galaxies at $z \sim 3$ (Reddy et al. 2016b), where multiple Lyman series lines were used to constrain $\langle f_{cov}(H I) \rangle$. The right panel of Figure 11 also shows $\langle f_{cov}(HI) \rangle$ inferred from the screen model (red circles), which are for the most part systematically lower than $f_{cov}(H I)$ derived from the clumpy model but still correlate with $\langle W_{\lambda}(Ly\alpha)\rangle$. At any rate, the inference of high column density H I, Ly β that is not black at line center, and a similar level of residual flux under the Ly β and Ly γ lines suggest that the Lyman series lines are saturated and that their depths are sensitive to the covering fraction of high column density HI.

It is worth noting that for some of the composites considered in this study a screen model implies $\langle f_{\rm cov}({\rm H~I}) \rangle$ that are up to a factor of \simeq 2 × lower than the values implied by the clumpy model. Such low covering fractions imply high escape fractions

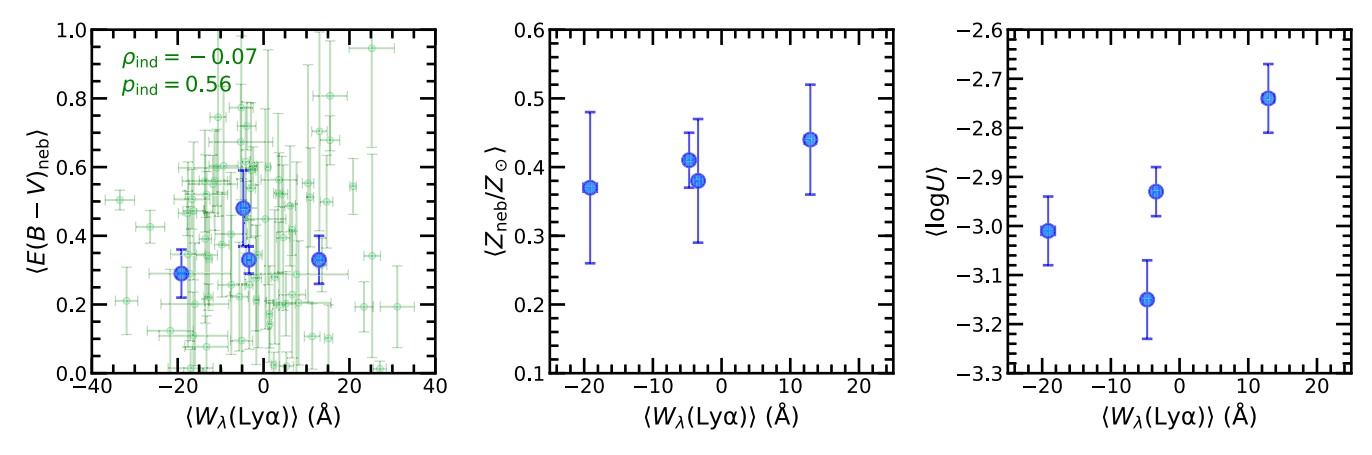


Figure 10. Variation of $\langle E(B-V)_{\rm neb} \rangle$ (left), $\langle Z_{\rm neb}/Z_{\odot} \rangle$ (middle), and $\langle \log U \rangle$ (right) assuming the 100bin models, with $\langle W_{\lambda}({\rm Ly}\alpha) \rangle$ for the ALN, WT1LN, WT2LN, and WT3LN subsamples which have complete coverage of the optical nebular emission lines. The $E(B-V)_{\rm neb}$ calculated for individual galaxies are denoted by the light-green points in the left panel. Also indicated are the Spearman ρ correlation coefficient ($\rho_{\rm ind}$) and p-value ($p_{\rm ind}$) between $E(B-V)_{\rm neb}$ and $W_{\lambda}({\rm Ly}\alpha)$ for individual galaxies.

of ionizing photons that lead to suppressed Balmer line luminosities. Accounting for the fraction of ionizing photons that escape results in H α -inferred SFRs (SFR(H α)) that exceed the UV-inferred SFRs (SFR(UV); e.g., see discussion in Section 4.3.1 and Appendix A) by up to a factor of $\simeq 2$, even when using age-dependent conversions between $H\alpha/UV$ luminosity and SFR (i.e., to account for the age of the stellar population when converting luminosity to SFR). On the other hand, $\langle f_{cov}(HI) \rangle$ inferred from the clumpy model leads to consistent H α - and UV-inferred SFRs. These results suggest that the $\langle f_{cov}(HI) \rangle$ inferred using the clumpy model are more realistic than those inferred with the screen model. Thus, the dust column densities in optically thin channels in the ISM are likely lower than what is assumed for the screen model, and closer to what is assumed in the clumpy model (i.e., negligible dust column densities).

There are a few salient points to keep in mind regarding the inferences of gas covering fractions. First, foreground contamination (Vanzella et al. 2010, 2012; Nestor et al. 2011, 2013; Mostardi et al. 2015; Siana et al. 2015) can in principle lead to residual flux under the Lyman series lines in the spectra of the targets of interest. However, as discussed in Reddy et al. (2016b), FUV spectra of the typical depth attained in this study have proven to be quite effective in identifying and removing spectroscopic blends of target and foreground galaxies, particularly when coupled to deep optical (i.e., MOSFIRE) spectra that enable the identification of lowredshift contaminants over a broader range of redshifts via a second set of (typically strong) optical nebular lines. The final sample for this work excludes galaxies for which either the MOSFIRE or LRIS spectrum indicated that there may be foreground contamination in the spectroscopic aperture (Section 2.4). The purity of these samples has been confirmed with spatially resolved deep HST observed optical and nearinfrared imaging, where foreground contaminants can be identified through photometric redshifts of galaxy subcomponents (Mostardi et al. 2015; Pahl et al. 2021).

Second, redshift uncertainties can artificially broaden and weaken the Lyman series absorption lines, resulting in a larger residual flux under the cores of the lines. Reddy et al. (2016b) used a sample of $z \sim 3$ UV-selected galaxies to show that uncertainties in the systemic redshifts—which were derived from combining absorption line and Ly α emission redshifts in

a manner similar to that discussed in Section 2.3.1—cannot explain the level of residual flux observed in composite FUV spectra, particularly for inferred $N({\rm H\,I})\gtrsim 10^{19.5}~{\rm cm}^{-2}$. Relative to the previous work of Reddy et al. (2016b), our analysis has the advantage of direct measurements of $z_{\rm sys}$ from the strong optical nebular emission lines, resulting in a factor of \simeq 2 lower uncertainties in $z_{\rm sys}$. Thus, based on the precise $z_{\rm sys}$ and the large column densities inferred from the damping wings of Ly α , the residual flux observed in the FUV composite spectra cannot be due to redshift uncertainties.

Third, there are a few reasons why the covering fraction inferred from the HI lines may be a lower limit on the true covering fraction of high column density HI. First, limited spectral resolution will mask the presence of narrow ($\Delta v \leq$ 300 km s⁻¹) absorption components that may be opaque to LyC (and Ly α) radiation but not detectable because of the lack of prominent damping wings, corresponding to column densities of $18 \lesssim \log[N(\text{H I})/\text{cm}^{-2}] \lesssim 20$. Section 4.2 argues that the presence of this moderate column density and unresolved gas is likely correlated with the covering fraction of optically thick H I. Second, if different velocity components of the HI gas are not spatially coincident, then the derived covering fraction will underestimate the true covering fraction (e.g., Vasei et al. 2016; Reddy et al. 2016b). Finally, independent of the HI column density, Ly α and LyC photons may be further attenuated if there is significant dust in the low column density channels of the ISM (e.g., Borthakur et al. 2014), as is assumed in the screen model of the ISM. Consequently, the line-of-sight escape fraction of Ly α photons may be viewed as a more direct indicator of the effective gas and dust covering fractions (Section 4.2).

3.3.3. Gas Covering Fractions from Saturated Low-ionization Interstellar Absorption Lines

As discussed in Section 1, saturated line transitions of metal ions—in particular, low-ionization interstellar absorption lines—have been widely used to infer H I covering fractions given their relative ease of detection. As noted elsewhere (Henry et al. 2015; Rivera-Thorsen et al. 2015; Reddy et al. 2016b; Vasei et al. 2016; Steidel et al. 2018; Gazagnes et al. 2018; Chisholm et al. 2018; Du et al. 2021), covering fractions derived from the low-ionization metal lines may significantly underpredict the H I covering fraction if, for example, the metal-bearing gas traces only the regions with highest gas

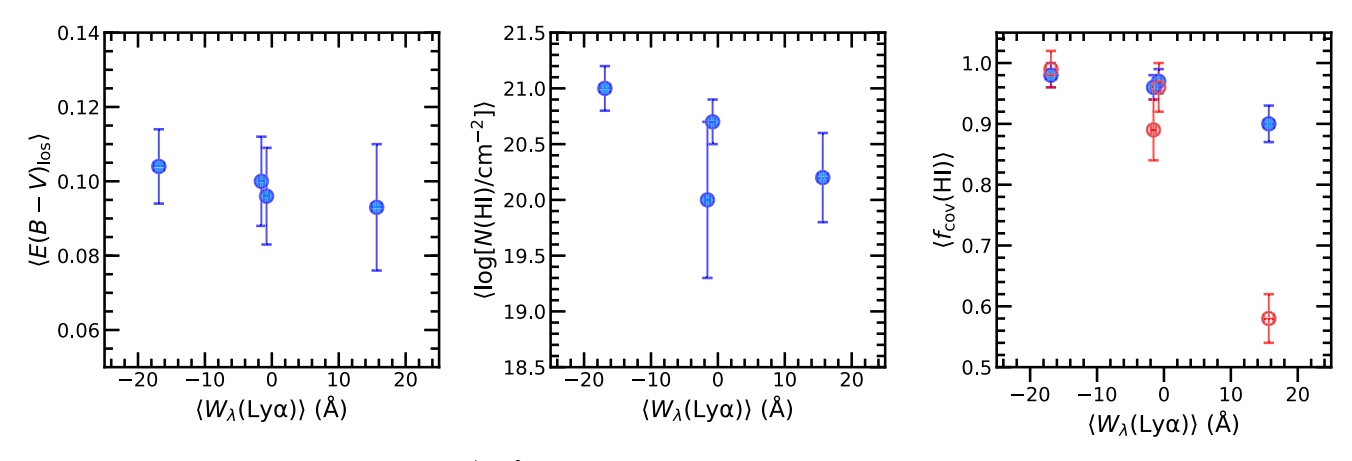


Figure 11. Variation of $\langle E(B-V)_{los} \rangle$ (left), $\langle log[N(H\,I)/cm^{-2}] \rangle$ (middle), and $\langle f_{cov}(H\,I) \rangle$ (right) assuming the 100bin models, with $\langle W_{\lambda}(Ly\alpha) \rangle$ for the AL, WT1L, WT2L, and WT3L subsamples with coverage of Ly β . The blue and red points in the right panel denote covering fractions derived in the clumpy and screen models, respectively.

densities, the H I gas is metal-poor, or partially ionized H I provides significant LyC opacity and where metal ions are primarily in the doubly ionized state. Additionally, there may be some degree of emission filling of the absorption from line photons scattered along the line of sight (e.g., Prochaska et al. 2011; Scarlata & Panagia 2015), though adjacent fine-structure transitions can mitigate this effect (e.g., Steidel et al. 2016). Nevertheless, several studies have found that covering fractions deduced from the low-ionization metal lines correlate significantly with those derived directly from the H I lines (Reddy et al. 2016b; Gazagnes et al. 2018), and thus the former could potentially be used as a proxy for the H I gas covering fraction (e.g., Gazagnes et al. 2018; Chisholm et al. 2018).

With that in mind, we explored how the depths of three saturated low-ionization metal lines in the composite FUV spectra—Si II λ 1260, Si II λ 1527, and C II λ 1334—correlate with $W_{\lambda}(\text{Ly}\alpha)$ and $f_{\text{cov}}(\text{H I})^{16}$ In the optically thin limit, the ratio of the equivalent widths of the two Si II transitions is $W_{1260}/W_{1527} \gtrsim 6$. However, the observed ratio is $W_{1260}/$ $W_{1527} \simeq 1$, indicating that the lines are saturated and their depths are sensitive to the covering fraction of Si II-enriched gas. The similarity in velocity width and depth of the lowionization transition C II $\lambda 1334$ to those of the saturated Si II transitions implies that the former arises from the same gas and that its depth is also sensitive to the covering fraction. To measure these lines, we divided the composite FUV spectra by their corresponding best-fit SPSneb models, thus allowing us to both normalize the line absorption relative to the continuum and remove any stellar absorption components (e.g., CII λ 1334). The residual fluxes, $\langle R \rangle$, at the absorption-line centers were then measured from the continuum-normalized composite FUV spectra. These values are listed in Table 6.

These residual fluxes were converted to covering fractions based on assuming the two-component model discussed in Section 3.3.1 (see also Gazagnes et al. 2018). The variations in the metal-line covering fractions, $\langle f_{\rm cov}({\rm metal}) \rangle$, with $\langle W_{\lambda}({\rm Ly}\alpha) \rangle$ and $\langle f_{\rm cov}({\rm H\,I}) \rangle$ are shown in Figure 13. These results show that galaxies with higher $\langle W_{\lambda}({\rm Ly}\alpha) \rangle$ have lower covering fractions of metal-bearing gas. The direct comparison between the metal and H I covering fractions suggests that the former is

systematically smaller than the latter (see discussion above), indicating that some portion of the optically thick H I may be metal-poor. Because of its potential utility, we provide the following empirical calibration between $\langle f_{\rm cov}({\rm metal}) \rangle$ and $\langle f_{\rm cov}({\rm H~I}) \rangle$ for the independent WTL subsamples analyzed here:

$$\langle f_{\text{cov}}(\text{metal}) \rangle = 1.50 \langle f_{\text{cov}}(\text{H I}) \rangle - 0.62,$$
 (5)

for $0.90 \lesssim \langle f_{\rm cov}({\rm H~I}) \rangle \lesssim 1.00$ (shown as a thick green line in the bottom right panel of Figure 13). We have not formally calculated errors on the slope and intercept of the relation, as the subsamples are not independent of each other. In any case, while direct inferences of $f_{\rm cov}({\rm metal})$ are useful, they do require a priori knowledge of $f_{\rm cov}({\rm H~I})$ and $E(B-V)_{\rm los}$ for the clumpy model of the ISM discussed above. For the screen model of the ISM, both $\langle f_{\rm cov}({\rm H~I}) \rangle$ and $\langle f_{\rm cov}({\rm metal}) \rangle$ are systematically lower than the corresponding values for the clumpy model, while $\langle f_{\rm cov}({\rm H~I}) \rangle$ is still systematically larger than $\langle f_{\rm cov}({\rm metal}) \rangle$. At any rate, for the same reasons given in Section 3.3.2, the limited resolution of the spectra implies that the derived $f_{\rm cov}({\rm metal})$ may be a lower limit on the true covering fraction of the metal-bearing gas.

3.4. Summary of Composite-fitting Results and Comparisons to Previous Works

We performed comprehensive modeling of composite FUV and optical spectra of galaxies in the MOSDEF-LRIS survey to deduce key properties of the massive stars (Section 3.1), ionized ISM (Section 3.2), and neutral ISM (Section 3.3) of star-forming galaxies at redshifts $1.85 \le z \le 3.49$, and we determined how these properties vary with $W_{\lambda}(\text{Ly}\alpha)$. The results of the spectral modeling are summarized below.

3.4.1. Reddening Measures

We find a significant anticorrelation between $\langle W_{\lambda}(\mathrm{Ly}\alpha) \rangle$ and $\langle E(B-V)_{\mathrm{cont}} \rangle$, similar to results from other studies (e.g., Shapley et al. 2003; Gawiser et al. 2006; Atek et al. 2008, 2009; Pentericci et al. 2009, 2010; Finkelstein et al. 2011; Guaita et al. 2011; Jones et al. 2012; Atek et al. 2014; Hathi et al. 2016; Du et al. 2018, 2021). Generally, this trend has been interpreted in a framework where $\mathrm{Ly}\alpha$ photons are preferentially attenuated (owing to their resonant scattering) compared to continuum photons, resulting in lower $W_{\lambda}(\mathrm{Ly}\alpha)$ with increasing $E(B-V)_{\mathrm{cont}}$. Alternatively, Reddy et al. (2016b) find that

 $[\]overline{^{16}}$ Du et al. (2021) present a detailed analysis of the relationships between $W_{\lambda}(\text{Ly}\alpha)$, equivalent widths of the low-ionization metal lines, and $E(B-V)_{\text{cont}}$ for MOSDEF-LRIS galaxies. Here, we just focus on using the low-ionization metal lines as proxies for the gas covering fraction.

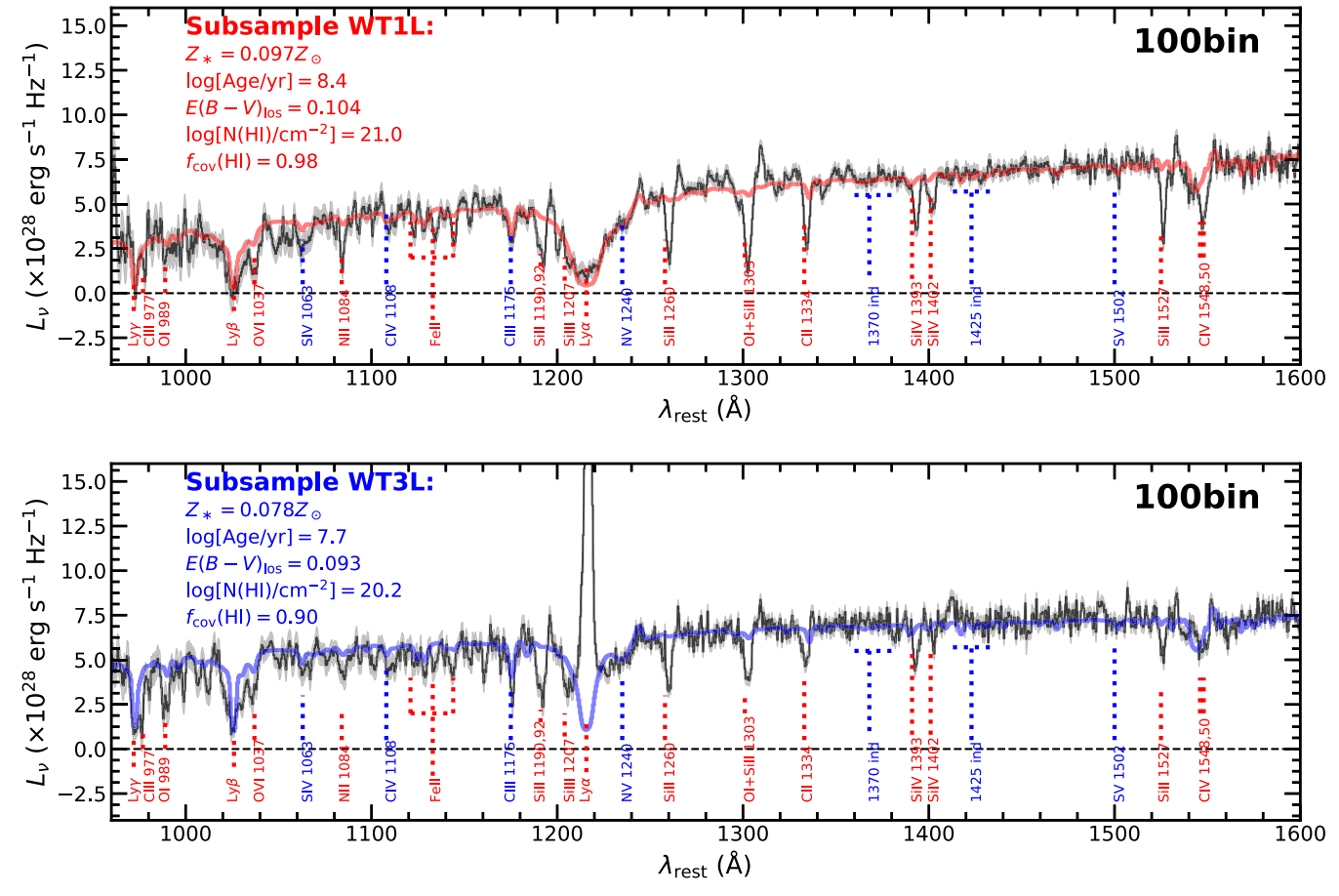


Figure 12. Composite FUV spectra for subsamples WT1L (top) and WT3L (bottom) shown in black (1σ error in gray), along with the best-fit neutral ISM model fits in red (top) and blue (bottom). These neutral ISM models assume the best-fit $\langle Z_* \rangle$ and $\langle \log[\mathrm{Age/yr}] \rangle$ obtained from the 100bin SPSneb model fitting (Section 3.1.1). Indicated in each panel are the $E(B-V)_{los}$, $\log[N(\mathrm{H~I})/\mathrm{cm^{-2}}]$, and $f_{cov}(\mathrm{H~I})$ for the models shown. Line labeling is similar to Figure 2.

 $E(B-V)_{\rm cont}$ correlates with $f_{\rm cov}({\rm H\,I})$. This correlation arises because a galaxy with higher $f_{\rm cov}({\rm H\,I})$ has a larger fraction of sight lines with nonnegligible dust content, translating to a higher $E(B-V)_{\rm cont}$; i.e., the reddening measured in the case of a foreground screen of dust, namely, $E(B-V)_{\rm cont}$, is effectively the line-of-sight reddening, $E(B-V)_{\rm los}$, weighted by the gas covering fraction. In this framework, the decrease in $W_{\lambda}({\rm Ly}\alpha)$ with increasing $E(B-V)_{\rm cont}$ may be more directly tied to the larger fraction of ${\rm Ly}\alpha$ photons scattering out of the line of sight with increasing $f_{\rm cov}({\rm H\,I})$ (see Section 4.2).

We do not find a significant correlation between $\langle W_{\lambda}(\mathrm{Ly}\alpha)\rangle$ and $\langle E(B-V)_{\mathrm{los}}\rangle$. This lack of correlation is perhaps not unexpected if the majority of $\mathrm{Ly}\alpha$ photons are escaping through low column density (and low-reddening) channels in the ISM, in which case $W_{\lambda}(\mathrm{Ly}\alpha)$ would be insensitive to the reddening of the (high column density) *covered* portion of the continuum, $E(B-V)_{\mathrm{los}}$.

Finally, $\langle E(B-V)_{\rm neb} \rangle$ does not appear to correlate significantly with $\langle W_{\lambda}({\rm Ly}\alpha) \rangle$, at least on an individual galaxy basis, with only a marginal correlation present for the composite measurements. At face value, these results run counter to those reported by Scarlata et al. (2009), who found lower ${\rm Ly}\alpha/{\rm H}\alpha$ ratios (i.e., roughly translating to lower $W_{\lambda}({\rm Ly}\alpha)$) with increasing ${\rm H}\alpha/{\rm H}\beta$, or nebular reddening (see also Trainor et al. 2016). However, this study was based exclusively on strong ${\rm Ly}\alpha$ emitters at z=0.3, and it is possible that the inclusion of similarly strong LAEs in our $z\sim 2$ sample

would reveal a trend that is otherwise difficult to discern based on the small fraction of LAEs in our sample.

For all the relevant subsamples presented here, $\langle E(B-V)_{\rm neb}\rangle > \langle E(B-V)_{\rm cont}\rangle$. Other studies report a similar offset in the reddening of the nebular emission lines relative to the stellar continuum (e.g., Fanelli et al. 1988; Calzetti et al. 1994, 2000; Förster Schreiber et al. 2009; Kashino et al. 2013; Reddy et al. 2010; Kreckel et al. 2013; Price et al. 2014; Reddy et al. 2015; Battisti et al. 2016; Theios et al. 2019; Shivaei et al. 2020; Reddy et al. 2020), though the extent of the difference depends on the attenuation curves assumed for the two (e.g., Shivaei et al. 2020; Reddy et al. 2020). As noted in many of these same studies, this difference in nebular and stellar reddening may arise from the higher column densities of dust along the sight lines to the youngest stellar populations that dominate the emission-line luminosities.

3.4.2. Ages

Subsamples with $\langle W_{\lambda}(\mathrm{Ly}\alpha) \rangle > 10\,\mathrm{\mathring{A}}$ have best-fit ages a factor of $\simeq 3-4$ younger (less than $\approx 100\,\mathrm{Myr}$) than those of subsamples with $\langle W_{\lambda}(\mathrm{Ly}\alpha) \rangle < 0\,\mathrm{\mathring{A}}$ ($\approx 300\,\mathrm{Myr}$). There is a marginal correlation between age and $W_{\lambda}(\mathrm{Ly}\alpha)$ when examined on an individual galaxy basis, such that galaxies with stronger $\mathrm{Ly}\alpha$ emission are younger. The relative youth of galaxies with strong $\mathrm{Ly}\alpha$ emission has been suggested in many previous studies (e.g., Gawiser et al. 2006; Pentericci et al. 2007; Finkelstein et al. 2007; Guaita et al. 2011; Hagen et al. 2014),

 Table 6

 Interstellar Absorption-line Measurements

| | /p/g: 140(0))3 | /p/g:) 4 505\\ h | (P(G) 100 ()) C |
|-----------|--|--|---|
| Subsample | $\langle R(\text{Si II } \lambda 1260) \rangle^{\mathbf{a}}$ | $\langle R(\text{Si II } \lambda 1527) \rangle^{\mathbf{b}}$ | $\langle R(\text{C II } \lambda 1334) \rangle^{\text{c}}$ |
| A | 0.46 ± 0.04 | 0.53 ± 0.04 | 0.52 ± 0.04 |
| AL | 0.43 ± 0.04 | 0.53 ± 0.04 | 0.51 ± 0.05 |
| ALN | 0.40 ± 0.05 | 0.48 ± 0.04 | 0.48 ± 0.04 |
| WT1 | 0.30 ± 0.07 | 0.40 ± 0.05 | 0.40 ± 0.06 |
| WT1L | 0.32 ± 0.09 | 0.38 ± 0.07 | 0.38 ± 0.07 |
| WT1LN | 0.24 ± 0.10 | 0.47 ± 0.07 | 0.31 ± 0.11 |
| WT2 | 0.43 ± 0.06 | 0.47 ± 0.06 | 0.46 ± 0.05 |
| WT2L | 0.40 ± 0.07 | 0.44 ± 0.05 | 0.45 ± 0.07 |
| WT2LN | 0.30 ± 0.07 | 0.42 ± 0.07 | 0.43 ± 0.09 |
| WT3 | 0.51 ± 0.07 | 0.64 ± 0.08 | 0.71 ± 0.05 |
| WT3L | 0.47 ± 0.07 | 0.64 ± 0.09 | 0.65 ± 0.07 |
| WT3LN | 0.52 ± 0.06 | 0.53 ± 0.06 | 0.55 ± 0.07 |
| ST1 | 0.36 ± 0.09 | 0.35 ± 0.09 | 0.45 ± 0.09 |
| ST1L | 0.35 ± 0.10 | 0.37 ± 0.09 | 0.47 ± 0.09 |
| ST2 | 0.33 ± 0.08 | 0.40 ± 0.07 | 0.49 ± 0.09 |
| ST2L | 0.29 ± 0.07 | 0.39 ± 0.06 | 0.39 ± 0.08 |
| ST3 | 0.46 ± 0.06 | 0.49 ± 0.07 | 0.48 ± 0.07 |
| ST3L | 0.43 ± 0.07 | 0.48 ± 0.07 | 0.47 ± 0.09 |
| sST1 | 0.31 ± 0.11 | 0.41 ± 0.06 | 0.47 ± 0.08 |
| sST1L | 0.33 ± 0.10 | 0.42 ± 0.06 | 0.46 ± 0.07 |
| sST2 | 0.40 ± 0.10 | 0.37 ± 0.10 | 0.39 ± 0.13 |
| sST2L | 0.35 ± 0.10 | 0.36 ± 0.09 | 0.35 ± 0.13 |
| sST3 | 0.45 ± 0.05 | 0.50 ± 0.07 | 0.53 ± 0.05 |
| sST3L | 0.41 ± 0.06 | 0.48 ± 0.07 | 0.52 ± 0.06 |

Notes.

though there appears to be a fairly large scatter in the relationship between Ly α strength and age (e.g., Pentericci et al. 2009; Finkelstein et al. 2009; Kornei et al. 2010). The implication for these age differences on the shape of the ionizing spectrum is discussed further in Section 4.2.

3.4.3. Stellar and Gas-phase Metallicities

There is no apparent significant variation of $\langle Z_* \rangle$ and $\langle Z_{\text{neb}} \rangle$ with $\langle W_{\lambda}(\mathrm{Ly}\alpha)\rangle$. The typical stellar metallicity across the subsamples is $\langle Z_*\rangle \approx 0.08~Z_{\odot}$, and the typical nebular abundance inferred from photoionization modeling is $\langle Z_{\rm neb} \rangle \approx 0.4 \ Z_{\odot}$. The direct-method T_e -based estimates from O III] $\lambda\lambda 1661$, 1666 point to $\langle Z_{\text{neb}}\rangle$ consistent with those obtained from the photoionization modeling of all the strong optical nebular emission lines (Appendix B). The lack of any significant correlation between $W_{\lambda}(Ly\alpha)$ and either the stellar or gas-phase metallicity may be related to the limited dynamic range of metallicity probed by the MOSDEF-LRIS sample. In particular, Topping et al. (2020b) find a range of $Z_{\text{neb}} \simeq$ $0.3-1.0~Z_{\odot}$ for individual objects in the MOSDEF-LRIS sample, while strong LAEs at similar redshifts $(z \sim 2 - 3)$ are found to have lower $Z_{\rm neb} \approx 0.2~Z_{\odot}$ (Trainor et al. 2016). Similarly, the broader stellar mass and $W_{\lambda}(Ly\alpha)$ ranges probed by Cullen et al. (2020) for a large spectroscopic sample of $3 \le z \le 5$ galaxies drawn from the VANDELS survey (McLure et al. 2018; Pentericci et al. 2018) allowed these authors to uncover a trend between $W_{\lambda}(Ly\alpha)$ and Z_* .

Regardless, the apparent insensitivity of $W_{\lambda}(\mathrm{Ly}\alpha)$ to Z_* for MOSDEF-LRIS galaxies strongly suggests that the observed

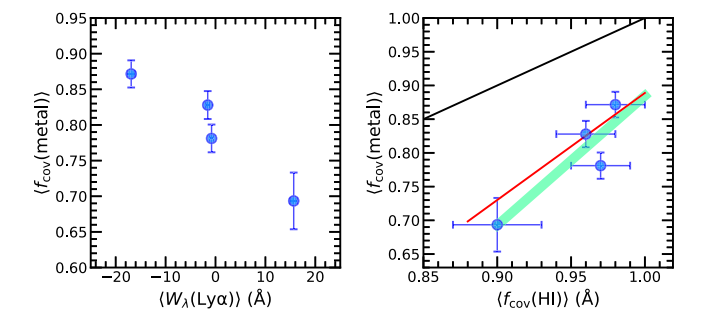


Figure 13. Inferred covering fraction of the metal-bearing gas vs. $\langle W_{\lambda}(Ly\alpha)\rangle$ (left) and $\langle f_{cov}(H\ I)\rangle$ (right) for the clumpy geometry. Measurements are shown for the AL, WT1L, WT2L, and WT3L subsamples which have coverage of Ly β . In addition, the thick green line indicates a linear fit between $\langle f_{cov}(\text{metal})\rangle$ and $\langle f_{cov}(H\ I)\rangle$ (Equation (5)). The red line indicates the best-fit linear relation between the covering fraction of Si II-enriched gas and H I for a sample of 18, mostly local, star-forming galaxies with Lyman series observations (Gazagnes et al. 2018). An equivalent gas covering fraction of the metal-bearing gas and H I is indicated by the black line.

variation in $W_{\lambda}(\mathrm{Ly}\alpha)$ within the sample may be tied to factors unrelated to the intrinsic stellar population. We revisit this issue in Section 4.2. For the time being, we note that the offset in the sample-averaged values of $\langle Z_*/Z_{\odot} \rangle \simeq 0.08$ and $\langle Z_{\mathrm{neb}}/Z_{\odot} \rangle \simeq 0.40$ implies a ratio of (O/Fe) that is roughly $5 \times$ the solar ratio, placing these galaxies at the theoretical upper limit for (O/Fe) from core-collapse (Type II) supernova (SN) enrichment (Nomoto et al. 2006). The apparent α -enhancement inferred for these galaxies is consistent with their spectrally derived stellar population ages of less than a few hundred Myr (Section 3.1.3), placing them at a stage prior to the onset of significant Fe enrichment from Type Ia SNe (see also Steidel et al. 2016; Cullen et al. 2019; Topping et al. 2020a; Matthee & Schaye 2018).

3.4.4. Ionization Parameter, log U

The ionization parameter, U, exhibits significant variation with $W_{\lambda}(\mathrm{Ly}\alpha)$: subsamples of galaxies with $\langle W_{\lambda}(\mathrm{Ly}\alpha) \rangle < 0$ Å have low average ionization parameters of $\langle \log U \rangle \lesssim -2.9$ (and as low as $\langle \log U \rangle \simeq -3.2$), while those with $\langle W_{\lambda}(\mathrm{Ly}\alpha) \rangle > 0$ Å have high average ionization parameters of $\langle \log U \rangle \gtrsim -2.8$. Additional evidence for this increase in ionization parameter with $W_{\lambda}(\mathrm{Ly}\alpha)$ comes from the correlation between the latter and C III] $\lambda\lambda 1907$, 1909, one that cannot be explained by abundance variations (Appendix C). These results concur with previous studies that have suggested high ionization parameters for LAEs relative to galaxies with weaker $\mathrm{Ly}\alpha$ emission at similar redshifts (e.g., Trainor et al. 2016). A possible physical interpretation of the trend between $\langle W_{\lambda}(\mathrm{Ly}\alpha) \rangle$ and $\langle \log U \rangle$ is discussed in Section 4.3.3.

3.4.5. Evidence of Binary Stellar Populations

SPS models that include the effects of binary stellar evolution (and with a high-mass cutoff of the IMF of 100 and $300\,M_\odot$) predict significant stellar He II $\,\lambda 1640$ emission that, when subtracted from the observed He II emission in the composite FUV spectra, yields residual (nebular) He II emission consistent with the predictions from photoionization modeling. On the other hand, SPS models that do not include the effects of binary stellar evolution, regardless of the high-mass cutoff of the IMF, lead to inferences of nebular He II emission that are significantly higher than the predictions of the photoionization models (see also

^a Residual flux at line center of Si II λ 1260 relative to the continuum.

 $^{^{\}rm b}$ Residual flux at line center of Si II $\lambda1527$ relative to the continuum.

^c Residual flux at line center of C II λ 1334 relative to the continuum.

Steidel et al. 2016). Only the SPS models that include stellar binarity can self-consistently explain the observed He II λ 1640 emission, a conclusion that applies to all of the subsamples considered in this work, irrespective of $W_{\lambda}(\text{Ly}\alpha)$.

3.4.6. Column Densities and Gas Covering Fractions

There is marginal evidence that the mean gas column density decreases with increasing $\langle W_{\lambda}(\mathrm{Ly}\alpha) \rangle$, where the former varies from $\langle \log[N(\mathrm{H\ I})/\mathrm{cm}^{-2}] \rangle \simeq 21.1$ for subsamples with the lowest $\langle W_{\lambda}(\mathrm{Ly}\alpha) \rangle$ to $\langle \log[N(\mathrm{H\ I})/\mathrm{cm}^{-2}] \rangle \simeq 19.5$ for subsamples with the highest $\langle W_{\lambda}(\mathrm{Ly}\alpha) \rangle$. In all cases, however, the best-fit $\log[N(\mathrm{H\ I})/\mathrm{cm}^{-2}]$ imply gas that is optically thick in all the Lyman series lines and the Lyman continuum. As a result, $\mathrm{Ly}\alpha$ photons spatially coincident with the stellar continuum are likely escaping through optically thin (i.e., ionized or low column density) channels in the ISM, or shifted out of resonance by gas with nonzero velocity.

For both the clumpy and screen geometries of the ISM considered above, we find that subsamples with $\langle W_{\lambda}(Ly\alpha)\rangle <$ 0 Å have mean H I covering fractions, $\langle f_{cov}(H I) \rangle$, that are close to unity, while the modeling of subsamples with $\langle W_{\lambda}(Ly\alpha)\rangle >$ 0 Å rules out unity covering fractions at the $\gtrsim 3\sigma$ level. Additional constraints on the covering fraction of metalbearing neutral H I, f_{cov} (metal), come from an examination of saturated low-ionization interstellar absorption lines. Covering fractions inferred from these lines are strongly anticorrelated with $\langle W_{\lambda}(Ly\alpha)\rangle$, where subsamples with the lowest $\langle W_{\lambda}(Ly\alpha)\rangle$ have $\langle f_{\text{cov}}(\text{metal}) \rangle \simeq 0.91$ while those with the highest $\langle W_{\lambda}(\text{Ly}\alpha)\rangle$ have $\langle f_{\text{cov}}(\text{metal})\rangle \simeq 0.78$. This strong anticorrelation between $W_{\lambda}(Ly\alpha)$ and the depths of the low-ionization interstellar absorption lines (or their equivalent widths) has been noted in a large number of previous studies (e.g., Shapley et al. 2003; Pentericci et al. 2007, 2009; Erb et al. 2010; Berry et al. 2012; Jones et al. 2012; Du et al. 2018; Marchi et al. 2019; Pahl et al. 2020; Du et al. 2021) and implies a lower covering fraction of metal-bearing gas with increasing $W_{\lambda}(Ly\alpha)$.

4. Discussion

With the modeling results of Section 3 in hand, we are in a position to evaluate the primary mechanisms responsible for the escape of Ly α photons for galaxies in our sample. The escape fraction of Ly α photons is discussed in Section 4.1. Section 4.2 focuses on the role of massive stars and the gas covering fraction on the escape of Ly α photons. The relations between gas covering fraction and the distribution of star formation and galaxy potential are discussed in Section 4.3, along with the connection between SFR surface density and ionization parameter. Section 4.4 briefly addresses the scatter between $W_{\lambda}(\text{Ly}\alpha)$ and several other parameters examined in this work. We then conclude with a discussion of the implications of our analysis for the escape of ionizing radiation at high redshift (Section 4.5).

4.1. Ly\alpha Emission Equivalent Width and Escape Fraction

The correlations presented up to this point have been cast in terms of $W_{\lambda}(\mathrm{Ly}\alpha)$, as this quantity can be easily measured for individual galaxies and ensembles of galaxies. However, as noted in Section 2.5, the connection between the production/ escape of $\mathrm{Ly}\alpha$ photons and $W_{\lambda}(\mathrm{Ly}\alpha)$ is complicated by virtue of the method used to compute $W_{\lambda}(\mathrm{Ly}\alpha)$. $W_{\lambda}(\mathrm{Ly}\alpha)$ computed

using the procedures of Kornei et al. (2010) will depend not only on the level of $Ly\alpha$ emission relative to the continuum but also on the underlying absorption. This absorption is detected in some individual galaxies (typically the brighter ones), ubiquitous in composite FUV spectra (e.g., Figures 2 and 12) and, as per the discussion of Section 3.3, due primarily to absorption from interstellar H I. Though the $net \langle W_{\lambda}(Ly\alpha) \rangle$ for a given subsample (or individual galaxy) may be negative, there may be some residual leakage of $Ly\alpha$ photons. Hence, to more directly connect the production and escape of $Ly\alpha$ photons to many of the galaxy properties discussed up to this point, we calculated two additional quantities: the emission-line $W_{\lambda}(Ly\alpha)$ as

$$W_{\lambda}^{\text{em}}(\text{Ly}\alpha) = \frac{\text{L}(\text{Ly}\alpha)_{\text{obs}}}{L_{\lambda}^{\text{red}}},$$
 (6)

and the "escape" fraction of Ly α photons as

$$f_{\rm esc}^{\rm spec}({\rm Ly}\alpha) = \frac{{\rm L}({\rm Ly}\alpha)_{\rm obs}}{L({\rm Ly}\alpha)_{\rm int}},$$
 (7)

where $L(\mathrm{Ly}\alpha)_{\mathrm{obs}}$ and $L(\mathrm{Ly}\alpha)_{\mathrm{int}}$ are the observed and intrinsic $\mathrm{Ly}\alpha$ emission luminosities, respectively, and $L_{\lambda}^{\mathrm{red}}$ is the mean luminosity density of the continuum just redward of $\mathrm{Ly}\alpha$ (see Kornei et al. 2010). Note that $f_{\mathrm{esc}}^{\mathrm{spec}}(\mathrm{Ly}\alpha)$ only refers to the fraction of $\mathrm{Ly}\alpha$ photons exiting along the sight line and does not account for photons resonantly scattered out of the spectroscopic aperture. As discussed in Steidel et al. (2011), the total escape fraction of $\mathrm{Ly}\alpha$ when summing over all sight lines will typically be $\simeq 3 \times \mathrm{larger}$ than $f_{\mathrm{esc}}^{\mathrm{spec}}(\mathrm{Ly}\alpha)$.

The observed Ly α emission luminosity was computed as follows. First, the best-fit neutral ISM model (Section 3.3.1) was subtracted from the composite FUV spectrum, effectively removing both stellar and interstellar HI absorption. The resulting model-subtracted spectrum was integrated between the wavelength points where the Ly α emission line intersects the absorption trough in the original composite FUV spectrum, yielding $\langle L(Ly\alpha)_{obs} \rangle$. The intrinsic Ly α luminosity was computed by multiplying the dust-corrected H α luminosity, $L(H\alpha)$ (see Section 3.2.1), by the intrinsic Ly $\alpha/H\alpha$ ratio predicted by the best-fit photoionization model. This intrinsic ratio varies in the range $(Ly\alpha/H\alpha)_{int} = 8.99 - 9.58$ depending on the specific SPSneb model, photoionization model, and BPASS model type and is slightly larger than the canonically assumed value of $(Ly\alpha/H\alpha)_{int} = 8.7$ for an H II region temperature of $T_e = 10,000$ K. While $L(Ly\alpha)_{int}$ can also be computed from the best-fit SPSneb model (i.e., by integrating the model to obtain the ionizing photon production rate, $N(H^0)$; Section 4.2), the adopted method of computing $L(Ly\alpha)_{int}$ —i.e., based on $L(H\alpha)$ —obviates the need to account for the fraction of LyC photons that either are absorbed by dust (e.g., Inoue 2001) or escape the ISM of the galaxy, and thereby remains unavailable to photoionize hydrogen.

For reference, $\langle W_{\lambda}^{\rm em}({\rm Ly}\alpha)\rangle$ and $\langle f_{\rm esc}^{\rm spec}({\rm Ly}\alpha)\rangle$ are listed in Table 2 and shown in Figure 14, relative to the corresponding values of $\langle W_{\lambda}({\rm Ly}\alpha)\rangle$, for the 100bin models. The calculation of $\langle W_{\lambda}^{\rm em}({\rm Ly}\alpha)\rangle$ and $\langle f_{\rm esc}^{\rm spec}({\rm Ly}\alpha)\rangle$ depends on an accounting of underlying Ly α absorption—constrained through the neutral ISM modeling discussed in Section 3.3—and thus requires coverage of Ly β . In addition, $\langle f_{\rm esc}^{\rm spec}({\rm Ly}\alpha)\rangle$ requires coverage of the optical nebular emission lines to ensure an accurate estimate of the dust-corrected $\langle L({\rm H}\alpha)\rangle$. Thus, Figure 14 shows

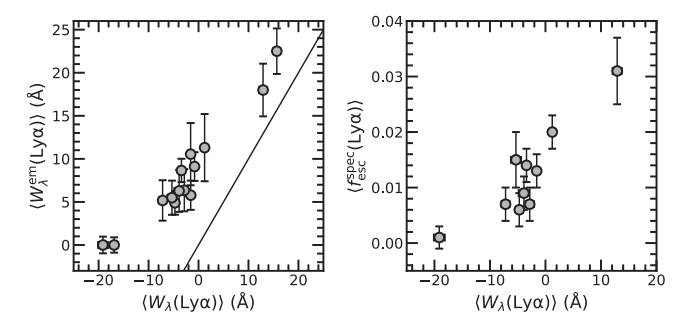


Figure 14. Left: emission-line $W_{\lambda}(\mathrm{Ly}\alpha)$, denoted by $\langle W_{\lambda}^{\mathrm{em}}(\mathrm{Ly}\alpha) \rangle$, vs. $\langle W_{\lambda}(\mathrm{Ly}\alpha) \rangle$ for the 14 subsamples with complete coverage of $\mathrm{Ly}\beta$ (Table 1). The solid line indicates the one-to-one relation. Right: escape fraction of $\mathrm{Ly}\alpha$, denoted by $\langle f_{\mathrm{esc}}^{\mathrm{spec}}(\mathrm{Ly}\alpha) \rangle$, vs. $\langle W_{\lambda}(\mathrm{Ly}\alpha) \rangle$ for the 10 subsamples with complete coverage of the optical nebular emission lines and $\mathrm{Ly}\beta$ (Table 1). The values shown assume the 100bin SPSneb models.

the relations between $\langle W_{\lambda}^{\rm em}({\rm Ly}\alpha)\rangle$ and $\langle W_{\lambda}({\rm Ly}\alpha)\rangle$ and between $\langle f_{\rm esc}^{\rm spec} ({\rm Ly}\alpha) \rangle$ and $\langle W_{\lambda}({\rm Ly}\alpha) \rangle$ for the 14 subsamples with complete coverage of Ly β and the 10 subsamples with complete coverage of Ly β and the optical nebular emission lines, respectively. Not surprisingly, many of the subsamples with $\langle W_{\lambda}(Ly\alpha)\rangle < 0$ A have a nonnegligible leakage of Ly α photons, where $\langle W_{\lambda}^{\rm em}({\rm Ly}\alpha)\rangle>0$ Å and $\langle f_{\rm esc}^{\rm spec}({\rm Ly}\alpha)\rangle>0$. As $L({\rm Ly}\alpha)_{\rm obs}$ increases and dominates over the underlying absorption, $\langle W_{\lambda}(Ly\alpha) \rangle$ approaches $\langle W_{\lambda}^{em}(Ly\alpha) \rangle$. Additionally, $\langle f_{\rm esc}^{\rm spec}({\rm Ly}\alpha) \rangle$ ranges from $\langle f_{\rm esc}^{\rm spec}({\rm Ly}\alpha) \rangle \simeq 0$ to 0.03 for ensembles with the lowest and highest measured $\langle W_{\lambda}(Ly\alpha)\rangle$, respectively. Evidently, the vast majority (\gtrsim 96%) of Ly α photons are either resonantly scattered out of the spectroscopic aperture or attenuated by dust. The computed values of $\langle W_{\lambda}^{\rm em}({\rm Ly}\alpha)\rangle$ and $\langle f_{\rm esc}^{\rm spec}({\rm Ly}\alpha)\rangle$ are examined in the context of the shape of the ionizing spectrum and gas covering fraction in the next section.

4.2. Primary Modulator of Escaping Ly\alpha Photons

As noted at the outset, a central focus of this work is to quantify the role of massive stars (i.e., the shape of the ionizing spectrum) and gas covering fraction on the emergent Ly α emission of high-redshift galaxies. There are a few salient points worth mentioning in the current context. First, $W_{\lambda}^{\rm em}({\rm Ly}\alpha)$ is sensitive to the shape of the ionizing spectrum, which determines the production of Ly α relative to the nonionizing FUV continuum, provided that there is sufficient HI gas to reprocess LyC photons into Ly α photons. Second, $W_{\lambda}^{\rm em}({\rm Ly}\alpha)$ is also sensitive to the dust column density and covering fraction of optically thick HI, as they determine the fraction of Ly α photons that emerge along the observer's sight line. On the other hand, $f_{\rm esc}^{\rm spec}({\rm Ly}\alpha)$ is insensitive to the ionizing spectrum for a fixed HI gas covering fraction and dust column density. In reality, of course, the ionizing spectrum may affect the H I gas covering fraction: e.g., a harder ionizing spectrum may lead to a larger fraction of ionized sight lines through which Ly α and LyC leakage can occur (i.e., a lower HI gas covering fraction; e.g., Erb et al. 2016; Trainor et al. 2016). Additionally, there is evidence that the dust column density, or reddening, correlates with HI covering fraction (e.g., Reddy et al. 2016b). These points are addressed below.

4.2.1. Quantifying the Shape of the Ionizing Spectrum

The shape of the ionizing spectrum of massive stars is determined by the BPASS model type (binary- vs. single-star evolution and IMF slope), Z_* , log[Age/yr], and the SFH (e.g., Stanway et al. 2016; Bouwens et al. 2016b; Steidel et al. 2016; Shivaei et al. 2018; Chevallard et al. 2018; Chisholm et al. 2019; Topping et al. 2020b). In Section 3.1.1, we motivated the choice of a constant star formation model in fitting the average FUV spectrum of an ensemble of $z \sim 2$ galaxies. Further, Section 3.2.4 presents evidence that SPS models including the effects of stellar binarity (100bin and 300bin models) are able to self-consistently explain the observed level of He II $\lambda 1640$ emission in the composite FUV spectra, while the single-star models cannot. Section 3.1.3 noted a marginal correlation between $\langle \log[\text{Age/yr}] \rangle$ and $\langle W_{\lambda}(\text{Ly}\alpha) \rangle$, while $\langle Z_{*}/Z_{\odot} \rangle$ appears to be uncorrelated with $\langle W_{\lambda}(Ly\alpha)\rangle$ (e.g., Figure 5). Based on these constraints, we can more directly examine the connection between the escape of Ly α photons and the shape (or hardness) of the ionizing spectrum by computing a commonly used proxy for the latter, namely, the ionizing photon production efficiency, ξ_{ion} (e.g., Robertson et al. 2013; Bouwens et al. 2016b; Shivaei et al. 2018; Theios et al. 2019):

$$\xi_{\rm ion} = \frac{N({\rm H}^0)}{L_{\rm FUV}} \,[{\rm s}^{-1}/{\rm erg}\;{\rm s}^{-1}\,{\rm Hz}^{-1}],$$
 (8)

where $N(\mathrm{H}^0)$ is the ionizing photon rate in s⁻¹ and L_{FUV} is the luminosity density at 1500 Å in erg s⁻¹ Hz⁻¹. ξ_{ion} is typically constrained by combining dust-corrected H α and FUV luminosities (e.g., Bouwens et al. 2016b; Matthee et al. 2017; Shivaei et al. 2018; Emami et al. 2020). In this work, ξ_{ion} was computed directly from the best-fit intrinsic SPSneb model, a route that obviates the need to apply potentially uncertain dust corrections to H α and FUV luminosities (Shivaei et al. 2018), account for LyC photons that may escape the ISM or be absorbed by dust (Inoue 2001), or implement conversions between H α luminosity and $N(\mathrm{H}^0)$ that may not apply to the galaxies in question (e.g., Reddy et al. 2016b; Theios et al. 2019). The ionizing photon rate was obtained by integrating the best-fit intrinsic SPSneb model:

$$N(\mathbf{H}^0) = \int_0^{912} \frac{\lambda l_{\lambda}}{hc} d\lambda, \tag{9}$$

where λ is in Å and l_{λ} is the luminosity density of the best-fit intrinsic SPSneb model in erg s⁻¹ Å⁻¹. Notwithstanding the aforementioned uncertainties in computing ξ_{ion} from dust-corrected H α and FUV luminosities, such estimates (Shivaei et al. 2018) are consistent with those derived directly from the SPSneb models for fixed assumptions of the nebular and stellar dust attenuation curves.

4.2.2. Relationships between Ly α Escape, ξ_{iow} and Gas Covering Fraction

The relationships between $\langle W_{\lambda}^{\rm em}({\rm Ly}\alpha)\rangle$ and $\langle\log[\xi_{\rm ion}/{\rm s}^{-1}/{\rm erg~s^{-1}~Hz^{-1}}]\rangle$ and between $\langle f_{\rm esc}^{\rm spec}({\rm Ly}\alpha)\rangle$ and $\langle\log[\xi_{\rm ion}/{\rm s^{-1}}/{\rm erg~s^{-1}~Hz^{-1}}]\rangle$ are shown in Figure 15. We do not find significant trends in either case, and the scatter in $\langle\log[\xi_{\rm ion}/{\rm s^{-1}}/{\rm erg~s^{-1}~Hz^{-1}}]\rangle$ at a fixed $\langle W_{\lambda}^{\rm em}({\rm Ly}\alpha)\rangle$ (or $\langle f_{\rm esc}^{\rm spec}({\rm Ly}\alpha)\rangle$) appears to be driven by differences in age of the stellar population, as demonstrated by the age color-coding

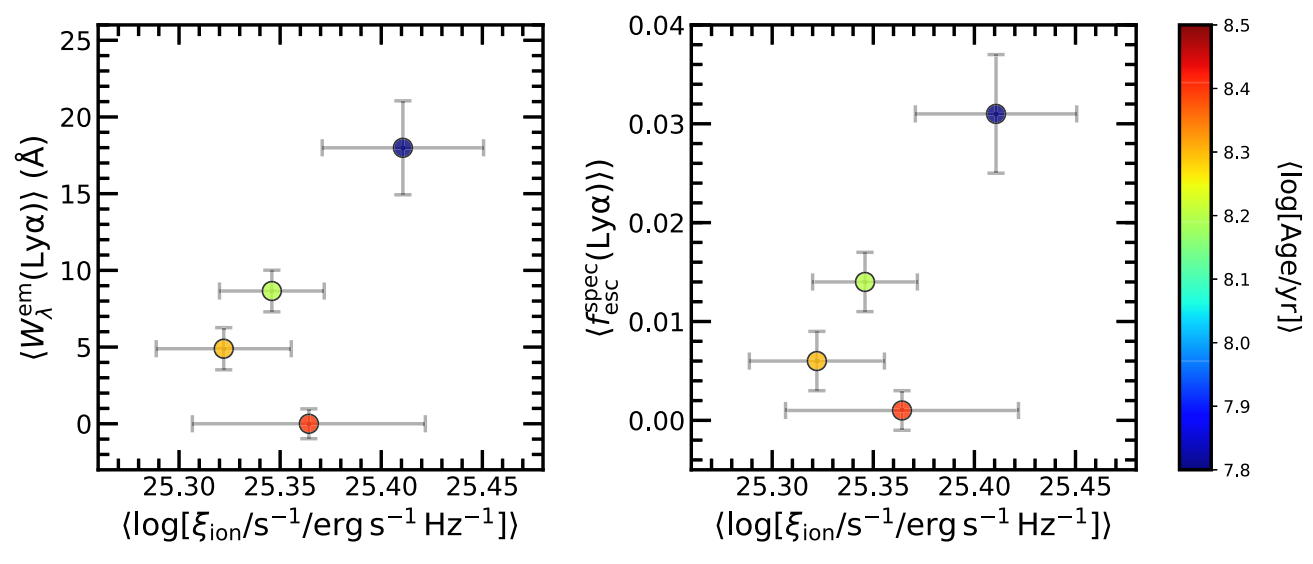


Figure 15. $\langle W_{\lambda}^{\rm em}({\rm Ly}\alpha)\rangle$ (left) and $\langle f_{\rm esc}^{\rm spec}({\rm Ly}\alpha)\rangle$ (right) vs. $\langle \log[\xi_{\rm ion}/{\rm s}^{-1}/{\rm erg}~{\rm s}^{-1}~{\rm Hz}^{-1}]\rangle$ for the ALN, WT1LN, WT2LN, and WT3LN subsamples which have complete coverage of Ly β and the optical nebular emission lines. The values assume the 100bin SPSneb models. Points are color-coded according to the best-fit log[Age/yr] (Section 3.1.3).

of the points shown in Figure 15. Subsamples with the youngest ages, $\langle \log[\mathrm{Age/yr}] \rangle \lesssim 8$, tend to have higher $\langle W_{\lambda}^{\mathrm{em}}(\mathrm{Ly}\alpha) \rangle$ and $\langle f_{\mathrm{esc}}^{\mathrm{spec}}(\mathrm{Ly}\alpha) \rangle$ on average, and they also have $\langle \log[\xi_{\mathrm{ion}}/\mathrm{s^{-1}/erg\ s^{-1}\ Hz^{-1}}] \rangle$ that are marginally (\simeq 0.1 dex) larger than those of subsamples with the oldest ages, $\langle \log[\mathrm{Age/yr}] \rangle \simeq 8.5$. A similar increase in ξ_{ion} for strong LAEs relative to continuum-selected galaxies has also been reported at $z \sim 3$ (Nakajima et al. 2018a). At any rate, the lack of a significant correlation between $\langle W_{\lambda}^{\mathrm{em}}(\mathrm{Ly}\alpha) \rangle$ and $\langle \log[\xi_{\mathrm{ion}}/\mathrm{s^{-1}/erg\ s^{-1}\ Hz^{-1}}] \rangle$, or between $\langle f_{\mathrm{esc}}^{\mathrm{spec}}(\mathrm{Ly}\alpha) \rangle$ and $\langle \log[\xi_{\mathrm{ion}}/\mathrm{s^{-1}/erg\ s^{-1}\ Hz^{-1}}] \rangle$, for galaxies in our sample strongly suggests that the observed variation in $W_{\lambda}(\mathrm{Ly}\alpha)$ is driven by factors other than—but which could still be influenced by—the shape of the ionizing spectrum. We return to a discussion of the scatter in the relationship between $\langle f_{\mathrm{cov}} \rangle$ and $\langle \log[\xi_{\mathrm{ion}}/\mathrm{s^{-1}/erg\ s^{-1}\ Hz^{-1}}] \rangle$ below.

The variations of $\langle W_{\lambda}^{\rm em}({\rm Ly}\alpha)\rangle$ and $\langle f_{\rm esc}^{\rm spec}({\rm Ly}\alpha)\rangle$ with gas covering fraction are directly shown in Figure 16 for the clumpy model of the ISM. Subsamples with $\langle W_{\lambda}^{\rm em}({\rm Ly}\alpha)\rangle > 10~{\rm Å}$ exclusively have $\langle f_{\rm cov}({\rm H\,I})\rangle \lesssim 0.94$, while those with $\langle W_{\lambda}^{\rm em}({\rm Ly}\alpha)\rangle < 10~{\rm Å}$ have $\langle f_{\rm cov}({\rm H\,I})\rangle \gtrsim 0.94$. Similar results are noted when considering $\langle f_{\rm cov}({\rm metal})\rangle$: subsamples with $\langle W_{\lambda}^{\rm em}({\rm Ly}\alpha)\rangle > 10~{\rm Å}$ exclusively have $\langle f_{\rm cov}({\rm metal})\rangle \lesssim 0.84$, while those with $\langle W_{\lambda}^{\rm em}({\rm Ly}\alpha)\rangle < 10~{\rm Å}$ have $\langle f_{\rm cov}({\rm metal})\rangle \gtrsim 0.84$. The significance of the difference in $\langle f_{\rm cov}({\rm metal})\rangle$ for independent subsamples (e.g., subsamples WT1 and WT3) is $\gtrsim 6\sigma$.

Unlike the case with $\langle \log [\xi_{\rm ion}/{\rm s}^{-1}/{\rm erg}~{\rm s}^{-1}~{\rm Hz}^{-1}] \rangle$, changes in $\langle f_{\rm cov} \rangle$ are more than sufficient to account for the full range of $\langle W_\lambda^{\rm em}({\rm Ly}\alpha) \rangle$. If the latter is solely dependent on the uncovered portion of the continuum, then $\langle W_\lambda^{\rm em}({\rm Ly}\alpha) \rangle$ should be directly proportional to $1-\langle f_{\rm cov}({\rm H~I}) \rangle$. Furthermore, if ${\rm Ly}\alpha$ photons are preferentially leaking from ionized or optically thin channels in the ISM, then $\langle f_{\rm esc}^{\rm spec}({\rm Ly}\alpha) \rangle \approx 1-\langle f_{\rm cov}({\rm H~I}) \rangle$. The bottom panel of Figure 16 shows that the $\gtrsim \! 10 \times \! {\rm variation}$ in the uncovered portion of the continuum for the subsamples is more than sufficient to account for the $\gtrsim \! 3 \times \! {\rm variation}$ in $\langle f_{\rm esc}^{\rm spec}({\rm Ly}\alpha) \rangle$. In the context of the screen model, there is significant dust

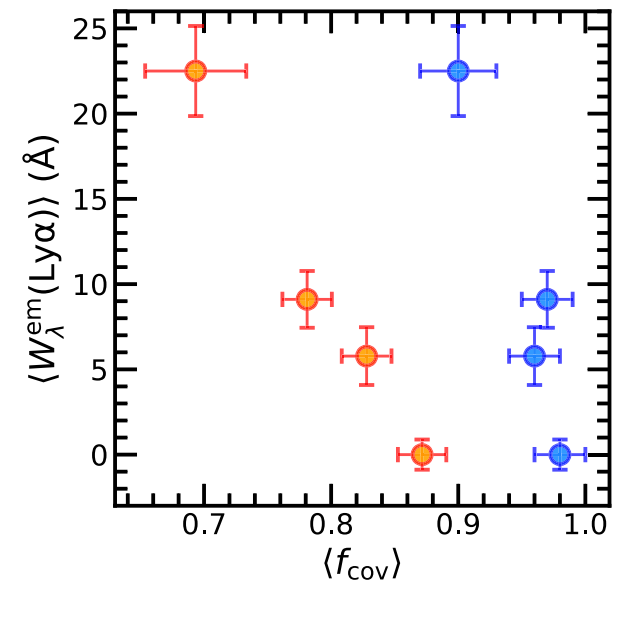
attenuation of Ly α photons (in the optically thin channels) that further modulates $\langle f_{\rm esc}^{\rm spec}({\rm Ly}\alpha)\rangle$.

4.2.3. Role of Gas Covering Fraction in Ly\alpha Escape

The results presented in the previous section imply that the covering fraction of high column density H I is likely a principal factor modulating $\langle f_{\rm esc}^{\rm spec}\,({\rm Ly}\alpha)\rangle$. This is perhaps not surprising given that even very small changes in $f_{\rm cov}({\rm H\,I})$ can lead to large variations in $W_\lambda^{\rm em}\,({\rm Ly}\alpha)$: e.g., for a fixed ionizing spectral shape, an $\approx 3\%$ decrease in $f_{\rm cov}({\rm H\,I})$ from 0.97 to 0.94 results in a factor of 2 increase in $\langle W_\lambda^{\rm em}\,({\rm Ly}\alpha)\rangle$ and $\langle f_{\rm esc}^{\rm spec}\,({\rm Ly}\alpha)\rangle$, assuming $\langle f_{\rm esc}^{\rm spec}\,({\rm Ly}\alpha)\rangle = 1 - \langle f_{\rm cov}\,({\rm H\,I})\rangle$. In other words, it is precisely because of the very large gas covering fraction that a small change in this fraction can lead to a dramatic variation in the line-of-sight (or down-the-barrel) Ly α luminosity. The bottom panel of Figure 16 demonstrates that our finding that a vast majority ($\gtrsim 95\%$) of Ly α photons are scattered out of (or removed from) the line of sight is consistent with the high covering fraction of optically thick gas inferred from the depths of the Lyman series absorption lines (Section 3.3.2).

Moreover, there are a number of subsamples where $1-\langle f_{\rm cov}({\rm H\,I})\rangle$ actually overpredicts $\langle f_{\rm esc}^{\rm spec}({\rm Ly}\alpha)\rangle$, i.e., $\langle f_{\rm esc}^{\rm spec}({\rm Ly}\alpha)\rangle$ $\lesssim 1-\langle f_{\rm cov}({\rm H\,I})\rangle$, implying that $\langle f_{\rm cov}({\rm H\,I})\rangle$ is a lower limit to the true covering fraction for the reasons discussed in Section 3.3.2. For example, the presence of unresolved moderate column density gas may further scatter ${\rm Ly}\alpha$ photons out of the line of sight. Figure 16 shows that $\langle f_{\rm esc}^{\rm spec}({\rm Ly}\alpha)\rangle$ still correlates with $1-\langle f_{\rm cov}({\rm H\,I})\rangle$ and that the (additional) opacity provided by moderate column density gas (or dust) increases with decreasing $\langle f_{\rm cov}({\rm H\,I})\rangle$ (see also Gazagnes et al. 2020; Kakiichi & Gronke 2021).

¹⁷ Reddy et al. (2016b) examined the relationship between $\langle f_{\rm esc}^{\rm spec}({\rm Ly}\alpha) \rangle$ and $\langle f_{\rm cov}({\rm H~I}) \rangle$ for composites constructed in bins of $E(B-V)_{\rm cont}$ for $\simeq L$ UV-selected galaxies at $z\sim 3$. They found a range of $\langle f_{\rm esc}^{\rm spec}({\rm Ly}\alpha) \rangle \simeq 0.01-0.18$ and $\langle f_{\rm esc}^{\rm spec}({\rm Ly}\alpha) \rangle \approx 1-\langle f_{\rm cov}({\rm H~I}) \rangle$ for all $E(B-V)_{\rm cont}$ bins except the bluest one, for which $\langle f_{\rm esc}^{\rm spec}({\rm Ly}\alpha) \rangle > 1-\langle f_{\rm cov}({\rm H~I}) \rangle$. In general, the $\langle f_{\rm esc}^{\rm spec}({\rm Ly}\alpha) \rangle$ derived here are lower than those obtained by Reddy et al. (2016b) at a fixed $\langle f_{\rm cov}({\rm H~I}) \rangle$, as the intrinsic $L({\rm H}\alpha)$ is larger at a fixed SFR when assuming the binary BPASS models.



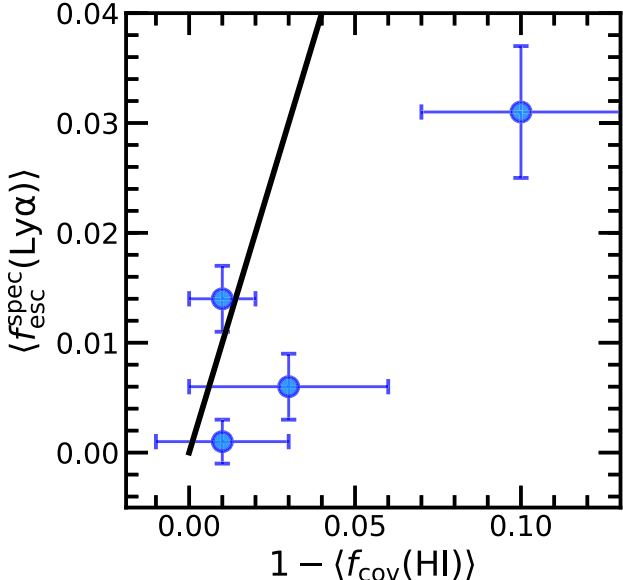


Figure 16. Top: $\langle W_{\lambda}^{\rm em}({\rm Ly}\alpha)\rangle$ vs. $\langle f_{\rm cov}({\rm H\,I})\rangle$ (blue) and $\langle f_{\rm cov}({\rm metal})\rangle$ (red) for the AL, WT1L, WT2L, and WT3L subsamples which have coverage of Ly β , assuming the clumpy ISM model. Bottom: $\langle f_{\rm esc}^{\rm spec}({\rm Ly}\alpha)\rangle$ vs. the uncovered fraction, $1-\langle f_{\rm cov}({\rm H\,I})\rangle$, for the ALN, WT1LN, WT2LN, and WT3LN subsamples which have coverage of Ly β and the optical nebular emission lines. The solid line indicates $f_{\rm esc}^{\rm spec}({\rm Ly}\alpha)=1-f_{\rm cov}({\rm H\,I})$.

Several previous investigations have also emphasized the role of gas covering fraction in the escape of Ly α and LyC photons (e.g., Rivera-Thorsen et al. 2015; Trainor et al. 2015; Dijkstra et al. 2016; Reddy et al. 2016b; Gazagnes et al. 2018; Chisholm et al. 2018; Steidel et al. 2018; Jaskot et al. 2019; Gazagnes et al. 2020; Matthee et al. 2021). We also highlight the recent study of Cullen et al. (2020), which finds that the variation in Z_* among the galaxies in their sample is insufficient to account for the range of observed $W_{\lambda}(\text{Ly}\alpha)$, and that some other factor (i.e., gas covering fraction) likely dominates the escape of Ly α . Our analysis points to a similar conclusion for typical star-forming galaxies at $z \sim 2$, based on the direct modeling of the interstellar H I absorption lines and the depths of saturated interstellar metal absorption lines in the composite FUV spectra.

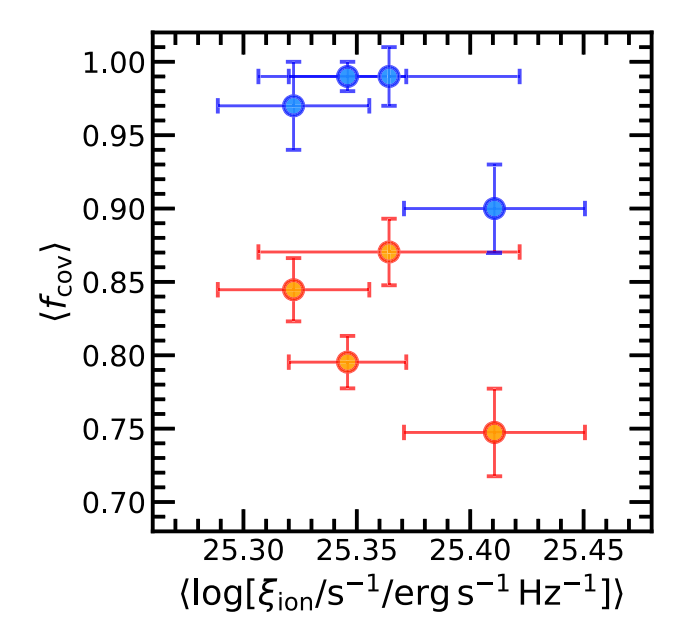


Figure 17. $\langle f_{\rm cov}({\rm H~I}) \rangle$ vs. $\langle \log[\xi_{\rm ion}/s^{-1}/{\rm erg~s^{-1}~Hz^{-1}}] \rangle$ (blue) and $\langle f_{\rm cov}({\rm metal}) \rangle$ vs. $\langle \log[\xi_{\rm ion}/s^{-1}/{\rm erg~s^{-1}~Hz^{-1}}] \rangle$ (red) for the ALN, WT1LN, WT2LN, and WT3LN subsamples which have coverage of Ly β and the optical nebular emission lines.

Finally, we briefly comment here on the large scatter in $\langle f_{\rm cov}({\rm H\,I}) \rangle$ and $\langle f_{\rm cov}({\rm metal}) \rangle$ at a given $\langle \log[\xi_{\rm ion}/{\rm s}^{-1}/{\rm erg\,s^{-1}\,Hz^{-1}}] \rangle$ (e.g., Figure 17). In particular, subsamples with the highest H I (near unity) or metal covering fractions have $\langle \log[\xi_{\rm ion}/{\rm s^{-1}/erg\,s^{-1}\,Hz^{-1}}] \rangle$ that are consistent within the sampling errors with the values obtained for galaxies with lower $\langle f_{\rm cov}({\rm H\,I}) \rangle$. These results suggest that the shape of the ionizing spectrum is not the sole determinative factor in the covering fraction. Section 4.3 presents evidence that another factor, namely, the compactness of star formation, likely plays an important role in determining the covering fraction.

In summary, the preference for binary stellar evolution models irrespective of $\langle W_{\lambda}(Ly\alpha)\rangle$ (Section 3.2.4), the absence of any significant variation of $\langle Z_* \rangle$ with $\langle W_{\lambda}(\mathrm{Ly}\alpha) \rangle$ (Section 3.1.3), and the modest anticorrelation between $\langle \log[\text{Age/yr}] \rangle$ and $\langle W_{\lambda}(\text{Ly}\alpha) \rangle$ (Section 3.1.3) together imply a narrow range of $\langle \log[\xi_{\rm ion}/{\rm s}^{-1}/{\rm erg~s}^{-1}\,{\rm Hz}^{-1}]\rangle \simeq 25.30$ 25.40. This range is insufficient to account for the large variation in $\langle W_{\lambda}^{\text{em}}(\text{Ly}\alpha)\rangle$ observed for galaxies in our sample. On the other hand, the inferred range of $\langle f_{\rm cov}({\rm H\,I}) \rangle$ (Section 3.3.2) is more than sufficient to account for the variation in $\langle W_{\lambda}^{\text{em}}(\text{Ly}\alpha)\rangle$ observed for galaxies in our sample. Furthermore, $\langle f_{\rm esc}^{\rm spec}({\rm Ly}\alpha)\rangle$ correlates with $1-\langle f_{\rm cov}({\rm H\,I})\rangle$ in the manner one would expect if most of the Ly α opacity is due to foreground optically thick H I (or dust, in the case of the screen model). Accordingly, the covering fraction of optically thick H I (or dust) is the dominant factor in modulating Ly α emission within the spectroscopic aperture, while the shape of the ionizing spectrum—parameterized by ξ_{ion} —plays a minor role in modulating the emergent Ly α emission of the galaxies analyzed here.

4.3. Impact of the SFR Surface Density and Gravitational Potential on the Escape of Ly α and the Ionization Parameter

Section 4.2 presents evidence that the covering fraction of optically thick H I is the dominant factor in modulating

 $\langle W_{\lambda}^{\rm em}({\rm Ly}\alpha) \rangle$ and $\langle f_{\rm esc}^{\rm spec}({\rm Ly}\alpha) \rangle$ among the galaxies in our sample. The question remains as to the properties of galaxies that regulate the H_I covering fraction. The radiative, thermal, and mechanical feedback from star formation, stellar winds, and/or supernovae can promote the formation of ionized and/ or low column density channels in the ISM (and CGM), providing pathways through which Ly α and LyC photons can escape galaxies (e.g., Gnedin et al. 2008; Ma et al. 2016; Kimm et al. 2019; Ma et al. 2020; Cen 2020; Kakiichi & Gronke 2021). Both theoretical and observational work suggests that the impact of these "feedback" effects on the surrounding ISM, and the subsequent escape of Ly α and LyC photons, can be enhanced in regions of compact star formation (e.g., Ma et al. 2016; Sharma et al. 2016; Verhamme et al. 2017; Marchi et al. 2019; Cen 2020; Naidu et al. 2020), typically expressed by the SFR surface density, $\Sigma_{\rm SFR}$, in units of M_{\odot} yr⁻¹ kpc⁻². The deep CANDELS imaging in the MOSDEF survey fields allows us to examine the connection between Ly α escape and $\Sigma_{\rm SFR}$ through the measurement of galaxy sizes. In addition, while previous analyses have focused almost exclusively on the impact of Σ_{SFR} on the escape of Ly α and LyC photons, the galaxy potential may also play an important role (e.g., Kim et al. 2020). For example, the feedback associated with a fixed Σ_{SFR} may be more efficient in clearing sight lines in the ISM of a low-mass (low escape velocity) galaxy relative to a high-mass (high escape velocity) galaxy. This possibility is explored below by also considering $\Sigma_{\rm SFR}$ normalized by stellar mass, M_* . Section 4.3.1 describes the calculation of $\Sigma_{\rm SFR}$ and its normalization by M_* , while the correlation between Ly α escape and these quantities is discussed in Section 4.3.2. Section 4.3.3 concludes with a discussion of the correlation between the compactness of star formation and ionization parameter.

4.3.1. Parameterization of the Distribution of SFR and Galaxy Potential

The distribution, or compactness, of star formation is typically parameterized by the SFR surface density, $\Sigma_{\rm SFR}$:

$$\Sigma_{\rm SFR} = \frac{\rm SFR(H\alpha)}{2\pi R_{\circ}^2},\tag{10}$$

where R_e is the effective radius within which half the total light of the galaxy is contained. These half-light radii were obtained from the single-component Sérsic fits to the HST/F160W images of the MOSDEF-LRIS galaxies, as compiled in van der Wel et al. (2014). Note that $\Sigma_{\rm SFR}$ was computed assuming SFR (H α). Adopting the SFR(SED) inferred from broadband SED modeling (Section 2.3.3) does not significantly affect any of our conclusions.

For individual galaxies for which $H\alpha$ and $H\beta$ are both detected with $S/N \geqslant 3$, SFR($H\alpha$) was computed by multiplying the dust-corrected $L(H\alpha)$ for each galaxy (Section 3.2.1) by the factor $2.12 \times 10^{-42}\,M_\odot$ yr $^{-1}$ erg $^{-1}$ s, appropriate for the $Z_* = 0.001$ 100bin SPSneb models—i.e., the same models assumed in fitting the broadband photometry (Section 2.3.3). For ensembles containing galaxies with complete coverage of the optical nebular emission lines, $\langle SFR(H\alpha) \rangle$ was computed by multiplying the dust-corrected $\langle L(H\alpha) \rangle$ by the factor derived from the best-fitting SPSneb model. This factor is similar to the one used for individual galaxies and depends on the exact age and metallicity of the SPSneb model that best fits the composite

FUV spectrum. Furthermore, these values of $\langle SFR(H\alpha) \rangle$ were divided by $\langle f_{cov}(H\,I) \rangle$ inferred from the clumpy ISM model (Section 3.3.1) to account for the fraction of ionizing photons that escape and are therefore unavailable for generating Balmer recombination photons. $\Sigma_{SFR(H\alpha)}$ for individual galaxies and ensembles were then computed from the SFR(H α), assuming the individual and mean R_e , respectively.

To examine the dependence of Ly α escape on gravitational potential, we computed $\Sigma_{SFR(H\alpha)}$ normalized by stellar mass:

$$\Sigma_{\rm sSFR} = \frac{\Sigma_{\rm SFR}}{M_*} = \frac{\rm SFR(H\alpha)}{2\pi R_{\rm e}^2 M_*},\tag{11}$$

where the subscript "sSFR" refers to the specific SFR based on $H\alpha$, and M_* is used as a proxy for the galaxy potential. For simplicity, the factor of 2 in the denominator is retained—a choice that does not affect any of the relative trends examined in this work—as the impact of feedback on the ISM is likely to be sensitive to the entire galaxy mass, not just that contained within the half-light radius.

Galaxies were grouped together based on their individually measured $\Sigma_{\rm SFR}$ and $\Sigma_{\rm sSFR}$ to form subsamples ST1 through ST3 and sST1 through sST3, respectively (Table 1). The best-fit parameters obtained from fitting the composite spectra of these subsamples are listed in Table 2, and the average sizes, stellar masses, SFR(H α), $\Sigma_{\rm SFR}$, and $\Sigma_{\rm sSFR}$ for all the relevant subsamples (i.e., those with coverage of Ly β and the optical nebular emission lines) are given in Table 7.

4.3.2. Connection between Ly\alpha Escape and the SFR Distribution and Galaxy Potential

The correlations between $W_{\lambda}(\mathrm{Ly}\alpha)$ and R_e , SFR, and M_* for individual galaxies are presented in Appendix D. Here we focus on the individual and composite measurements of Σ_{SFR} and Σ_{SSFR} and their impact on $\mathrm{Ly}\alpha$ escape. If concentrated star formation and a shallower galaxy potential lead to conditions favorable for the formation of ionized or low column density channels in the ISM, then we expect the gas covering fraction to correlate with Σ_{SFR} and Σ_{sSFR} . Figure 18 shows the variation of $\langle f_{\mathrm{cov}}(\mathrm{H~I}) \rangle$ and $\langle f_{\mathrm{cov}}(\mathrm{metal}) \rangle$ with $\langle \Sigma_{\mathrm{SFR}} \rangle$ and $\langle \Sigma_{\mathrm{sSFR}} \rangle$.

The left panel of Figure 18 shows that there is no significant difference in $\langle f_{\rm cov}({\rm H\,I})\rangle$ for galaxies in the lowest and highest $\Sigma_{\rm SFR}$ bins. There is a marginally significant difference (${\simeq}2\sigma$) in $\langle f_{\rm cov}({\rm metal})\rangle$ for the same two bins: galaxies in the upper third of the $\Sigma_{\rm SFR}$ distribution have lower $\langle f_{\rm cov}({\rm metal})\rangle$ than galaxies in the lower third of the $\Sigma_{\rm SFR}$ distribution. There does not appear to be a clear monotonic relation between either $\langle f_{\rm cov}({\rm H\,I})\rangle$ or $\langle f_{\rm cov}({\rm metal})\rangle$ and $\langle \Sigma_{\rm SFR}\rangle$ over the dynamic range probed by the MOSDEF-LRIS sample.

In contrast to their lack of obvious correlation with $\langle \Sigma_{\rm SFR} \rangle$, $f_{\rm cov}({\rm H~I})$ and $f_{\rm cov}({\rm metal})$ appear to be significantly anticorrelated with $\langle \Sigma_{\rm sSFR} \rangle$. For example, galaxies in the upper third of the

 $[\]overline{^{18}}$ Galaxy potentials based on dynamical and baryonic masses will be considered elsewhere. For the time being, we note that Price et al. (2020) find a highly significant correlation between dynamical and stellar mass for $z\sim2$ galaxies in the MOSDEF sample: a Spearman test of the correlation between these two variables yields $\rho=0.67$ with a probability of $p=5.19\times10^{-44}$ of a null correlation. Thus, we use M_* as a proxy for galaxy potential, given that this parameter is available for every galaxy in the sample.

 $^{^{19}}$ The grouping of galaxies based on their $\Sigma_{\rm SFR}$ and $\Sigma_{\rm sSFR}$ requires that they have detected $H\alpha$ and $H\beta$ emission lines. However, we note that grouping galaxies based on $\Sigma_{\rm SFR(SED)}$ and $\Sigma_{\rm sSFR(SED)}$ (which do not require individual $H\alpha$ and $H\beta$ detections) yields results similar to those presented here.

| Table 7 | | | | | | |
|--|--|--|--|--|--|--|
| Galaxy Sizes, SFR(H α), Σ_{SFR} , and Σ_{SSFR} | | | | | | |

| Subsample | $\langle R_e angle^{ m a} \ m (kpc)$ | ${\langle M_* angle^{ m b}} \ (10^{10}M_\odot$) | $\langle SFR(H\alpha) \rangle^{c}$ $(M_{\odot} \text{ yr}^{-1})$ | $\langle \Sigma_{\rm SFR} \rangle^{\rm d} \ (M_{\odot} \ {\rm yr}^{-1} \ {\rm kpc}^{-2})$ | $(\Sigma_{\rm sSFR})^{\rm e}$ $({\rm Gyr}^{-1}{\rm kpc}^{-2})$ |
|-------------------------|--|---|---|---|---|
| ALN | 2.32 ± 0.02 | 1.11 ± 0.03 | 16.14 ± 2.49 | 0.479 ± 0.083 | 0.044 ± 0.008 |
| WT1LN WT2LN WT3LN | $\begin{array}{c} 2.31 \pm 0.02 \\ 2.67 \pm 0.02 \\ 2.05 \pm 0.01 \end{array}$ | 1.24 ± 0.03 1.17 ± 0.03 0.99 ± 0.02 | 17.08 ± 7.55 23.15 ± 8.34 19.27 ± 4.18 | $\begin{array}{c} 0.521 \pm 0.258 \\ 0.507 \pm 0.174 \\ 0.751 \pm 0.191 \end{array}$ | 0.043 ± 0.020 0.046 ± 0.018 0.080 ± 0.031 |
| ST1L ST2L ST3L | 3.12 ± 0.04 2.57 ± 0.01 1.30 ± 0.00 | 0.97 ± 0.02 1.63 ± 0.04 0.94 ± 0.02 | 10.08 ± 3.75 26.96 ± 6.31 32.51 ± 11.60 | $\begin{array}{c} 0.163 \pm 0.051 \\ 0.660 \pm 0.155 \\ 3.012 \pm 1.032 \end{array}$ | 0.017 ± 0.006 0.041 ± 0.012 0.318 ± 0.097 |
| sST1L sST2L sST3L | 3.39 ± 0.02 2.37 ± 0.02 1.36 ± 0.00 | 1.82 ± 0.05 1.23 ± 0.03 0.51 ± 0.01 | 17.64 ± 6.08 26.23 ± 7.87 20.37 ± 5.96 | $\begin{array}{c} 0.241 \pm 0.076 \\ 0.755 \pm 0.250 \\ 1.752 \pm 0.538 \end{array}$ | $0.013 \pm 0.004 \\ 0.061 \pm 0.018 \\ 0.355 \pm 0.114$ |

Notes.

 $\Sigma_{\rm sSFR}$ distribution have $\langle f_{\rm cov}({\rm H~I}) \rangle = 0.91 \pm 0.02$, while those in the lower third have $\langle f_{\rm cov}({\rm H~I}) \rangle = 0.99 \pm 0.02$, a difference that is significant at the $\approx 3\sigma$ level. Similarly, there is a large and significant difference in $\langle f_{\rm cov}({\rm metal}) \rangle$ for galaxies in the upper and lower third of $\Sigma_{\rm sSFR}$. Similar conclusions are reached if we consider $\langle f_{\rm cov}({\rm H~I}) \rangle$ and $\langle f_{\rm cov}({\rm metal}) \rangle$ from the screen model.

The difference in $\langle f_{\rm cov}({\rm H\,I}) \rangle$ (and $\langle f_{\rm cov}({\rm metal}) \rangle$) between the upper and lower third of the $\Sigma_{\rm sSFR}$ distribution is both larger and more significant than the difference in the covering fraction in the upper and lower third of the $\Sigma_{\rm SFR}$ distribution. Additionally, there is a clear monotonic trend between covering fraction and $\langle \Sigma_{\rm sSFR} \rangle$, while no such trend is apparent between covering fraction and $\langle \Sigma_{\rm sSFR} \rangle$. These results point to a tighter anticorrelation between $\langle f_{\rm cov}({\rm H\,I}) \rangle$ and $\langle \Sigma_{\rm sSFR} \rangle$ than between $\langle f_{\rm cov}({\rm H\,I}) \rangle$ and $\langle \Sigma_{\rm sSFR} \rangle$, in accordance with the expectation that the gravitational potential may play a role in the impact of feedback on gas covering fraction. Fitting the independent subsamples in bins of $\Sigma_{\rm sSFR}$ yields the following relation:

$$\langle f_{\rm cov}({\rm H\,I}) \rangle = -0.056 \log \left[\frac{\langle \Sigma_{\rm sSFR} \rangle}{{\rm Gyr}^{-1} \, {\rm kpc}^{-2}} \right] + 0.884, \quad (12)$$

for $0.01 \lesssim \Sigma_{\rm sSFR} \lesssim 0.3~{\rm Gyr}^{-1}\,{\rm kpc}^{-2}$ (thick purple line in the right panel of Figure 18).

The possibility that covering fraction anticorrelates more tightly with $\Sigma_{\rm sSFR}$ than with $\Sigma_{\rm SFR}$ suggests that the covering fraction should correlate with M_* . As shown in Figure 19, galaxies with lower stellar masses have lower HI and metal covering fractions. Ensembles with $\langle M_* \rangle \gtrsim 10^{10}~M_{\odot}$ have $\langle f_{\rm cov}({\rm H\,I}) \rangle \gtrsim 0.95$, while those with $\langle M_* \rangle \lesssim 10^{10}~M_{\odot}$ have $\langle f_{\rm cov}({\rm H\,I}) \rangle \lesssim 0.95$. For subsamples with $\langle \log[M_*/M_{\odot}] \rangle \lesssim 9.8$, unity covering fractions of HI can be ruled out with $\gtrsim 3\sigma$ confidence. The difference in the covering fraction of metalbearing gas between low- and high-mass galaxies is even more pronounced: subsamples with $\langle \log[M_*/M_{\odot}] \rangle \lesssim 10.0$ have $\langle f_{\rm cov}({\rm metal}) \rangle \lesssim 0.80$, signifying a $\gtrsim 10\sigma$ difference from the $\langle f_{\rm cov}({\rm metal}) \rangle \simeq 0.90$ for subsamples with $\langle \log[M_*/M_{\odot}] \rangle \gtrsim 10.2$. In the present framework, the correlation between covering fraction and M_* is driven by the higher $\Sigma_{\rm SFR}$ and

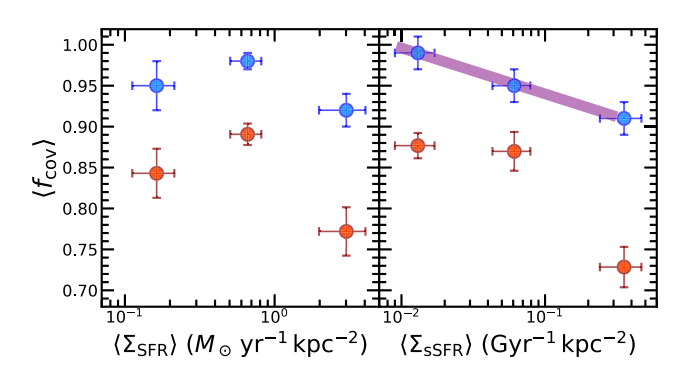


Figure 18. Dependence of H I (blue) and metal covering fraction (red) on $\Sigma_{\rm SFR}$ (left) and $\Sigma_{\rm sSFR}$ (right) for, respectively, the ST and sST subsamples with coverage of Ly β , assuming the clumpy ISM model. The thick purple line in the top right panel denotes a linear fit to the independent subsamples constructed in bins of $\Sigma_{\rm sSFR}$, indicating $\langle f_{\rm cov} ({\rm H~I}) \rangle \propto -0.056 \log[\langle \Sigma_{\rm sSFR} \rangle / {\rm Gyr}^{-1} \, {\rm kpc}^{-2}]$ (see Equation (12)).

lower gravitational potential associated with low-mass galaxies, conditions favorable for an increased ISM porosity.

A more detailed investigation of the effects of compact star formation and the galaxy potential on gas kinematics will be presented elsewhere. For the time being, note that the anticorrelation between covering fraction and $\Sigma_{\rm sSFR}$ comports with the expectation that compact star formation in a low gravitational potential has the effect of decreasing the covering fraction of optically thick H I. As a consequence, $W_{\lambda}({\rm Ly}\alpha)$, $W_{\lambda}^{\rm em}({\rm Ly}\alpha)$, and $f_{\rm esc}^{\rm spec}$ (Ly α) are all expected to increase in such cases.

The correlations between $W_{\lambda}(\mathrm{Ly}\alpha)$ and both Σ_{SFR} and Σ_{sSFR} are shown for individual objects and subsamples in Figure 20. There is a high probability $(p_{\mathrm{ind}}=0.28)$ of a null correlation between $W_{\lambda}(\mathrm{Ly}\alpha)$ and Σ_{SFR} for individual galaxies, though we do find more significant differences in the average values computed for the subsamples. For example, the subsample with the highest $\langle \Sigma_{\mathrm{SFR}} \rangle$ has $\langle W_{\lambda}(\mathrm{Ly}\alpha) \rangle \gtrsim -1.5 \, \text{Å}$, while the one with the lowest $\langle \Sigma_{\mathrm{SFR}} \rangle$ has $\langle W_{\lambda}(\mathrm{Ly}\alpha) \rangle \simeq -5 \, \text{Å}$, a difference in $\langle W_{\lambda}(\mathrm{Ly}\alpha) \rangle$ that is significant at the $\simeq 3.5\sigma$ level. Individual galaxies exhibit a correlation between $W_{\lambda}(\mathrm{Ly}\alpha)$ and Σ_{sSFR} that

^a Mean effective radius.

^b Mean stellar mass.

^c Mean SFR(H α), corrected for the fraction of ionizing photons that escape the galaxies based on $f_{cov}(H I)$ inferred from the clumpy ISM model (see text).

^d Mean $\Sigma_{\rm SFR}$, assuming SFR(Hlpha).

^e Mean $\Sigma_{\rm SSFR}$, assuming SFR(H α).

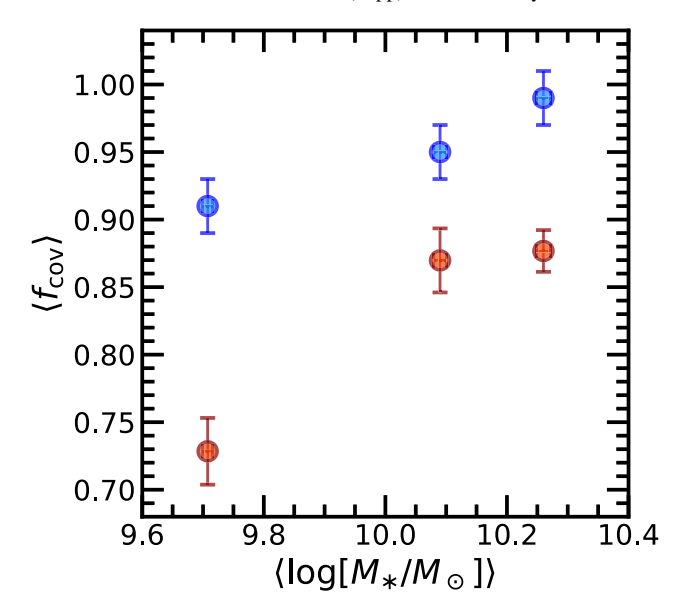


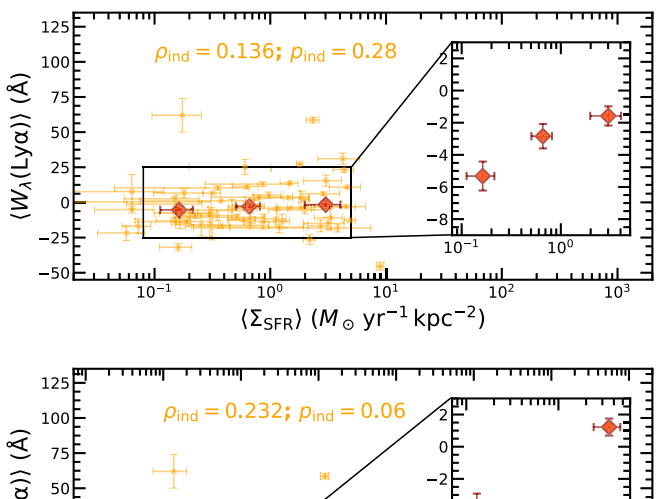
Figure 19. Correlation of $\langle f_{\rm cov}({\rm H~I}) \rangle$ (blue points) and $\langle f_{\rm cov}({\rm metal}) \rangle$ (red points) with average stellar mass, $\langle M_* \rangle$, for subsamples sST1L, sST2L, and sST3L.

is more significant than the one between $W_{\lambda}(\mathrm{Ly}\alpha)$ and Σ_{SFR} . Furthermore, the subsample with the highest $\langle \Sigma_{\mathrm{sSFR}} \rangle$ has $\langle W_{\lambda}(\mathrm{Ly}\alpha) \rangle \simeq 1$ Å compared to $\langle W_{\lambda}(\mathrm{Ly}\alpha) \rangle \simeq -4$ to -7 Å for subsamples with lower $\langle \Sigma_{\mathrm{sSFR}} \rangle$, a difference that is significant at the $\gtrsim 4\sigma$ level. Interestingly, we do not find a monotonic trend between $\langle W_{\lambda}(\mathrm{Ly}\alpha) \rangle$ and $\langle \Sigma_{\mathrm{sSFR}} \rangle$ for the composite measurements, suggesting a large scatter in the relationship between these two quantities (see discussion in Section 4.4).

Figure 21 shows the variation of $\langle f_{\rm esc}^{\rm spec} ({\rm Ly}\alpha) \rangle$ with $\langle \Sigma_{\rm SFR} \rangle$ and $\langle \Sigma_{\rm sSFR} \rangle$. The difference in $\langle f_{\rm esc}^{\rm spec} ({\rm Ly}\alpha) \rangle$ between the upper and lower third of the $\Sigma_{\rm SFR}$ distribution is not as pronounced as it is between the upper and lower third of the $\Sigma_{\rm sSFR}$ distribution. The significance of the difference in $\langle W_{\lambda}(Ly\alpha)\rangle$ and $\langle f_{\rm esc}^{\rm spec}({\rm Ly}\alpha)\rangle$ for galaxies in the upper and lower thirds of the $\Sigma_{\rm sSFR}$ distribution relative to that obtained for the upper and lower thirds of the Σ_{SFR} distribution suggests that the gravitational potential may be a relevant factor in the escape of Ly α photons (see also Kim et al. 2020), consistent with a framework in which compact star formation in a shallow potential results in lower gas covering fractions (Figure 18 and associated discussion). Data sets spanning a larger dynamic range in $W_{\lambda}(\text{Ly}\alpha)$, $f_{\text{cov}}(\text{H I})$, $f_{\text{cov}}(\text{metal})$, Σ_{SFR} , and Σ_{sSFR} will be needed to confirm these preliminary results regarding the role of the gravitational potential in modulating $f_{cov}(H I)$ and, as a consequence, $f_{\rm esc}^{\rm spec}$ (Ly α).

4.3.3. Impact of the SFR Distribution on Ionization Parameter

One significant difference between subsamples with high and low $\langle W_{\lambda}(\mathrm{Ly}\alpha) \rangle$ is in their ionization parameters (Section 3.2.5), where subsamples with higher $\langle W_{\lambda}(\mathrm{Ly}\alpha) \rangle$ also have higher $\langle \log U \rangle$ (e.g., Figure 10). As per the discussion in Sections 3.2.2 and 3.2.3 and Figures 6 and 7, $\langle \log U \rangle$ is insensitive to the BPASS model type and the range of ionizing spectra indicated by the best-fit SPSneb models. The question then remains as to the physical cause of the change in $\langle \log U \rangle$ with $\langle W_{\lambda}(\mathrm{Ly}\alpha) \rangle$. Section 4.3.2 presents evidence that compact star formation in a shallow potential yields conditions (i.e., lower gas covering fractions) favorable for the escape of $\mathrm{Ly}\alpha$ photons. Here we suggest that changes in the compactness of



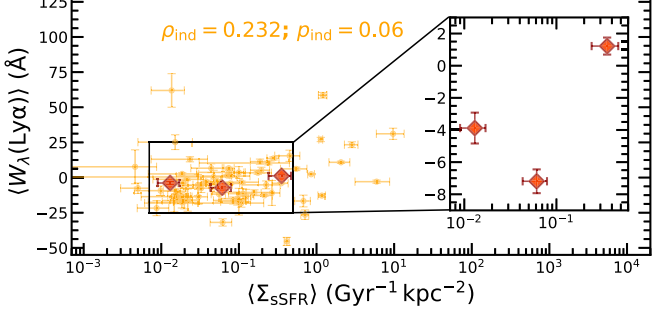


Figure 20. $W_{\lambda}(\mathrm{Ly}\alpha)$ vs. Σ_{SFR} (top) and Σ_{sSFR} (bottom) for individual galaxies and subsamples. Small orange points indicate individual galaxies. The Spearman correlation coefficient (ρ_{ind}) and p-value (p_{ind}) between $W_{\lambda}(\mathrm{Ly}\alpha)$ and Σ_{SFR} and between $W_{\lambda}(\mathrm{Ly}\alpha)$ and Σ_{SFR} are indicated in each panel. Large red diamonds indicate values for subsamples constructed in bins of Σ_{SFR} and Σ_{sSFR} .

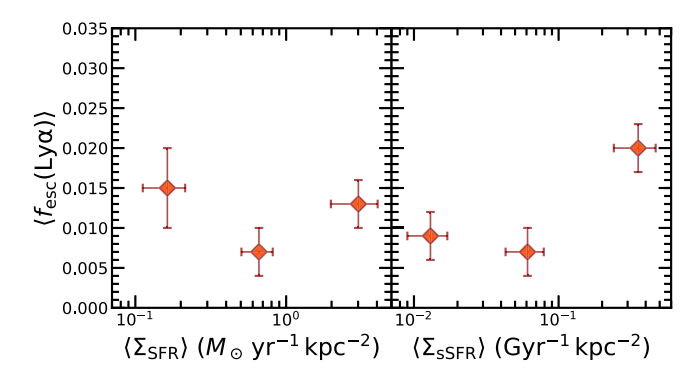


Figure 21. $\langle f_{\rm ssc}^{\rm spec}({\rm Ly}\alpha) \rangle$ as a function of $\langle \Sigma_{\rm SFR} \rangle$ (left) and $\langle \Sigma_{\rm sSFR} \rangle$ (right) for subsamples constructed in bins of $\langle \Sigma_{\rm SFR} \rangle$ and $\langle \Sigma_{\rm sSFR} \rangle$, respectively, and with coverage of ${\rm Ly}\beta$.

star formation may also be responsible for the observed variation in $\langle \log U \rangle$.

In particular, Shimakawa et al. (2015) find a significant correlation between Σ_{SFR} and n_e for z = 2.5 galaxies, such that

$$n_e \propto \Sigma_{\rm SFR}^{1/S_{n_e}},\tag{13}$$

where $S_{n_e} = 1.7 \pm 0.3$. This correlation may be a consequence of the relationship between star formation activity and interstellar pressure in H II regions (Shimakawa et al. 2015) and may further imply a connection between the electron and cold gas densities, even though the two are sensitive to gas on different physical scales (i.e., 50–100 pc scales for the densities of H II regions vs. \sim 1 kpc scales for the density of cold gas;

e.g., Shirazi et al. 2014; Shimakawa et al. 2015; Jiang et al. 2019; Davies et al. 2021).²⁰

The SFR density within a sphere of radius R can be written as

$$n_{\rm SFR} \propto \frac{\Sigma_{\rm SFR}}{R} \propto \Sigma_{\rm SFR}^{[1-1/S_R]},$$
 (14)

where $S_R = -2.82 \pm 0.16$ based on fitting the relationship between $\log[\Sigma_{\rm SFR}/M_{\odot}~{\rm yr^{-1}~kpc^{-2}}]$ and $\log[R/{\rm kpc}]$ for the independent bins of $\Sigma_{\rm SFR}$. The number density of ionizing photons is proportional to the product of $n_{\rm SFR}$ and $\xi_{\rm ion}$:

$$n_{\gamma} \propto n_{\rm SFR} \xi_{\rm ion},$$
 (15)

such that an increase in $n_{\rm SFR}$ by some factor results in a similar factor increase in n_{γ} at a fixed $\xi_{\rm ion}$ and, likewise, an increase in $\xi_{\rm ion}$ by some factor results in a similar factor increase in n_{γ} at a fixed $n_{\rm SFR}$. We do not find a significant correlation between $\xi_{\rm ion}$ and $\Sigma_{\rm SFR}$, and therefore we assume

$$n_{\gamma} \propto \Sigma_{\rm SFR}^{[1-1/S_R]} \tag{16}$$

based on Equation (14).

Combining Equations (13) and (16) with the definition of the ionization parameter as $U \equiv n_{\gamma}/n_e$ yields the following relationship:

$$\log U \propto \left[1 - \frac{1}{S_R} - \frac{1}{S_{n_e}}\right] \log[\Sigma_{SFR}/M_{\odot} \text{ yr}^{-1} \text{ kpc}^{-2}]. \quad (17)$$

The shaded region in Figure 22 depicts the 95% confidence interval on the slope of Equation (17), where the relationship has been normalized to pass through the point $(\langle \Sigma_{SFR} \rangle_0, \langle \log U \rangle_0) = (0.5 \, M_\odot \, \text{yr}^{-1} \, \text{kpc}^{-2}, -3.0)$.

The relationship between $\log U$ and $\Sigma_{\rm SFR}$ is undoubtedly more complicated than what we have approximated here given the large differences in physical scales associated with the ionized and cold gas, and the ambiguity in the physical interpretation of $\log U$ for geometries that depart from the simple ones (plane-parallel or spherical) assumed in the photoionization modeling (Section 3.2.1). In spite of these complications, the simplified assumptions adopted here predict a relationship between $\log U$ and $\Sigma_{\rm SFR}$ that lies within a factor of $\lesssim 2$ of the measurements for most of the subsamples considered in this work (Figure 22). Thus, the apparent superlinear dependence of $\Sigma_{\rm SFR}$ on n_e (Equation (13)) could plausibly explain at least part of the dependence of $\log U$ on $\Sigma_{\rm SFR}$.

A principal consequence of the dependence of $W_{\lambda}(\text{Ly}\alpha)$ on covering fraction (Section 4.2) is that $\text{Ly}\alpha$ visibility is a highly stochastic function of viewing angle and that a high $W_{\lambda}(\text{Ly}\alpha)$ may signal the fortuitous alignment of a low column density and/or ionized channel in the ISM with the observer's line of sight as has been suggested by radiative transfer simulations (see also Verhamme et al. 2012; Behrens & Braun 2014; Behrens et al. 2019; Smith et al. 2019; Mauerhofer et al. 2021).

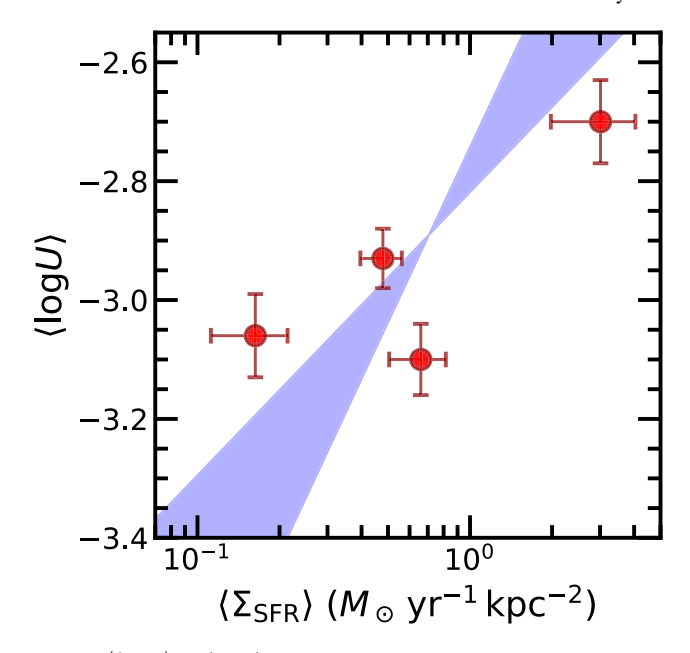


Figure 22. $\langle \log U \rangle$ vs. $\langle \Sigma_{\rm SFR} \rangle$ for the ALN, ST1L, ST2L, and ST3L subsamples which have coverage of Ly β and the optical nebular emission lines. The shaded region indicates the 95% confidence interval on the predicted relationship between log U and log[$\Sigma_{\rm SFR}/M_{\odot}$ yr $^{-1}$ kpc $^{-2}$] given in Equation (17), normalized to pass through the point ($\langle \Sigma_{\rm SFR} \rangle_0 \langle \log U \rangle_0$) = (0.5 M_{\odot} yr $^{-1}$ kpc $^{-2}$, -3.0).

This stochasticity may be responsible for much of the scatter between $W_{\lambda}(Ly\alpha)$ and other galaxy properties noted in previous studies. Examples of this scatter are shown in Figure 23, which in some cases only becomes apparent when binning galaxies by properties independent of those on the abscissa and ordinate. For instance, the top two panels show the relationship between $\langle W_{\lambda}(Ly\alpha)\rangle$ and $\langle E(B-V)_{cont}\rangle$, including subsamples that were not constructed in bins of either $W_{\lambda}(Ly\alpha)$ or $E(B - V)_{cont}$ (i.e., the ST and sST subsamples). Similarly, the bottom two panels show the relationship between $\langle W_{\lambda}(Ly\alpha)\rangle$ and $\langle \Sigma_{SFR}\rangle$, including those subsamples not constructed in bins of either $W_{\lambda}(Ly\alpha)$ or Σ_{SFR} (i.e., the sST subsamples). These results suggest that the spread in $W_{\lambda}(Ly\alpha)$ at a fixed $E(B-V)_{cont}$, log U, or Σ_{SFR} may in part be driven by changes in H I/metal covering fraction, as demonstrated by the color-coding of the points in Figure 23. For instance, subsamples WT1LN and WT3LN have a relatively small separation in both $\langle \log U \rangle$ and $\langle \Sigma_{\rm SFR} \rangle$, yet they contain galaxies at the extreme ends of the $W_{\lambda}(Ly\alpha)$ distribution. In this case, the difference in $\langle W_{\lambda}(Ly\alpha)\rangle$ between the two samples is likely due to changes in gas covering fraction.

It is worth noting that several of the correlations investigated here are not expected to be monotonic, such as that between $W_{\lambda}(\mathrm{Ly}\alpha)$ and $f_{\mathrm{cov}}(\mathrm{H\,I})$, and between $W_{\lambda}(\mathrm{Ly}\alpha)$ and other parameters that influence $f_{\mathrm{cov}}(\mathrm{H\,I})$ (e.g., Σ_{SFR} , Σ_{SSFR}), for galaxies with lower covering fractions. A low covering fraction implies a significant escape of LyC photons that will result in a corresponding reduction in H I recombination line (e.g., Ly α , H α , H β , etc.) strengths. If $f_{\mathrm{esc}}^{\mathrm{spec}}(\mathrm{Ly}\alpha) = f_{\mathrm{esc}}(\mathrm{LyC})$, then one may expect $W_{\lambda}(\mathrm{Ly}\alpha) \propto f_{\mathrm{cov}}(\mathrm{H\,I})(1-f_{\mathrm{cov}}(\mathrm{H\,I}))$, where the first term reflects the fraction of LyC photons that photoionize hydrogen. While this function reaches a maximum value at $f_{\mathrm{cov}}(\mathrm{H\,I}) = 0.50$, additional scattering/attenuation of Ly α photons from moderate column density gas/dust—such that $f_{\mathrm{esc}}^{\mathrm{spec}}(\mathrm{Ly}\alpha) < f_{\mathrm{esc}}(\mathrm{LyC})$ —may result in a turnover of the

 $[\]overline{^{20}}$ The n_e derived in bins of $\Sigma_{\rm SFR}$ for the present sample are too uncertain to independently confirm a trend between $\Sigma_{\rm SFR}$ and n_e .

 $^{^{21}}$ Runco et al. (2021) find a similar trend between log U and $\Sigma_{\rm SFR}$ for MOSDEF galaxies, which form a superset of the galaxies considered here.

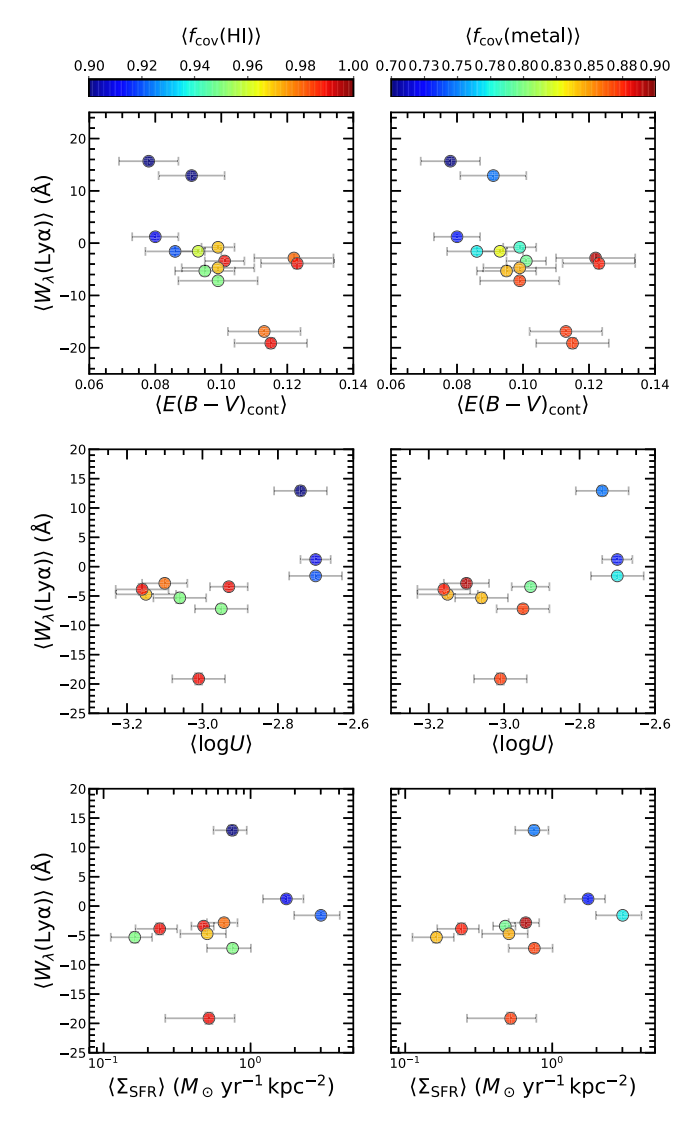


Figure 23. $\langle W_{\lambda}(\text{Ly}\alpha) \rangle$ vs. $\langle E(B-V)_{\text{cont}} \rangle$ (top), $\langle \log U \rangle$ (middle), and $\langle \Sigma_{\text{SFR}} \rangle$ (bottom), where the points have been color-coded by $\langle f_{\text{cov}}(\text{H I}) \rangle$ (left column) and $\langle f_{\text{cov}}(\text{metal}) \rangle$ (right column). The top panels only include subsamples with coverage of Ly β (required for a robust inference of $f_{\text{cov}}(\text{H I})$), and the middle and bottom panels only include subsamples with complete coverage of the optical nebular emission lines and Ly β .

function at higher $f_{\rm cov}({\rm H\,I})$. On the other hand, if $f_{\rm esc}^{\rm spec}$ (Ly α) $> f_{\rm esc}$ (LyC) (e.g., Dijkstra et al. 2016; Izotov et al. 2021)—as might be expected if a significant fraction of the Ly α flux observed within the spectroscopic aperture has resonantly scattered through many mean free paths (e.g., Figure 16)—then the turnover in the relation between $W_{\lambda}({\rm Ly}\alpha)$ and $f_{\rm cov}({\rm H\,I})$ may occur at lower $f_{\rm cov}({\rm H\,I})$. The nonmonotonic dependence of $W_{\lambda}({\rm Ly}\alpha)$ on $f_{\rm cov}({\rm H\,I})$ and variations in the turnover of this function from galaxy to galaxy would naturally contribute additional scatter in the relations between $W_{\lambda}({\rm Ly}\alpha)$ and other properties that correlate with $f_{\rm cov}({\rm H\,I})$.

4.5. Implications for LyC Escape at High Redshift

While our analysis has focused primarily on the production and escape of Ly α , it has obvious implications for LyC production and escape as well. The small variation in $\langle \xi_{\rm ion} \rangle$ with $\langle W_{\lambda}({\rm Ly}\alpha) \rangle$ (Section 4.2) implies a narrow range of ionizing photon production efficiencies across the sample. The variation in $W_{\lambda}({\rm Ly}\alpha)$ is most directly explained by the covering

fraction of H I (Section 4.2). From a physical standpoint, the low column density and ionized channels that facilitate the escape of Ly\$\alpha\$ provide avenues for LyC leakage. This scenario is supported empirically by the strong connection between $W_{\lambda}^{\rm em}({\rm Ly}\alpha)$ and the ionizing-to-nonionizing flux density ratio measured for $z \sim 3$ star-forming galaxies (Steidel et al. 2018), as well as correlations between $f_{\rm esc}^{\rm spec}$ (Ly\$\alpha\$) and $1 - f_{\rm cov}({\rm H\,I})$ (Reddy et al. 2016b; Gazagnes et al. 2020; see also Section 4.2) and between $f_{\rm esc}({\rm LyC})$ and $1 - f_{\rm cov}({\rm H\,I})$ (Steidel et al. 2018; Gazagnes et al. 2020) at both low and high redshift. 22

The variation in $f_{cov}(H I)$ alone is sufficient to account for the range of $W_{\lambda}(Ly\alpha)$ measured in our sample (Section 4.2). However, there is evidence that the hardness of the ionizing radiation field may play a more important role in the escape of Ly α and LyC radiation at higher redshifts ($z \gtrsim 4$) and for galaxies with fainter continuum luminosities and stronger Ly α emission (e.g., Trainor et al. 2016; Maseda et al. 2020). For instance, Pahl et al. (2020) report higher C IV P Cygni emission and Ly α equivalent width for $z \sim 5$ galaxies compared to lower-redshift galaxies at a fixed interstellar absorption-line equivalent width, suggestive of a harder ionizing spectrum on average for the former. Similarly, Atek et al. (submitted) suggest an evolution of higher ξ_{ion} with redshift for galaxies of similar mass based on a compilation of ξ_{ion} measurements at different redshifts. The strong correlation between ξ_{ion} and the equivalent widths of optical nebular emission lines (e.g., Chevallard et al. 2018; Tang et al. 2019; Reddy et al. 2018b; Atek et al., submitted) and the evolution toward higher equivalent widths with redshift at a fixed stellar mass (e.g., Fumagalli et al. 2012; Sobral et al. 2014; Khostovan et al. 2016; Faisst et al. 2016; Reddy et al. 2018b) imply an increase in the average hardness of the ionizing spectrum with redshift.

This increase in $\xi_{\rm ion}$ with redshift (e.g., for galaxies of a fixed mass) may also be accompanied by a decrease in the gas covering fraction. The well-studied size evolution of galaxies (e.g., Ribeiro et al. 2016; Allen et al. 2017) points to more compact sizes with redshift at a fixed stellar mass. This size evolution and the increase in SFR with redshift at a fixed stellar mass (e.g., Noeske et al. 2007; Whitaker et al. 2014; Schreiber et al. 2015) together imply a more compact configuration of star formation (i.e., higher $\Sigma_{\rm SFR}$) at higher redshifts that may favor the formation of low column density and/or ionized channels through which Ly α and LyC photons can escape.

Regardless of these evolutionary trends that may favor the escape of ionizing radiation, it is worth noting that the SPSneb modeling described in Section 3.1 implies that even *typical* star-forming galaxies at $z \sim 2$ are quite metal-poor in terms of their stellar abundances, 5%-10% of solar. If the escape of LyC radiation at higher redshifts ($z \gtrsim 3$) is aided by an increase in $\xi_{\rm ion}$, then it would ostensibly point to even younger ($\lesssim 10^7$ yr) or more metal-deficient ($Z_* \lesssim 0.05~Z_\odot$) stellar populations at these redshifts. However, for the 100bin SPSneb model with an age of 10^7 yr, $\log[\xi_{\rm ion}/s^{-1}/{\rm erg~s^{-1}~Hz^{-1}}] = 25.58$ and 25.66 for Z = 0.001 and Z = 0.0001 (i.e., $Z_*/Z_\odot = 0.07$ and 0.007), respectively, implying a relatively modest change of $\Delta \log[\xi_{\rm ion}/s^{-1}/{\rm erg~s^{-1}~Hz^{-1}}] \approx 0.08$ dex. The same numbers for the 300bin SPSneb model are $\log[\xi_{\rm ion}/s^{-1}/s^{-1}]$

²² Note that $f_{\rm cov}({\rm H~I})$ derived in this work is based on the residual flux under the Lyβ line, which is optically thick for gas with column densities that are $\simeq 3$ orders of magnitude lower than the column densities required for significant opacity ($\tau > 1$) in the LyC, i.e., $\log[N({\rm H~I})/{\rm cm}^{-2}] \simeq 14.2$ vs. $\log[N({\rm H~I})/{\rm cm}^{-2}] \simeq 17.2$.

erg s⁻¹ Hz⁻¹] = 25.65 and 25.71, again implying a modest change of $\Delta \log[\xi_{\rm ion}/{\rm s}^{-1}/{\rm erg~s}^{-1}$ Hz⁻¹] ≈ 0.06 .

Thus, it appears that changes in stellar metallicity alone are insufficient to cause significant increases in ξ_{ion} relative to the values found for typical star-forming galaxies at $z \sim 2$. The analysis described in Section 4.3.2 suggests that Σ_{SFR} and, in particular, $\Sigma_{\rm sSFR}$ may have more influence on LyC escape than the actual properties of the massive stars (e.g., stellar metallicity and age). Alternatively, strong bursts of star formation can both temporarily elevate ξ_{ion} (e.g., Emami et al. 2019, 2020; Nanayakkara et al. 2020) and reduce the covering fraction. Additionally, a harder ionizing spectrum than that predicted by the BPASS models at a fixed metallicity may allow for significant production (and escape) of LyC radiation without the need for invoking extremely metal-poor stellar populations. Further insight into the relevant factors for LyC escape may be achieved by extending the joint FUV and optical spectral modeling discussed here to galaxies with stronger Ly α emission and/or at higher redshifts, where at least most of the salient measurements are still possible, particularly at $2.7 \lesssim z \lesssim 4.0$, where the IGM is still relatively transparent and the LyC region is accessible using ground-based facilities.

5. Conclusions

We used spectral fitting and photoionization modeling of typical star-forming galaxies at redshifts $1.85 \le z \le 3.49$ to deduce several important characteristics of the massive stellar populations, as well as neutral and ionized ISM, and explore how the emergent Ly α line luminosity varies with these characteristics. The sample consists of 136 galaxies with deep FUV and optical spectra obtained with the Keck/LRIS and MOSFIRE spectrographs, respectively. The galaxies were binned according to $W_{\lambda}(Ly\alpha)$, Σ_{SFR} , and Σ_{sSFR} , and composite FUV and optical spectra were constructed for these bins. SPS model fits to the composite FUV spectra were used to infer stellar metallicity, age, and continuum reddening of the massive stars. Simultaneous fits to the interstellar HI absorption lines including Ly α and Ly β were used to infer line-ofsight reddening, column density, and gas covering fraction. Photoionization modeling of the composite optical spectra of the same sets of galaxies was used to infer the nebular reddening, gas-phase oxygen abundance, and ionization parameter. The joint FUV and optical spectral modeling is also used to distinguish between single and binary stellar evolution models. Section 3.4 summarizes most of the findings from the spectral fitting, including confirmation of several previously found (anti)correlations, such as those between $W_{\lambda}(\mathrm{Ly}\alpha)$ and $E(B-V)_{\mathrm{cont}}$ and those between $W_{\lambda}(\mathrm{Ly}\alpha)$ and age. Here, we summarize the key new results from our analysis:

1. Based on a comparison of the inferred He II nebular emission from the FUV composite spectra and the predictions from photoionization modeling, we find that the galaxies in our sample are uniformly consistent with stellar population models that include the effects of stellar binarity, independent of $W_{\lambda}(\text{Ly}\alpha)$ (Section 3.2.4, Figure 9). Furthermore, we find little variation in the stellar and nebular metallicity with $W_{\lambda}(\text{Ly}\alpha)$ over the dynamic range probed by our sample, with $\langle Z_* \rangle \simeq 0.08$ Z_{\odot} (Section 3.1.3, Figure 5) and $\langle Z_{\text{neb}} \rangle \simeq 0.40$ Z_{\odot} (Section 3.2.5, Figure 10, Appendix B). The offset in stellar and nebular metallicity implies that the stars and

- gas have $(O/Fe) \simeq 5 \times (O/Fe)_{\odot}$ irrespective of $W_{\lambda}(Ly\alpha)$, consistent with primary enrichment from Type II (corecollapse) SNe (Section 3.4). This conclusion is corroborated by the spectrally derived ages that vary from $\lesssim 100 \, \text{Myr}$ for galaxies with net positive $\langle W_{\lambda}(Ly\alpha) \rangle$ to $\simeq 300 \, \text{Myr}$ for those with net negative $\langle W_{\lambda}(Ly\alpha) \rangle$ (Section 3.1.3), implying that the galaxies are observed prior to the onset of significant Fe enrichment from Type Ia SNe.
- 2. The preference for binary stellar evolution models, the absence of any significant correlation between $\langle Z_* \rangle$ and $\langle W_{\lambda}(Ly\alpha)\rangle$, and the modest anticorrelation between $\langle \log[\mathrm{Age/Myr}] \rangle$ and $\langle W_{\lambda}(\mathrm{Ly}\alpha) \rangle$ together imply a relatively narrow range of ionizing spectral shapes ($\langle \log[\xi_{ion}/s^{-1}/s] \rangle$ erg s⁻¹ Hz⁻¹] $\rangle \simeq 25.30 - 25.40$; Section 4.2, Figure 15) that alone cannot account for the variation in $W_{\lambda}(Ly\alpha)$ observed within the sample. On the other hand, modeling of the Lyman series absorption lines and the depths of saturated low-ionization interstellar absorption lines suggests HI and metal-bearing gas covering fractions that are correlated with $W_{\lambda}(Ly\alpha)$. The covering fractions vary from $\langle f_{cov}(H I) \rangle \simeq 0.90$ and $\langle f_{cov}(metal) \rangle \simeq 0.75$ for galaxies with the highest $\langle W_{\lambda}({\rm Ly}\alpha) \rangle$ to $\langle f_{\rm cov}({\rm H~I}) \rangle \simeq 1.00$ and $\langle f_{\rm cov}({\rm metal}) \rangle \simeq 0.92$ for galaxies with the lowest $\langle W_{\lambda}(Ly\alpha)\rangle$ (Section 3.3.2, Figures 11 and 13).
- 3. These inferred covering fractions are sufficient to account for the variation in $W_{\lambda}(Ly\alpha)$ observed within the sample (Section 4.2). Thus, the gas covering fraction plays a more important role in modulating $W_{\lambda}(Ly\alpha)$ than the ionizing stellar spectrum for galaxies in our sample. Furthermore, we find that the fraction of Ly α photons that escapes along the line of sight, $\langle f_{\rm esc}^{\rm spec}({\rm Ly}\alpha)\rangle$, correlates with $1 - \langle f_{cov}(HI) \rangle$, suggesting that the majority of Ly α photons in down-the-barrel observations of galaxies escape through low column density or ionized channels in the ISM (Section 4.2, Figure 16). The dependence of $W_{\lambda}(Ly\alpha)$ on $f_{cov}(HI)$ implies that $Ly\alpha$ visibility may be a highly stochastic function of viewing angle, consequently contributing to the scatter between $W_{\lambda}(Ly\alpha)$ and several other galaxy properties, such as $E(B-V)_{\rm cont}$, log U, and $\Sigma_{\rm SFR}$ (Section 4.4, Figure 23).
- 4. The apparent large scatter in $\langle f_{\text{cov}} \rangle$ at a fixed ξ_{ion} (Figure 17) implies that there are factors other than the shape of ionizing spectrum that affect f_{cov} . In particular, we investigate the effects of compact star formation and galaxy potential on gas covering fraction. We do not observe a clear monotonic relationship between $\langle f_{\rm cov}({\rm H\,I}) \rangle$ and $\langle \Sigma_{\rm SFR} \rangle$, and we only find a significant difference in $\langle f_{cov}(metal) \rangle$ between galaxies in the lower and upper third of the Σ_{SFR} distribution (Section 4.3.2, Figure 18). On the other hand, both $\langle f_{cov}(HI) \rangle$ and $\langle f_{\rm cov}({\rm metal}) \rangle$ are significantly lower in galaxies with higher $\Sigma_{\rm sSFR}$. Similarly, the difference in $\langle f_{\rm esc}^{\rm spec}({\rm Ly}\alpha) \rangle$ for galaxies, in the last state of the state of th galaxies in the lower and upper thirds of the $\Sigma_{\rm sSFR}$ distribution is larger than that of galaxies in the lower and upper thirds of the $\Sigma_{\rm SFR}$ distribution (Figure 21). These results suggest that the galaxy potential may play an important role in the escape of Ly α (and LyC) photons: compact star formation in a low potential may yield conditions (i.e., lower gas covering fractions) that aid the escape of these photons. Furthermore, we suggest that the correlation between ionization parameter and Σ_{SFR} may

be connected to the superlinear dependence of the latter on electron density, or interstellar pressure (Section 4.3.3, Figure 22).

This paper presents a comprehensive analysis of the composite FUV and optical spectra of a sample of typical star-forming galaxies at $z \sim 2$, focusing on how Ly α escape depends on key properties of the massive stars, and the neutral and ionized ISM. To conclude, we suggest a few investigations to further elucidate the mechanisms of Ly α and LyC escape in high-redshift galaxies. As noted in Section 3.3, direct inferences of HI gas covering fractions at high redshift are limited to ensembles of galaxies given the large line-of-sight opacity variations of the Ly α forest. Nonetheless, several of the correlations presented here and the dependence of the scatter in these correlations on other galaxy properties (e.g., such as those between $W_{\lambda}(Ly\alpha)$, Z_* , and spectrally derived ages; between $W_{\lambda}(Ly\alpha)$, Z_{neb} , and $\log U$; between $W_{\lambda}(Ly\alpha)$ and ξ_{ion} ; and between $W_{\lambda}(Ly\alpha)$, Σ_{SFR} , and $\Sigma_{\rm sSFR}$) may be further investigated on an individual galaxy basis provided sufficiently high S/N FUV and optical spectra (e.g., Topping et al. 2020b; Du et al. 2021). Additionally, several ongoing ALMA programs to constrain molecular gas masses can be used to probe gas surface densities, examine their connection to interstellar pressure, and evaluate them in the context of the high electron densities and high ionization parameters inferred for highredshift galaxies. MOSDEF-LRIS and the ancillary HST imaging also enable investigations of the correlation between gas covering fraction and galaxy inclination and the subsequent effect on Ly α and LyC escape. The joint FUV and optical spectral modeling presented here can be extended to galaxies at slightly higher average redshifts $(2.7 \le z \le 4.0)$ for which the transparency of the intervening IGM and Earth's atmosphere allow the modeling of the higher-order Lyman series lines and LyC emission to be probed with ground-based observatories. Upcoming observations with the James Webb Space Telescope will give access to the longer-wavelength optical lines (e.g., $H\alpha$, [N II], [S II]) for galaxies at these redshifts, aiding in photoionization modeling of their ionized ISM. Finally, ongoing optical IFU observations with the Keck Cosmic Web Imager (KCWI) will enable studies of the resonantly scattered Ly α emission (and LyC emission) in individual galaxies, likely revealing the diversity of avenues through which Ly α and LyC emission escapes galaxies.

We acknowledge support from NSF AAG grants AST1312780, 1312547, 1312764, and 1313171; grant AR13907 from the Space Telescope Science Institute; and grant NNX16AF54G from the NASA ADAP program. This work made use of v2.2.1 of the Binary Population and Spectral Synthesis (BPASS) models, as described in Eldridge et al. (2017) and Stanway & Eldridge (2018), and v17.02 of the Cloudy radiative transfer code (Ferland et al. 2017). We wish to extend special thanks to those of Hawaiian ancestry on whose sacred mountain we are privileged to be guests. Without their generous hospitality, most of the observations presented herein would not have been possible.

Appendix A Constraints on the Continuum Attenuation Curve

As noted in Section 3.1.1, the composite FUV spectra were initially fit with the SPSneb models assuming three dust attenuation curves. For the bulk of our analysis, however, we choose to present the results with the SMC extinction curve, as

this curve yields SFRs from the spectral fitting, SFR(SED), most consistent with those derived based on $H\alpha$, SFR($H\alpha$). The calculations of SFR($H\alpha$) for individual galaxies and composites (subsamples) are presented in Section 4.3.1. For individual galaxies, SFR(SED) was inferred from broadband SED modeling (Section 2.3.3). For an ensemble of galaxies, $\langle SFR(SED) \rangle$ was determined by the normalization of the SPSneb model that best fits the composite FUV spectrum (Section 3.1.1) and is similar to that obtained by averaging the SFR(SED) of individual galaxies contributing to the composite. For the purposes of comparing SFR(SED) and SFR($H\alpha$), we highlight a few additional salient details below.

Binary stellar evolution or a higher-mass cutoff of the IMF results in a larger ionizing photon luminosity, $Q(H^0)$, and hence larger $L(H\alpha)$, per unit SFR. The factors used to convert the dust-corrected $L({\rm H}\alpha)$ to SFR(H α) are [2.12, 1.52, 2.69, 1.96] \times 10⁻⁴² M_{\odot} yr⁻¹ erg⁻¹ s for the Z_* = 0.001 100bin, 300bin, 100sin, and 300sin SPSneb models, respectively, and are essentially constant as a function of age beyond 10⁷ yr. On the other hand, SFR(SED) is primarily determined by the nonionizing UV luminosity and therefore is not particularly sensitive to binary stellar evolution or the high-mass cutoff of the IMF (Theios et al. 2019). Similarly, the variations in SFR $(H\alpha)$ and SFR(SED) with Z_* are generally small over the range of relevant Z_* —e.g., \approx 7% variations in SFR(H α) for the $Z_* = 0.001$ versus $Z_* = 0.002$ models—compared to the variations induced by changing the high-mass cutoff of the IMF or including the effects of binary stellar evolution. As noted in Section 2.3.3, we assumed the $Z_* = 0.001$ BPASS models when fitting the broadband photometry of individual galaxies, while for the galaxy ensembles Z_* is the best-fit value obtained when fitting the SPSneb models to the composite FUV spectra (Section 3.1.1).

Finally, we note that varying the dust attenuation curve can have a large effect on SFR(SED), which can change by a factor of \simeq 2–4 depending on the colors of the object (or ensemble). At a fixed observed FUV color, curves with a steep dependence of attenuation on wavelength yield lower reddening, and hence lower SFR(SED), than shallower curves (e.g., Pettini et al. 1998; Reddy et al. 2012b). Consequently, SFR(SED) computed with the SMC curve are systematically lower than those computed with the Calzetti et al. (2000) curve, while those computed with the Reddy et al. (2015) curve lie between the SMC and Calzetti et al. (2000) determinations.

Figure 24 shows comparisons between SFR(H α) and SFR (SED) for individual objects and composites of galaxies having complete coverage of the optical nebular emission lines. Though only individual objects with significant H α and H β detections are shown in the figure, for a fixed attenuation curve their $\langle SFR(H\alpha) \rangle$ and $\langle SFR(SED) \rangle$ generally lie within 20% of the mean values obtained for the composites that include galaxies irrespective of significant individual detections of H α and H β .

Having computed $\langle SFR(H\alpha) \rangle$ and $\langle SFR(SED) \rangle$ using the self-consistent modeling described above, we find that the two agree within a factor of $\simeq 2$ only if we assume the SMC extinction curve for the reddening of the stellar continuum. In contrast, the Calzetti et al. (2000) curve yields $\langle SFR(SED) \rangle$ that is systematically larger than $\langle SFR(H\alpha) \rangle$ by 0.4–0.5 dex in $\log[SFR/M_{\odot} \text{ yr}^{-1}]$. These conclusions hold irrespective of the effects of binary stellar evolution and variations in the high-

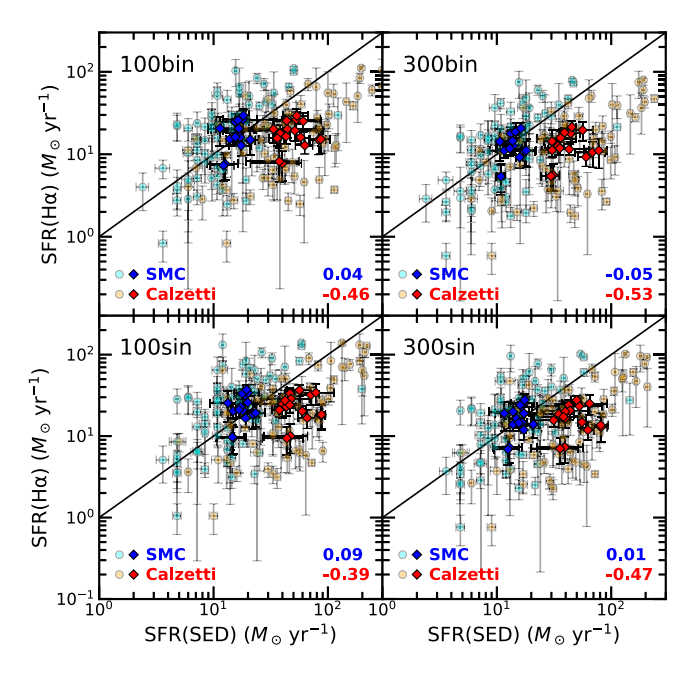


Figure 24. Comparison of SFR(H α) and SFR(SED) for individual objects with significant detections of H α and H β (circles) and for the 16 composites with complete coverage of the optical nebular emission lines (diamonds). SFRs derived assuming the SMC curve are denoted by the cyan and blue symbols; those derived assuming the Calzetti et al. (2000) curve are denoted by the orange and red symbols. In all cases, SFR(H α) is calculated by dust-correcting $L(H\alpha)$ using the Cardelli et al. (1989) extinction curve. The line indicates the one-to-one relation between SFR(H α) and SFR(SED). The panels show the comparisons for the four flavors of BPASS models discussed in Section 2.3.3. The average offsets (differences) in dex between log[SFR(H α)/ M_{\odot} yr⁻¹] and log[SFR(SED)/ M_{\odot} yr⁻¹] for the 16 composites are indicated for the SMC and Calzetti et al. (2000) cases in the lower right corner of each panel.

mass cutoff of the IMF between 100 and $300 M_{\odot}$, as indicated in the four panels of Figure 24.²³

The preference for the SMC extinction curve in describing the reddening of the stellar continuum is not unique to this analysis. Earlier studies suggested that young and low-mass galaxies at $z \gtrsim 2$ may follow an attenuation curve that is steeper than the commonly assumed Calzetti et al. (2000) curve (e.g., Baker et al. 2001; Reddy et al. 2006; Siana et al. 2008, 2009; Reddy et al. 2010, 2012a; Lee et al. 2012; Oesch et al. 2013; De Barros et al. 2016). More recently, Reddy et al. (2018a) found that the relationship between dust attenuation—parameterized by the ratio of the infrared and unobscured FUV luminosities (i.e., IRX)—and FUV slope, β , is best reproduced by the SMC extinction curve for subsolar-metallicity stellar populations at $z \sim 2$ (see also Theorem et al. 2019). ALMA dust continuum and [CII] surveys of modestly reddened $z \gtrsim 2$ galaxies also point to a steep (SMC-like) dust curve (Bouwens et al. 2016a; Fudamoto et al. 2017, 2020). Such a steep curve is also favored by observations of local analogs of high-redshift galaxies (Salim et al. 2018).

The requirement of an SMC-like dust curve for obtaining consistent values of $\langle SFR(H\alpha) \rangle$ and $\langle SFR(SED) \rangle$ does not preclude the possibility that some galaxies in our sample are better described by shallower dust curves. Specifically, Shivaei et al. (2020) find that MOSDEF galaxies in the upper half of the

stellar mass and gas-phase abundance distributions have a dust curve similar in shape to the Calzetti et al. (2000) curve, and shallower than the curve for lower-mass (and lower gas-phase abundance) MOSDEF galaxies. This conclusion corroborates previous findings of a mass dependence of the shape of the dust curve (e.g., Pannella et al. 2009; Reddy et al. 2010; Bouwens et al. 2016a). In the present context, we simply note that the comparison between $\langle SFR(H\alpha) \rangle$ and $\langle SFR(SED) \rangle$ implies an attenuation curve that is steeper than the Calzetti et al. (2000) curve for the subsamples formed by the parameters listed in Table 1.

Appendix B Direct Electron-temperature-based Metallicities

The detection of the intercombination lines O III] $\lambda\lambda$ 1661, 1666 in the composite FUV spectra provides an independent measurement of the oxygen abundance via the "direct" metallicity method. The average O III] $\lambda\lambda$ 1661, 1666 luminosity was computed by directly integrating over the line pair in the composite FUV spectrum for the ALN subsample—the only subsample with complete coverage of the optical nebular emission lines where O III] is significantly detected—after subtracting a locally determined continuum. The O III] luminosity was corrected for dust obscuration assuming $\langle E(B-V)_{\text{neb}} \rangle$ and the Cardelli et al. (1989) extinction curve (Table 5). The ratio of the dust-corrected O III] $\lambda\lambda$ 1661, 1666 luminosity to that of [O III] λ 5008 yields an estimate of the electron temperature of the [O III]-emitting region, $T_e(O III) = 13400 \pm 1100 \text{ K}$ (e.g., Villar-Martín et al. 2004). Using the relationship between the temperatures of the [O III]- and [O II]-emitting regions (i.e., the " $T_2 - T_3$ " relation) given in Campbell et al. (1986) and the abundance relations provided in Izotov et al. (2006), we derive an O abundance of $12 + \log (O/H)_{dir} \simeq 8.01 \pm 0.10$, provided that O is predominantly in the singly or doubly ionized stages. Note that the abundances derived using the collisionally excited lines are most sensitive to the highest-temperature regions and will thus underestimate the abundances relative to those derived from nebular recombination lines. Based on measurements of collisionally excited and recombination lines in star-forming knots of local galaxies (Esteban et al. 2014) and H II regions (Blanc et al. 2015), the typical offset in abundances derived from the two sets of lines is ≈ 0.24 dex (see also discussion in Steidel et al. 2016). Adding 0.24 dex to the direct-method abundance yields $\langle 12 + \log(O/H) \rangle = 8.26 \pm 0.10$, or $\langle Z_{neb} \rangle = 0.37 \pm 0.09$, in excellent agreement with that obtained from the photoionization modeling. Note that there may be a potentially large (and unaccounted-for) systematic error in the extrapolation of the nebular dust attenuation curve to FUV wavelengths and the resulting dust corrections to OIII]. However, the agreement between the direct-method abundance and those obtained from the photoionization modeling suggests that the dust corrections inferred from the Cardelli et al. (1989) curve are reasonable.

Appendix C C III] $\lambda\lambda$ 1907, 1909

As noted in Section 3.2.5, additional evidence for the higher ionization parameter of galaxies with stronger Ly α emission comes from C III] $\lambda\lambda1907$, 1909, which is frequently used as a probe of the ionizing radiation field (e.g., Garnett et al. 1995; Shapley et al. 2003; Erb et al. 2010; Stark et al. 2015; Vanzella et al. 2016; Berg et al. 2016; Senchyna et al. 2017; Maseda et al. 2017; Schaerer et al. 2018; Nakajima et al. 2018b;

²³ An upward correction to $\langle SFR(H\alpha) \rangle$ to account for the fraction of escaping ionizing photons (as inferred from the clumpy ISM model; Sections 3.3.1 and 3.3.2) does not significantly affect the SFR comparisons discussed here. Such corrected $\langle SFR(H\alpha) \rangle$ are considered in Section 4.3.

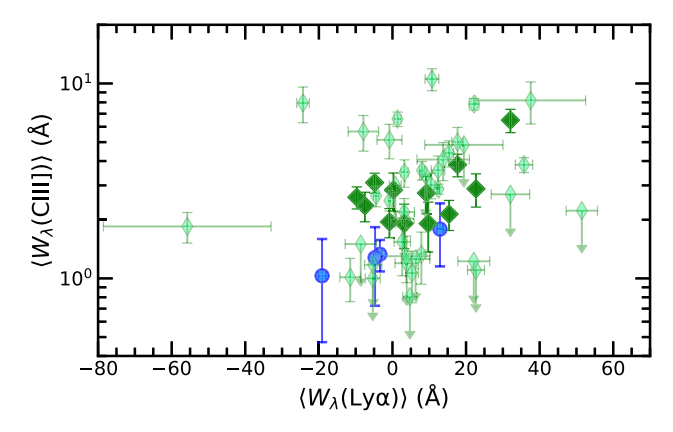


Figure 25. Variation of $\langle W_{\lambda}(\text{C III}] \rangle$ with $\langle W_{\lambda}(\text{Ly}\alpha) \rangle$. Values obtained for the ALN, WT1LN, WT2LN, and WT3LN subsamples which have complete coverage of the optical nebular emission lines are indicated by the blue filled circles. For comparison, also shown are the individual measurements (small lightgreen diamonds) of EELGs from Du et al. (2020), which lie at similar redshifts $(z \sim 2)$ to MOSDEF-LRIS galaxies. For clarity, one of the EELGs from Du et al. (2020) that has $W_{\lambda}(\text{Ly}\alpha) = 132 \pm 11$ Å and $W_{\lambda}(\text{C III}]) = 13.2 \pm 0.8$ Å is not shown. Composite measurements of the EELGs are indicated by the large darkgreen diamonds.

Hutchison et al. 2019; Du et al. 2020; Mainali et al. 2020; Feltre et al. 2020; Ravindranath et al. 2020; Tang et al. 2021). The relationship between $W_{\lambda}(Ly\alpha)$ and $W_{\lambda}(CIII)$ for subsamples ALN and WT with complete coverage of the optical nebular emission lines—and hence complete coverage of C III] in the composite FUV spectra given the redshift distribution of the galaxies in these subsamples (z < 2.6)—is shown in Figure 25. For context, the figure also includes measurements for extreme emission-line galaxies (EELGs) from Du et al. (2020), where $W_{\lambda}(Ly\alpha)$ was measured using the same methodology adopted here. The uncertainties on $W_{\lambda}(C III)$ for the aforementioned composites prevent us from independently confirming a trend between $\langle W_{\lambda}(C \text{ III}] \rangle$ and $\langle W_{\lambda}(Ly\alpha) \rangle$. However, these measurements are consistent with those obtained from previous studies (e.g., Shapley et al. 2003; Stark et al. 2014, 2015; Nakajima et al. 2018a; Ravindranath et al. 2020; Feltre et al. 2020) that find a significant correlation between $W_{\lambda}(C \text{ III}]$) and $W_{\lambda}(Ly\alpha)$.

In addition to the shape of the ionizing spectrum, $W_{\lambda}(\text{C III}]$) is also sensitive to the carbon abundance (Garnett et al. 1995). To quantify the extent to which variations in $W_{\lambda}(\text{C III}]$) may be driven by changes in C abundance, we compared the C3O3 ratios (defined in Table 4) measured for the subsamples with the predictions of the best-fit photoionization models (Section 3.2) for a range of C/O.²⁴ Figure 26 shows the predicted C3O3 as a function of log W and C/O for $W_{\text{neb}} = 0.4 \ Z_{\odot}$, the typical nebular abundance indicated by the photoionization modeling presented in Section 3.2. These predictions can be compared with the C3O3 calculated for each subsample using the measurements in Table 5. The measured C3O3 for subsamples with complete coverage of the optical nebular emission lines are also shown in Figure 26, color-coded by the $W_{\lambda}(\text{Ly}\alpha)$ for those subsamples. In considering the sample as a whole (i.e.,

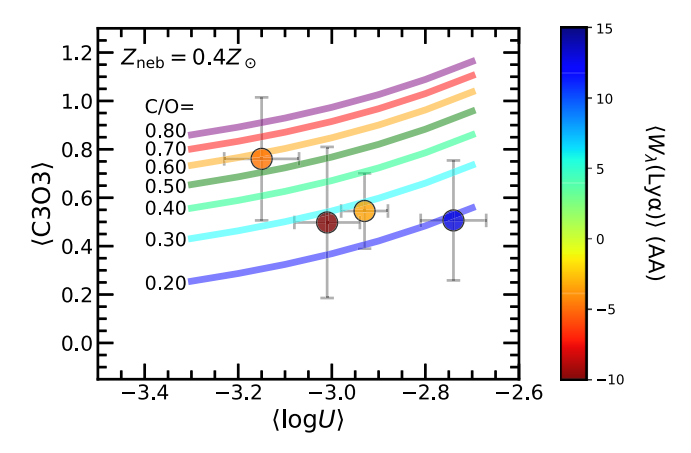


Figure 26. $\langle \text{C3O3} \rangle$ vs. $\langle \log U \rangle$ for the ALN, WT1LN, WT2LN, and WT3LN subsamples which have complete coverage of the optical nebular emission lines, color-coded by $\langle W_{\lambda}(\text{Ly}\alpha) \rangle$. Also shown are the photoionization model predictions for the relationships between C3O3 and $\log U$ for $Z_{\text{neb}} = 0.4~Z_{\odot}$ and different values of C/O.

subsample ALN), we find that the photoionization models discussed in Section 3.2 reproduce the measured C3O3 ratios if we assume $\log(C/O)=-0.46\pm0.13$, a value similar to that of local dwarf galaxy H II regions (Kobulnicky & Skillman 1998; Berg et al. 2019) of the same O abundance of $12+\log(O/H)\simeq 8.3$ ($Z_{\rm neb}\approx 0.4Z_{\odot}$). The inferred C/O in terms of the solar value ($\log{(C/O)_{\odot}}=-0.26$; Asplund et al. 2009) is $[C/O]=-0.20\pm0.13$. Note that this is similar to the inferred value of $[N/O]=\log(N/O)-\log{(N/O)_{\odot}}=-0.34\pm0.01$, where $\log(N/O)=-1.20\pm0.01$ (Section 3.2.1) and $\log{(N/O)_{\odot}}=-0.86$ (Asplund et al. 2009), and suggests a common nucleosynthetic origin for C and N.

The measurement uncertainties in C3O3 are not particularly constraining insofar as the implied $\log(C/O)$, and there does not appear to be any significant trend between $\log(C/O)$ and $\langle W_{\lambda}(\mathrm{Ly}\alpha) \rangle$. This result is perhaps not so surprising given the lack of any significant trend in O abundance (or gas-phase metallicity, Z_{neb}) with $\langle W_{\lambda}(\mathrm{Ly}\alpha) \rangle$ (Section 3.2.5; Figure 10). Consequently, the significant correlation between $\langle W_{\lambda}(\mathrm{C\,III\,I}] \rangle$ and $\langle W_{\lambda}(\mathrm{Ly}\alpha) \rangle$ (Figure 25) is likely driven by changes in the ionizing radiation field rather than by abundance variations (see also Jaskot & Ravindranath 2016; Nakajima et al. 2018b; Ravindranath et al. 2020).

Appendix D Correlations between $W_{\lambda}(\mathrm{Ly}\alpha)$ and R_e , SFR, and M. for Individual Galaxies

Figure 27 summarizes the correlations between $W_{\lambda}(\mathrm{Ly}\alpha)$ and R_e , SFR(H α), and M_* for individual galaxies in the sample. The data indicate a significant anticorrelation between $W_{\lambda}(\mathrm{Ly}\alpha)$ and R_e , with a probability of $p_{\mathrm{ind}} = 0.01$ that the two are uncorrelated based on a Spearman rank correlation test. The observation of compact ($\lesssim 1$ kpc) sizes for strong Ly α emitters has been noted in many previous studies and likely reflects the underlying correlations between $W_{\lambda}(\mathrm{Ly}\alpha)$ and luminosity/mass and between size and luminosity/mass (e.g., Shibuya et al. 2019 and references therein).

A Spearman test indicates a relatively high probability $(p_{\rm ind}=0.26)$ of a null correlation between $W_{\lambda}({\rm Ly}\alpha)$ and SFR $({\rm H}\alpha)$. Finally, the data indicate a significant anticorrelation between $W_{\lambda}({\rm Ly}\alpha)$ and M_* , with $p_{\rm ind}<0.01$ (right panel of Figure 27), a result that has been found (or suggested) by a

 $^{^{24}}$ As is the case with O abundances determined from collisionally excited O lines (Appendix B), C abundances derived from C III] $\lambda\lambda$ 1907, 1909 may underestimate those derived from the optical C recombination lines. However, in the present context, we are interested in the *relative* abundances derived for the different subsamples and are therefore not concerned with offsets in the absolute C abundance.

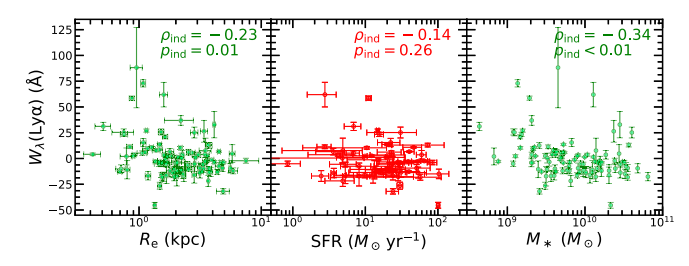


Figure 27. Variation in $W_{\lambda}(\mathrm{Ly}\alpha)$ with half-light radius R_e (left), SFR(H α) (middle), and M_* (right) for individual galaxies. SFR(H α) is shown only for those galaxies where H α and H β are both detected with S/N > 3. Each panel indicates the Spearman correlation coefficient and p-value for the displayed variables.

number of other studies (e.g., Gawiser et al. 2006; Pentericci et al. 2007; Finkelstein et al. 2007; Pentericci et al. 2009; Guaita et al. 2011; Jones et al. 2012; Hagen et al. 2014; Hathi et al. 2016; Du et al. 2018; Marchi et al. 2019).

The aforementioned correlations, particularly between $W_{\lambda}(Ly\alpha)$ and both size and stellar mass, have generally been interpreted to reflect the less evolved state of galaxies with stronger Ly α emission. This interpretation is supported by the apparent anticorrelation between $W_{\lambda}(Ly\alpha)$ and age, where the latter is inferred either from broadband SED fitting or from FUV spectral fitting (Section 3.1.3). However, the strong Ly α emission observed in some evolved high-redshift galaxies implies that the emergent Ly α emission is not solely related to galaxy youth and may also depend on the covering fraction of gas or dust (e.g., Pentericci et al. 2009), an inference that is supported by our findings (Sections 4.2.3). Our analysis also suggests that the galaxy potential may play an important role in gas covering fraction (Section 4.3), which, consequently, gives rise to an anticorrelation between $W_{\lambda}(Ly\alpha)$ and stellar mass (e.g., Kim et al. 2020).

ORCID iDs

Naveen A. Reddy https://orcid.org/0000-0001-9687-4973
Alice E. Shapley https://orcid.org/0000-0003-3509-4855
Charles C. Steidel https://orcid.org/0000-0002-4834-7260
Ryan L. Sanders https://orcid.org/0000-0003-4792-9119
Xinnan Du https://orcid.org/0000-0001-5554-5444
Alison L. Coil https://orcid.org/0000-0002-2583-5894
Sedona H. Price https://orcid.org/0000-0002-0108-4176
Irene Shivaei https://orcid.org/0000-0003-4702-7561

References

```
Alexandroff, R. M., Heckman, T. M., Borthakur, S., Overzier, R., &
  Leitherer, C. 2015, ApJ, 810, 104
Allen, R. J., Kacprzak, G. G., Glazebrook, K., et al. 2017, ApJL, 834, L11
Asplund, M., Grevesse, N., Sauval, A. J., & Scott, P. 2009, ARA&A, 47, 481
Atek, H., Kunth, D., Hayes, M., Östlin, G., & Mas-Hesse, J. M. 2008, A&A,
Atek, H., Kunth, D., Schaerer, D., et al. 2009, A&A, 506, L1
Atek, H., Kunth, D., Schaerer, D., et al. 2014, A&A, 561, A89
Azadi, M., Coil, A., Aird, J., et al. 2018, ApJ, 866, 63
Azadi, M., Coil, A. L., Aird, J., et al. 2017, ApJ, 835, 27
Bacon, R., Conseil, S., Mary, D., et al. 2017, A&A, 608, A1
Baker, A. J., Lutz, D., Genzel, R., Tacconi, L. J., & Lehnert, M. D. 2001,
      A, 372, L37
Baldwin, J. A., Phillips, M. M., & Terlevich, R. 1981, PASP, 93, 5
Battisti, A. J., Calzetti, D., & Chary, R. R. 2016, ApJ, 818, 13
Behrens, C., & Braun, H. 2014, A&A, 572, A74
Behrens, C., Pallottini, A., Ferrara, A., Gallerani, S., & Vallini, L. 2019,
   MNRAS, 486, 2197
```

```
Berg, D. A., Erb, D. K., Henry, R. B. C., Skillman, E. D., &
  McQuinn, K. B. W. 2019, ApJ, 874, 93
Berg, D. A., Skillman, E. D., Henry, R. B. C., Erb, D. K., & Carigi, L. 2016,
    ApJ, 827, 126
Berry, M., Gawiser, E., Guaita, L., et al. 2012, ApJ, 749, 4
Blanc, G. A., Kewley, L., Vogt, F. P. A., & Dopita, M. A. 2015, ApJ, 798, 99
Borthakur, S., Momjian, E., Heckman, T. M., et al. 2014, ApJ, 795, 98
Bouwens, R. J., Aravena, M., Decarli, R., et al. 2016a, ApJ, 833, 72
Bouwens, R. J., Smit, R., Labbé, I., et al. 2016b, ApJ, 831, 176
Brinchmann, J., Pettini, M., & Charlot, S. 2008, MNRAS, 385, 769
Calzetti, D., Armus, L., Bohlin, R. C., et al. 2000, ApJ, 533, 682
Calzetti, D., Kinney, A. L., & Storchi-Bergmann, T. 1994, ApJ, 429, 582
Campbell, A., Terlevich, R., & Melnick, J. 1986, MNRAS, 223, 811
Cardelli, J. A., Clayton, G. C., & Mathis, J. S. 1989, ApJ, 345, 245
Cen, R. 2020, ApJL, 889, L22
Chabrier, G. 2003, PASP, 115, 763
Chevallard, J., Charlot, S., Senchyna, P., et al. 2018, MNRAS, 479, 3264
Chisholm, J., Gazagnes, S., Schaerer, D., et al. 2018, A&A, 616, A30
Chisholm, J., Rigby, J. R., Bayliss, M., et al. 2019, ApJ, 882, 182
Coil, A. L., Aird, J., Reddy, N., et al. 2015, ApJ, 801, 35
Crowther, P. A., Caballero-Nieves, S. M., Bostroem, K. A., et al. 2016,
  MNRAS, 458, 624
Crowther, P. A., Prinja, R. K., Pettini, M., & Steidel, C. C. 2006, MNRAS,
Cullen, F., McLure, R. J., Dunlop, J. S., et al. 2019, MNRAS, 487, 2038
Cullen, F., McLure, R. J., Dunlop, J. S., et al. 2020, MNRAS, 495, 1501
Davies, R. L., Schreiber, N. M. F., Genzel, R., et al. 2021, ApJ, 909, 78
Dayal, P., Maselli, A., & Ferrara, A. 2011, MNRAS, 410, 830
De Barros, S., Reddy, N., & Shivaei, I. 2016, ApJ, 820, 96
Dijkstra, M., Gronke, M., & Venkatesan, A. 2016, ApJ, 828, 71
Dijkstra, M., Haiman, Z., & Spaans, M. 2006, ApJ, 649, 14
Du, X., Shapley, A. E., Reddy, N. A., et al. 2018, ApJ, 860, 75
Du, X., Shapley, A. E., Tang, M., et al. 2020, ApJ, 890, 65
Du, X., Shapley, A. E., Topping, M. W., et al. 2021, ApJ, 920, 95
Duval, F., Schaerer, D., Östlin, G., & Laursen, P. 2014, A&A, 562, A52
Eldridge, J. J., Stanway, E. R., Xiao, L., et al. 2017, PASA, 34, e058
Emami, N., Siana, B., Alavi, A., et al. 2020, ApJ, 895, 116
Emami, N., Siana, B., Weisz, D. R., et al. 2019, ApJ, 881, 71
Erb, D. K., Pettini, M., Shapley, A. E., et al. 2010, ApJ, 719, 1168
Erb, D. K., Pettini, M., Steidel, C. C., et al. 2016, ApJ, 830, 52
Esteban, C., García-Rojas, J., Carigi, L., et al. 2014, MNRAS, 443, 624
Faisst, A. L., Capak, P., Hsieh, B. C., et al. 2016, ApJ, 821, 122
Fanelli, M. N., O'Connell, R. W., & Thuan, T. X. 1988, ApJ, 334, 665
Feltre, A., Maseda, M. V., Bacon, R., et al. 2020, A&A, 641, A118
Ferland, G. J., Chatzikos, M., Guzmán, F., et al. 2017, RMxAA, 53, 385
Finkelstein, S. L., Cohen, S. H., Moustakas, J., et al. 2011, ApJ, 733, 117
Finkelstein, S. L., Rhoads, J. E., Malhotra, S., & Grogin, N. 2009, ApJ,
  691, 465
Finkelstein, S. L., Rhoads, J. E., Malhotra, S., Pirzkal, N., & Wang, J. 2007,
  ApJ, 660, 1023
Förster Schreiber, N. M., Genzel, R., Bouché, N., et al. 2009, ApJ, 706, 1364
Fudamoto, Y., Oesch, P. A., Faisst, A., et al. 2020, A&A, 643, A4
Fudamoto, Y., Oesch, P. A., Schinnerer, E., et al. 2017, MNRAS, 472, 483
Fumagalli, M., Patel, S. G., Franx, M., et al. 2012, ApJL, 757, L22
Garnett, D. R., Skillman, E. D., Dufour, R. J., et al. 1995, ApJ, 443, 64
Gawiser, E., van Dokkum, P. G., Gronwall, C., et al. 2006, ApJL, 642, L13
Gazagnes, S., Chisholm, J., Schaerer, D., et al. 2018, A&A, 616, A29
Gazagnes, S., Chisholm, J., Schaerer, D., Verhamme, A., & Izotov, Y. 2020,
    &A, 639, A85
Gnedin, N. Y., Kravtsov, A. V., & Chen, H.-W. 2008, ApJ, 672, 765
Gordon, K. D., Clayton, G. C., Misselt, K. A., Landolt, A. U., & Wolff, M. J.
   2003, ApJ, 594, 279
Grogin, N. A., Kocevski, D. D., Faber, S. M., et al. 2011, ApJS, 197, 35
Gronke, M., Bull, P., & Dijkstra, M. 2015, ApJ, 812, 123
Gronke, M., Dijkstra, M., McCourt, M., & Oh, S. P. 2016, ApJL, 833, L26
Guaita, L., Acquaviva, V., Padilla, N., et al. 2011, ApJ, 733, 114
Hagen, A., Ciardullo, R., Gronwall, C., et al. 2014, ApJ, 786, 59
Halliday, C., Daddi, E., Cimatti, A., et al. 2008, A&A, 479, 417
Harikane, Y., Laporte, N., Ellis, R. S., & Matsuoka, Y. 2020, ApJ, 902, 117
Hathi, N. P., Le Fèvre, O., Ilbert, O., et al. 2016, A&A, 588, A26
Hayes, M., Schaerer, D., Östlin, G., et al. 2011, ApJ, 730, 8
Heckman, T. M., Borthakur, S., Overzier, R., et al. 2011, ApJ, 730, 5
Henry, A., Scarlata, C., Martin, C. L., & Erb, D. 2015, ApJ, 809, 19
Hutchison, T. A., Papovich, C., Finkelstein, S. L., et al. 2019, ApJ, 879, 70
Hutter, A., Dayal, P., Partl, A. M., & Müller, V. 2014, MNRAS, 441, 2861
Inoue, A. K. 2001, AJ, 122, 1788
```

```
Izotov, Y. I., Stasińska, G., Meynet, G., Guseva, N. G., & Thuan, T. X. 2006,
Izotov, Y. I., Worseck, G., Schaerer, D., et al. 2021, MNRAS, 503, 1734
Jaskot, A. E., Dowd, T., Oey, M. S., Scarlata, C., & McKinney, J. 2019, ApJ,
   885.96
Jaskot, A. E., & Oey, M. S. 2013, ApJ, 766, 91
Jaskot, A. E., & Ravindranath, S. 2016, ApJ, 833, 136
Jeong, M.-S., Shapley, A. E., Sanders, R. L., et al. 2020, ApJL, 902, L16
Jiang, T., Malhotra, S., Yang, H., & Rhoads, J. E. 2019, ApJ, 872, 146
Jones, T., Stark, D. P., & Ellis, R. S. 2012, ApJ, 751, 51
Jones, T. A., Ellis, R. S., Schenker, M. A., & Stark, D. P. 2013, ApJ, 779, 52
Kakiichi, K., & Gronke, M. 2021, ApJ, 908, 30
Kashino, D., Silverman, J. D., Rodighiero, G., et al. 2013, ApJL, 777, L8
Kewley, L. J., & Dopita, M. A. 2002, ApJS, 142, 35
Khostovan, A. A., Sobral, D., Mobasher, B., et al. 2016, MNRAS, 463, 2363
Kim, K., Malhotra, S., Rhoads, J. E., Butler, N. R., & Yang, H. 2020, ApJ,
   893, 134
Kimm, T., Blaizot, J., Garel, T., et al. 2019, MNRAS, 486, 2215
Kobulnicky, H. A., Kennicutt, R. C. J., & Pizagno, J. L. 1999, ApJ, 514, 544
Kobulnicky, H. A., & Skillman, E. D. 1998, ApJ, 497, 601
Koekemoer, A. M., Faber, S. M., Ferguson, H. C., et al. 2011, ApJS, 197, 36
Kornei, K. A., Shapley, A. E., Erb, D. K., et al. 2010, ApJ, 711, 693
Kreckel, K., Groves, B., Schinnerer, E., et al. 2013, ApJ, 771, 62
Kriek, M., Shapley, A. E., Reddy, N. A., et al. 2015, ApJS, 218, 15
Kunth, D., Mas-Hesse, J. M., Terlevich, E., et al. 1998, A&A, 334, 11
Leclercq, F., Bacon, R., Verhamme, A., et al. 2020, A&A, 635, A82
Lee, K.-S., Alberts, S., Atlee, D., et al. 2012, ApJL, 758, L31
Leitherer, C., Leão, J. R. S., Heckman, T. M., et al. 2001, ApJ, 550, 724
Leung, G. C. K., Coil, A. L., Aird, J., et al. 2019, ApJ, 886, 11
Levesque, E. M., & Richardson, M. L. A. 2014, ApJ, 780, 100
Ma, X., Hopkins, P. F., Kasen, D., et al. 2016, MNRAS, 459, 3614
Ma, X., Quataert, E., Wetzel, A., et al. 2020, MNRAS, 498, 2001
Mainali, R., Stark, D. P., Tang, M., et al. 2020, MNRAS, 494, 719
Marchi, F., Pentericci, L., Guaita, L., et al. 2019, A&A, 631, A19
Maseda, M. V., Bacon, R., Lam, D., et al. 2020, MNRAS, 493, 5120
Maseda, M. V., Brinchmann, J., Franx, M., et al. 2017, A&A, 608, A4
Matthee, J., & Schaye, J. 2018, MNRAS Lett., 479, L34
Matthee, J., Sobral, D., Best, P., et al. 2017, MNRAS, 465, 3637
Matthee, J., Sobral, D., Hayes, M., et al. 2021, MNRAS, 505, 1382
Mauerhofer, V., Verhamme, A., Blaizot, J., et al. 2021, A&A, 646, A80
McGaugh, S. S. 1991, ApJ, 380, 140
McLean, I. S., Steidel, C. C., Epps, H. W., et al. 2012, Proc. SPIE, 8446,
McLure, R. J., Pentericci, L., Cimatti, A., et al. 2018, MNRAS, 479, 25
Meier, D. L., & Terlevich, R. 1981, ApJL, 246, L109
Momose, R., Ouchi, M., Nakajima, K., et al. 2014, MNRAS, 442, 110
Mostardi, R. E., Shapley, A. E., Steidel, C. C., et al. 2015, ApJ, 810, 107
Nagao, T., Maiolino, R., & Marconi, A. 2006, A&A, 459, 85
Naidu, R. P., Tacchella, S., Mason, C. A., et al. 2020, ApJ, 892, 109
Nakajima, K., Fletcher, T., Ellis, R. S., Robertson, B. E., & Iwata, I. 2018a,
       RAS, 477, 2098
Nakajima, K., & Ouchi, M. 2014, MNRAS, 442, 900
Nakajima, K., Ouchi, M., Shimasaku, K., et al. 2013, ApJ, 769, 3
Nakajima, K., Schaerer, D., Le Fèvre, O., et al. 2018b, A&A, 612, A94
Nanayakkara, T., Brinchmann, J., Boogaard, L., et al. 2019, A&A, 624, A89
Nanayakkara, T., Brinchmann, J., Glazebrook, K., et al. 2020, ApJ, 889, 180
Nestor, D. B., Shapley, A. E., Kornei, K. A., Steidel, C. C., & Siana, B. 2013,
   ApJ, 765, 47
Nestor, D. B., Shapley, A. E., Steidel, C. C., & Siana, B. 2011, ApJ, 736, 18
Noeske, K. G., Weiner, B. J., Faber, S. M., et al. 2007, ApJL, 660, L43
Nomoto, K., Tominaga, N., Umeda, H., Kobayashi, C., & Maeda, K. 2006,
   NuPhA, 777, 424
Oesch, P. A., Labbé, I., Bouwens, R. J., et al. 2013, ApJ, 772, 136
Oke, J. B., Cohen, J. G., Carr, M., et al. 1995, PASP, 107, 375
Oke, J. B., & Gunn, J. E. 1983, ApJ, 266, 713
Osterbrock, D. E., & Ferland, G. J. 2006, Astrophysics of Gaseous Nebulae
   and Active Galactic Nuclei (Sausalito, CA: University Science Books)
Ouchi, M., Ono, Y., & Shibuya, T. 2020, ARA&A, 58, 617
Pahl, A. J., Shapley, A., Faisst, A. L., et al. 2020, MNRAS, 493, 3194
Pahl, A. J., Shapley, A., Steidel, C. C., Chen, Y., & Reddy, N. A. 2021,
   MNRAS, 505, 2447
Pannella, M., Carilli, C. L., Daddi, E., et al. 2009, ApJL, 698, L116
Papovich, C., Finkelstein, S. L., Ferguson, H. C., Lotz, J. M., & Giavalisco, M.
   2011, MNRAS, 412, 1123
Partridge, R. B., & Peebles, P. J. E. 1967, ApJ, 147, 868
Pentericci, L., Grazian, A., Fontana, A., et al. 2007, A&A, 471, 433
```

```
Pentericci, L., Grazian, A., Fontana, A., et al. 2009, A&A, 494, 553
Pentericci, L., Grazian, A., Scarlata, C., et al. 2010, A&A, 514, A64
Pentericci, L., McLure, R. J., Garilli, B., et al. 2018, A&A, 616, A174
Pérez-Montero, E., Hägele, G. F., Contini, T., & Díaz, Á I. 2007, MNRAS,
  381, 125
Pettini, M., Kellogg, M., Steidel, C. C., et al. 1998, ApJ, 508, 539
Pilyugin, L. S., Vilchez, J. M., Mattsson, L., & Thuan, T. X. 2012, MNRAS,
   421, 1624
Price, S. H., Kriek, M., Barro, G., et al. 2020, ApJ, 894, 91
Price, S. H., Kriek, M., Brammer, G. B., et al. 2014, ApJ, 788, 86
Price, S. H., Kriek, M., Shapley, A. E., et al. 2016, ApJ, 819, 80
Prochaska, J. X., Kasen, D., & Rubin, K. 2011, ApJ, 734, 24
Ravindranath, S., Monroe, T., Jaskot, A., Ferguson, H. C., & Tumlinson, J.
   2020, ApJ, 896, 170
Reddy, N., Dickinson, M., Elbaz, D., et al. 2012a, ApJ, 744, 154
Reddy, N. A., Erb, D. K., Pettini, M., Steidel, C. C., & Shapley, A. E. 2010,
     J, 712, 1070
Reddy, N. A., Kriek, M., Shapley, A. E., et al. 2015, ApJ, 806, 259
Reddy, N. A., Oesch, P. A., Bouwens, R. J., et al. 2018a, ApJ, 853, 56
Reddy, N. A., Pettini, M., Steidel, C. C., et al. 2012b, ApJ, 754, 25
Reddy, N. A., Shapley, A. E., Kriek, M., et al. 2020, ApJ, 902, 123
Reddy, N. A., Shapley, A. E., Sanders, R. L., et al. 2018b, ApJ, 869, 92
Reddy, N. A., & Steidel, C. C. 2009, ApJ, 692, 778
Reddy, N. A., Steidel, C. C., Fadda, D., et al. 2006, ApJ, 644, 792
Reddy, N. A., Steidel, C. C., Pettini, M., et al. 2008, ApJS, 175, 48
Reddy, N. A., Steidel, C. C., Pettini, M., & Bogosavljević, M. 2016a, ApJ,
Reddy, N. A., Steidel, C. C., Pettini, M., Bogosavljević, M., & Shapley, A. E.
   2016b, ApJ, 828, 108
Ribeiro, B., Le Fèvre, O., Tasca, L. A. M., et al. 2016, A&A, 593, A22
Rivera-Thorsen, T. E., Hayes, M., Östlin, G., et al. 2015, ApJ, 805, 14
Rix, S. A., Pettini, M., Leitherer, C., et al. 2004, ApJ, 615, 98
Robertson, B. E., Furlanetto, S. R., Schneider, E., et al. 2013, ApJ, 768, 71
Rudie, G. C., Steidel, C. C., Shapley, A. E., & Pettini, M. 2013, ApJ, 769, 146
Runco, J. N., Shapley, A. E., Sanders, R. L., et al. 2021, MNRAS, 502, 2600
Salim, S., Boquien, M., & Lee, J. C. 2018, ApJ, 859, 11
Sanders, R. L., Shapley, A. E., Kriek, M., et al. 2016, ApJ, 816, 23
Scarlata, C., Colbert, J., Teplitz, H. I., et al. 2009, ApJL, 704, L98
Scarlata, C., & Panagia, N. 2015, ApJ, 801, 43
Schaerer, D., Fragos, T., & Izotov, Y. I. 2019, A&A, 622, L10
Schaerer, D., Izotov, Y. I., Nakajima, K., et al. 2018, A&A, 616, L14
Schreiber, C., Pannella, M., Elbaz, D., et al. 2015, A&A, 575, A74
Senchyna, P., Stark, D. P., Vidal-García, A., et al. 2017, MNRAS, 472, 2608
Shapley, A. E., Steidel, C. C., Pettini, M., & Adelberger, K. L. 2003, ApJ,
  588, 65
Shapley, A. E., Steidel, C. C., Pettini, M., Adelberger, K. L., & Erb, D. K.
   2006, ApJ, 651, 688
Sharma, M., Theuns, T., Frenk, C., et al. 2016, MNRAS Lett., 458, L94
Shibuya, T., Ouchi, M., Harikane, Y., & Nakajima, K. 2019, ApJ, 871, 164
Shimakawa, R., Kodama, T., Steidel, C. C., et al. 2015, MNRAS, 451, 1284
Shirazi, M., & Brinchmann, J. 2012, MNRAS, 421, 1043
Shirazi, M., Brinchmann, J., & Rahmati, A. 2014, ApJ, 787, 120
Shivaei, I., Reddy, N., Rieke, G., et al. 2020, ApJ, 899, 117
Shivaei, I., Reddy, N. A., Siana, B., et al. 2018, ApJ, 855, 42
Siana, B., Shapley, A. E., Kulas, K. R., et al. 2015, ApJ, 804, 17
Siana, B., Smail, I., Swinbank, A. M., et al. 2009, ApJ, 698, 1273
Siana, B., Teplitz, H. I., Chary, R.-R., Colbert, J., & Frayer, D. T. 2008, ApJ,
   689, 59
Skelton, R. E., Whitaker, K. E., Momcheva, I. G., et al. 2014, ApJS, 214, 24
Smith, A., Ma, X., Bromm, V., et al. 2019, MNRAS, 484, 39
Sobral, D., Best, P. N., Smail, I., et al. 2014, MNRAS, 437, 3516
Sommariva, V., Mannucci, F., Cresci, G., et al. 2012, A&A, 539, A136
Spitzer, L. 1978, Physical Processes in the Interstellar Medium (New York:
Stanway, E. R., & Eldridge, J. J. 2018, MNRAS, 479, 75
Stanway, E. R., Eldridge, J. J., & Becker, G. D. 2016, MNRAS, 456, 485
Stark, D. P., Richard, J., Siana, B., et al. 2014, MNRAS, 445, 3200
Stark, D. P., Walth, G., Charlot, S., et al. 2015, MNRAS, 454, 1393
Steidel, C. C., Bogosavljević, M., Shapley, A. E., et al. 2011, ApJ, 736, 160
Steidel, C. C., Bogosavljević, M., Shapley, A. E., et al. 2018, ApJ, 869, 123
Steidel, C. C., Rudie, G. C., Strom, A. L., et al. 2014, ApJ, 795, 165
Steidel, C. C., Shapley, A. E., Pettini, M., et al. 2004, ApJ, 604, 534
Steidel, C. C., Strom, A. L., Pettini, M., et al. 2016, ApJ, 826, 159
Strom, A. L., Steidel, C. C., Rudie, G. C., et al. 2017, ApJ, 836, 164
Tang, M., Stark, D. P., Chevallard, J., et al. 2021, MNRAS, 501, 3238
Tang, M., Stark, D. P., Chevallard, J., & Charlot, S. 2019, MNRAS, 489, 2572
```

```
Theios, R. L., Steidel, C. C., Strom, A. L., et al. 2019, ApJ, 871, 128
Topping, M. W., Shapley, A. E., Reddy, N. A., et al. 2020a, MNRAS, 495, 4430
Topping, M. W., Shapley, A. E., Reddy, N. A., et al. 2020b, MNRAS, 499, 1652
Trainor, R. F., Steidel, C. C., Strom, A. L., & Rudie, G. C. 2015, ApJ, 809, 89
Trainor, R. F., Strom, A. L., Steidel, C. C., et al. 2019, ApJ, 887, 85
Trainor, R. F., Strom, A. L., Steidel, C. C., & Rudie, G. C. 2016, ApJ, 832, 171
van der Wel, A., Chang, Y.-Y., Bell, E. F., et al. 2014, ApJL, 792, L6
Vanzella, E., De Barros, S., Cupani, G., et al. 2016, ApJL, 821, L27
Vanzella, E., Giavalisco, M., Inoue, A. K., et al. 2010, ApJ, 725, 1011
Vanzella, E., Guo, Y., Giavalisco, M., et al. 2012, ApJ, 751, 70
```

```
Vasei, K., Siana, B., Shapley, A. E., et al. 2016, ApJ, 831, 38
Verhamme, A., Dubois, Y., Blaizot, J., et al. 2012, A&A, 546, A111
Verhamme, A., Orlitová, I., Schaerer, D., et al. 2017, A&A, 597, A13
Verhamme, A., Schaerer, D., Atek, H., & Tapken, C. 2008, A&A, 491, 89
Verhamme, A., Schaerer, D., & Maselli, A. 2006, A&A, 460, 397
Villar-Martín, M., Cerviño, M., & González Delgado, R. M. 2004, MNRAS, 355, 1132
Whitaker, K. E., Franx, M., Leja, J., et al. 2014, ApJ, 795, 104
Wisotzki, L., Bacon, R., Brinchmann, J., et al. 2018, Natur, 562, 229
Wofford, A., Leitherer, C., & Salzer, J. 2013, ApJ, 765, 118
Xue, R., Lee, K.-S., Dey, A., et al. 2017, ApJ, 837, 172
Zackrisson, E., Inoue, A. K., & Jensen, H. 2013, ApJ, 777, 39
```